Photon Reconstruction for the H. E. S. S. 28 m Telescope and Analysis of Crab Nebula and Galactic Centre Observations

Dissertation
zur Erlangung des akademischen Grades
"doctor rerum naturalium"
(Dr. rer. nat.)
in der Wissenschaftsdisziplin "Astroteilchenphysik"

eingereicht an der
Mathematisch-Naturwissenschaftlichen Fakultät
der Universität Potsdam

von
Markus Holler

Potsdam, den 24. Juni 2014

Published online at the
Institutional Repository of the University of Potsdam:
URL http://opus.kobv.de/ubp/volltexte/2014/7209/
URN urn:nbn:de:kobv:517-opus-72099
http://nbn-resolving.de/urn:nbn:de:kobv:517-opus-72099

Kurzfassung

In der vorliegenden Dissertation wird die zur Zeit sensitivste Methode zur Photonrekonstruktion in der bodengebundenen Gammastrahlungsastronomie an das 28 m H.E.S.S. Teleskop angepasst. Die Analyse basiert auf einem semi-analytischen Modell von elektromagnetischen Teilchenschauern in der Erdatmosphäre. Die Rekonstruktion erfolgt durch den Vergleich des Bildes der Teleskopkamera mit der Tscherenkow-Emission, die mittels des Schauermodells berechnet wurde. Zur Verringerung des dominanten Untergrundes, der hauptsächlich durch Teilchen der geladenen kosmischen Strahlung hervorgerufen wird, werden Ereignisse anhand bestimmter Kriterien ausgewählt. Die Leistungsfähigkeit der Analyse wird unter Verwendung simulierter Ereignisse evaluiert. Die Methode wird anschließend auf zwei Gammastrahlungsquellen angewendet. Zuerst wird der Krebsnebel analysiert, die Standardkerze der bodengebundenen Gammastrahlungsastronomie. Die Resultate der Analyse des Krebsnebels bestätigen die bereits zuvor erwartete Leistungsfähigkeit der Rekonstruktionsmethode, wobei hier insbesondere die im Vergleich zu H.E.S.S. I stark verringerte Energieschwelle hervorzuheben ist. Als Zweites werden Beobachtungen der Region um das galaktische Zentrum ausgewertet. Die Analyseergebnisse dieser Daten unterstreichen die Fähigkeiten des neuen Teleskops zur Messung kosmischer Gammastrahlung in einem für die theoretische und experimentelle Astrophysik interessanten Energiebereich. Die vorgestellte Analyse besitzt die niedrigste Energieschwelle, die in der bodengebundenen Gammastrahlungsastronomie je erreicht wurde. Sie ermöglicht damit präzise Messungen der physikalischen Eigenschaften von zeitabhängigen Quellen im Energiebereich von 10 bis 100 GeV.

Abstract

In the presented thesis, the most advanced photon reconstruction technique of ground-based γ-ray astronomy is adapted to the H. E. S. S. 28 m telescope. The method is based on a semi-analytical model of electromagnetic particle showers in the atmosphere. The properties of cosmic γ-rays are reconstructed by comparing the camera image of the telescope with the Cherenkov emission that is expected from the shower model. To suppress the dominant background from charged cosmic rays, events are selected based on several criteria. The performance of the analysis is evaluated with simulated events. The method is then applied to two sources that are known to emit γ-rays. The first of these is the Crab Nebula, the standard candle of ground-based γ-ray astronomy. The results of this source confirm the expected performance of the reconstruction method, where the much lower energy threshold compared to H. E. S. S. I is of particular importance. A second analysis is performed on the region around the Galactic Centre. The analysis results emphasise the capabilities of the new telescope to measure γ-rays in an energy range that is interesting for both theoretical and experimental astrophysics. The presented analysis features the lowest energy threshold that has ever been reached in ground-based γ-ray astronomy, opening a new window to the precise measurement of the physical properties of time-variable sources at energies of several tens of GeV.

Contents

1 Introduction

As in most fields of science, the evolution of observational astronomy from its very beginning has essentially been powered by three fundamental aspects:

- curiosity
- ingenuity
- technical progress

These three parts together form the fundamentals of scientific progress, where most of the time, one of them pushes another. This is illustrated in the following with some selected examples.

Up to the early 17th century, humans could observe the sky with only their naked eyes. While their curiosity must have been limitless when witnessing events like supernovae, which proved that the celestial sphere is not as static as believed by most people, lack of technology prevented an enlargement of their view of the world. This changed when the first refracting telescopes were invented in the Netherlands, enabling those with immense curiosity and ingenuity like Galileo Galilei to end that era of stagnation. Holding one of these instruments towards the night sky for the first time opened up a new window of science. All of the phenomena that were discovered at that time due to the magnification and light collection of the first telescopes raised the people's curiosity, paving the way for successful subsequent centuries of observational astronomy.

In the 20th century, the field of astrophysics outgrew its original boundaries. Whereas before it was limited to the observation and interpretation of objects at optical wavelengths, the technical progress gave birth to new fields of astronomy at other parts of the electromagnetic spectrum. An example of this is the *Chandra* telescope (see *left panel* of Fig. 1.1), which is a masterpiece of high-precision manufacturing. After its deployment in 1999, it changed the view of astrophysical objects that emit X-rays due to its unprecedented angular resolution.

Furthermore, it was found out that not only electromagnetic radiation provides information about outer space. Made curious because of previous indications, the Austrian physicist Victor Franz Hess discovered charged cosmic rays in 1912. Despite the high danger, he undertook several balloon flights up to altitudes of more than 5 km and showed that the number of ionising particles increases with height, which corresponds to the first real experiment of astroparticle physics.

At very high energies (VHE, $E \gtrsim 100\,\mathrm{GeV}$), the photon fluxes of most cosmic sources are too low to be detected with spaceborne instruments because of their low effective collection area. As first discovered by Galbraith & Jelley (1953), optical sensors can be used to image the Cherenkov light of particle showers as initiated by cosmic particles; this approach leads to much larger detection areas and is thus suited to exploration of the VHE γ-ray sky. It has been successfully being used for more than two decades to detect and measure cosmic sources. Whereas only a couple of sources were known ten years ago, their

Fig. 1.1: *Left:* artist's impression of the *Chandra* X-ray telescope. Image credit: NASA/CXC. *Right:* Victor Hess before departing for a balloon flight. Image from Breisky (2012).

count has rapidly increased to almost 150 since then (for an updated number, please visit `http://tevcat.uchicago.edu`). The reasons for this rapid increase are those mentioned at the beginning. Part of it is accounted for by better instrumentation. Additionally, this success was enabled by improving the existing reconstruction and analysis techniques and inventing new ones.

In 2012, the largest Cherenkov telescope that has ever been built was inaugurated, corresponding to a large step concerning instrumentation in order to explore and understand the VHE γ-ray sky. In this thesis, the most advanced reconstruction technique of ground-based γ-ray astronomy is adapted to this new telescope, which seeks to provide the technical progress needed to detect new sources and source classes to provide further insight into our Universe.

The subsequent chapter contains an overview of atmospheric particle showers, followed by the general principles of the Imaging Atmospheric Cherenkov Technique. At the end of the chapter, the H. E. S. S. II telescope, which is the detector used for all subsequent studies, is introduced. In Chapter 3, different ways to reconstruct the energy and direction of a cosmic γ-ray with a single IACT are described. The focus is set on a reconstruction method that is based on a semi-analytical shower model. The performance of this reconstruction method is evaluated in Chapter 4. The method is subsequently applied to two complementary sources in Chapter 5, namely the Crab Nebula and the Galactic Centre region. Conclusions are drawn in Chapter 6, followed by an outlook.

2 Ground-Based γ-ray Astronomy

This chapter contains an overview of the field of ground-based γ-ray astronomy. It starts with a short introduction about particle showers that are created when cosmic rays and γ-rays interact with the Earth's atmosphere. Section 2.2 is about Imaging Atmospheric Cherenkov Telescopes in general, whereas the H. E. S. S. 28 m telescope, which is the instrument used for all the subsequent studies and analyses, is introduced in Section 2.3.

2.1 Atmospheric Particle Showers

Cosmic γ-rays that hit the atmosphere interact with its matter, initiating showers consisting of secondary particles. The main processes that are relevant for the evolution of an electromagnetic particle shower are (as outlined in de Naurois (2012)):

- the production of an e^+e^- pair by a γ-ray in the Coulomb field of an atmospheric nucleus.
- emission of Bremsstrahlung when an electron or positron is decelerated or deflected by the Coulomb field of a nucleus.
- deflection of electrons and positrons by the electric fields of the nuclei (Coulomb scattering).
- ionisation and excitation of atmospheric nuclei by the electrons and positrons of the shower. These mechanisms dominate over the emission of Bremsstrahlung at particle energies below the so-called critical energy, which is $E_{\mathrm{crit}} \approx 83\,\mathrm{MeV}$ in air. Particles with $E < E_{\mathrm{crit}}$ are rapidly decelerated.

The first two processes are the ones responsible for the amplification of the electromagnetic cascade. The respective average interaction length for Bremsstrahlung and pair production is, to first order, identical. It is called the radiation length ($X_0 \approx 36.7\,\mathrm{g\,cm^{-2}}$) and is given in units of an area density. Assuming normal weather conditions and an altitude of 1800 m above sea level, the atmosphere has a thickness of 22 radiation lengths. Since only one interaction channel with few processes is involved, electromagnetic cascades tend to evolve quite regularly. This is apparent from the *top panel* of Fig. 2.1, which shows the profiles of ten simulated electromagnetic showers, each initiated by a γ-ray with an energy of 300 GeV.

In addition to γ-rays, the atmosphere is continuously exposed to a bombardment of cosmic rays, most of them being hadrons. Particle showers that are initiated by hadrons consist of several components (again referring to de Naurois (2012)):

- hadronic components, mostly consisting of fragments of nuclei and pions.
- electromagnetic sub-showers, initiated by, e.g., γ-rays that originate from the decay of a neutral pion.
- muons, created by the decay of charged mesons.

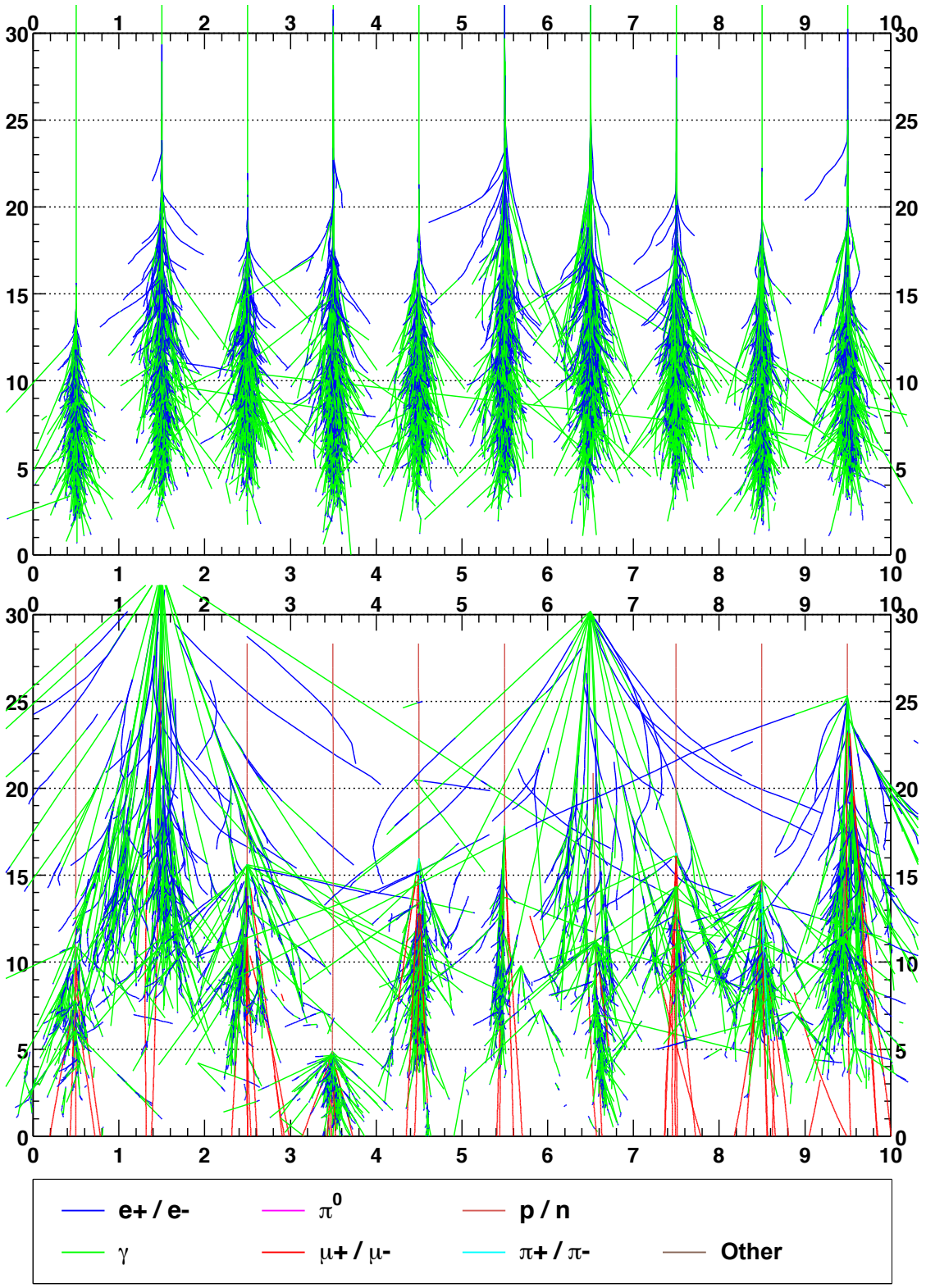

Fig. 2.1: Profiles of ten simulated electromagnetic (*top*) and hadronic (*bottom*) particle showers, all initiated by particles with an energy of 300 GeV. The vertical axes denote the height above sea level in units of km. The lateral displacement of the particles, as projected on each horizontal axis, is also given in units of km. The color legend is shown on the very bottom. Only particles with $E > E_{\mathrm{crit}}$ are displayed. Figure taken from de Naurois (2000).

- neutrinos, produced in several decay channels.

As more interaction channels are involved in the development of hadronic showers, they tend to evolve quite irregularly compared to electromagnetic showers. This is obvious from the *bottom panel* of Fig. 2.1, displaying the profiles of showers created by protons with an energy of 300 GeV.

Using Monte Carlo (MC) simulations that take into account the relevant interaction processes, an atmospheric model, and the strength and orientation of the Earth magnetic field, it is possible to create virtual showers. The software code used in this work is the KASCADE program that was developed by Kertzman & Sembroski (1994). Specifying the particle type, its energy, and direction of movement, the development of secondary particles that form the shower is calculated. To reach the desired statistics, this process is performed many times.

2.2 Imaging Atmospheric Cherenkov Telescopes

All the positrons and electrons of a particle shower with $E > E_{\mathrm{crit}}$ move at highly relativistic velocities, faster than the speed of light of the medium (i.e. air) they are traversing. Cherenkov (1934) discovered that light is emitted under these conditions, which is named Cherenkov light after its discoverer. Most of the radiation is typically emitted in the ultraviolet regime, but part of it is visible to the human eye, enabling the particle shower to be imaged with optical sensors. The Cherenkov light is radiated in the shape of a cone in the direction of movement of its parent particle. The opening angle of the cone is given by

$$\alpha = \arccos\left(\frac{1}{\beta n}\right) , \tag{2.1}$$

where n corresponds to the refractive index of the medium and β to the velocity of the charged particle relative to the speed of light in vacuum. For $\beta \approx 1$ and an index of refraction $n_{\mathrm{air}} \approx 1.00023$ at an altitude of 1800 m above sea level (see Eq. (2.8) in de Naurois (2000)), the opening angle is $\alpha \approx 1.2°$. At higher altitudes, the opening angle is smaller due to a lower index. This influence is taken into account by the MC software package described in Kertzman & Sembroski (1994), which calculates the Cherenkov emission of each particle of the simulated shower and propagates it to the ground.

The overall emission of the shower corresponds to a superposition of the emission of the individual particles, as is sketched in Fig. 2.2. The light pool of the superimposed Cherenkov cones covers an area of the order of $10^5\,\mathrm{m}^2$ (depending on the first interaction depth of the γ-ray, its energy, and fluctuations). Placing a telescope on the ground which is capable of imaging the Cherenkov light changes the atmosphere overhead into a huge calorimeter; due to this measuring technique, such a telescope is called an Imaging Atmospheric Cherenkov Telescope (IACT). IACTs can generally detect showers whose light pools cover their position, enabling very large effective areas as compared to spaceborne telescopes which measure γ-rays directly.

Fig. 2.1 and 2.2 display the shower profiles and the Cherenkov emission integrated over the entire evolution of the shower. In reality, the shower front and its associated Cherenkov emission progress at similarly large velocities and feature a thickness of only a few metres. Measured at a given position on the ground, the Cherenkov light front typically lasts for ≈ 10 ns. Using photosensors with a comparably short integration time helps the signal to be separated from the photons of the night-sky background (NSB).

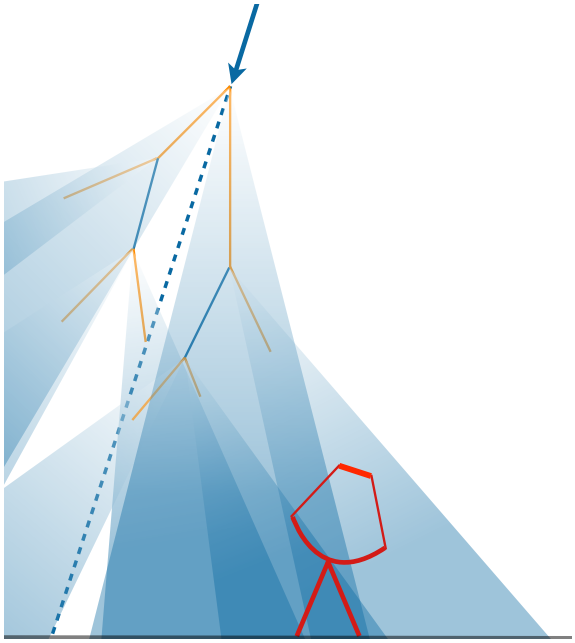

Fig. 2.2: Sketch illustrating the superposition of Cherenkov emission of the electrons and positrons (both displayed in orange) of an electromagnetic shower as initiated by a γ-ray. The proportions are strongly distorted for better visibility.

2.3 The H. E. S. S. 28 m Telescope

The H. E. S. S. (High Energy Stereoscopic System) array consists of five IACTs (see *top panel* of Fig. 2.3), situated in the Khomas highland in Namibia at an altitude of $\approx 1800\,\mathrm{m}$ above sea level. Their geographic location near the Tropic of Capricorn allows for observations of the whole southern sky, including the central part of the Galaxy, as well as parts of the northern sky. The H. E. S. S. telescopes can observe 80% of the whole celestial sphere at zenith angles below 60°, and 45% of it at zenith angles below 30°.

Originally, the array only consisted of the four identical smaller telescopes that are shown in Fig. 2.3 (*top panel*). They started operating in 2004 and have since become the most successful ground-based γ-ray astronomy experiment. For the remainder of this thesis, the original array will be called "H. E. S. S. I", and the telescopes shall be referred to as "H. E. S. S. I telescopes".

A fifth IACT was built in the centre of the existing array (see Fig. 2.3). This telescope, which will be called "the H. E. S. S. II telescope" from now on, was inaugurated in September 2012. As for the H. E. S. S. I telescopes, an alt-azimuth mount (made of steel) was used for the new telescope. The total mass of the structure is around 560 tons. The mount is equipped with a powerful drive system which is able to move the telescope with speeds of up to 200° per minute in azimuth and half as fast in altitude (Hofverberg et al. 2013). The mount hosts a dish with a size of $24\,\mathrm{m} \times 33\,\mathrm{m}$, holding the mirror of the telescope. The mirror itself actually consists of 875 identical facets, covering an area of $600\,\mathrm{m}^2$ that reflects the Cherenkov light of air showers and focuses it on a focal plane that is 36 m distant. The collection area corresponds to an effective diameter of 28 m (i.e. the diameter of a circular mirror with the same area), making the H. E. S. S. II telescope by far the largest IACT that has ever been built. The parabolic shape of the mirror ensures

Fig. 2.3: *Top:* the complete H. E. S. S. array with all telescopes pointing southwards. *Bottom left:* mirror facets of the H. E. S. S. II telescope during deployment. *Bottom right:* camera of the H. E. S. S. II telescope. Images courtesy of C. Medina (*top* and *bottom left*) and A. Balzer (*bottom right*).

the correct arrival times of the Cherenkov photons during the reflection.

The Cherenkov light is collected at the focal plane, using a camera with a diameter of around 2 m, corresponding to a Field of View (FoV) of $\approx 3.2^\circ$ (see *bottom right* panel of Fig. 2.3). The camera consists of 2048 photomultipliers (PMTs; also called pixel in the following) which are similar to the ones used for the cameras of the H. E. S. S. I telescopes. To maximise the light collection area, a Winston cone is placed in front of each PMT. Following a trigger signal, the camera reads out the charge of each pixel of the camera, integrated over a time window of 16 ns (see Barnacka (2013) for a detailed description of the trigger of the H. E. S. S. II telescope). To achieve a wide dynamical range, two amplification channels are used for the signal of each PMT, called the high-gain and low-gain, respectively. Calibrating the camera as described in Aharonian et al. (2004b), the charge in both channels is used to calculate the approximate number of photons entering the PMT. Differences of PMT collection efficiencies (due to different quantum efficiencies and Winston cone cleanliness) are also taken into account by the calibration. To estimate the absolute loss of Cherenkov light from entering the telescope until entering the windows of the PMTs, isolated muons of particle showers are used. This method is extensively described in Chalme-Calvet et al. (2014). Instead of the absolute optical efficiency mentioned in that reference, values in this thesis always refer to the relative optical efficiency. A relative optical efficiency of 100% corresponds to a telescope with 100% mirror reflectivity, clean Winston cones, and new PMTs whose quantum efficiency has not yet degraded.

In addition to the integrated charge, the camera of the H. E. S. S. II telescope reads out two time stamps that characterise the signal shape as measured by each PMT. The first value is the so-called *Time over Threshold*, which corresponds to the duration of the signal above a certain threshold value. The second is the *Time of Maximum*, denoting the time of the peak amplitude within the integration window. Both values are determined with an accuracy of ≈ 1 ns. Exploiting this additional information could, e.g., help to suppress the NSB (see Aliu et al. (2009) for a detailed review about how to make use of signal timing). For a more technical description of the camera of the H. E. S. S. II telescope, the reader is referred to Bolmont et al. (2013).

To utilise the virtual showers that are created by KASCADE, a collaboration-internal software is used. It simulates the telescope by taking into account the mirror size, its shape, the overall optical efficiency, and the quantum efficiency of the PMTs. In addition to that, the software simulates NSB in the virtual camera, finally providing a realistic camera image of the simulated shower which can be compared with measured events.

As low NSB values are crucial for the precise measurement of Cherenkov emission of particle showers, H. E. S. S. only operates during moonless nights. Observations are split into runs of 28 minutes duration where typically all telescopes track the position of the object of interest. The data taken during a run are processed by a data acquisition system which is described in Balzer et al. (2014).

3 Photon Reconstruction

This chapter describes how to reconstruct the parameters of a cosmic γ-ray using the camera image of a single IACT, such as the H. E. S. S. II telescope. The focus is set on a reconstruction method that uses a semi-analytical shower model, but the necessary preceding steps are also introduced.

3.1 Overview

As described in Section 2.2, IACTs detect γ-rays indirectly by measuring the Cherenkov light emitted by the induced cascade of electromagnetic particles. Once simulations have been carried out for γ-rays with varying initial parameters the measured Cherenkov camera image can be interpreted and the γ-ray parameters inferred. In order to do so, there are several independent approaches.

The Hillas method After the cleaning of the camera image, it is possible to reduce the amount of information stored for each image (i.e. position and amplitude) to a few parameters which characterise the shower image. These parameters can be used to estimate the properties of the incoming photon (Hillas 1985).

The template method An alternative approach is to create templates of the Cherenkov light distribution in the camera for different parameters of the incoming γ-ray. Events can then be reconstructed by comparing the measured camera image with the templates, searching for the parameter set that fits best.

In the following, all the necessary steps are described to trace back the properties of a cosmic VHE γ-ray with a single IACT. The starting point is a calibrated camera image of a simulated event, containing the intensity of each camera pixel in units of photoelectrons (pe). The simulated observation conditions of this example event are:

- Azimuth angle: 180°
- Zenith angle (θ): 18°
- Pointing offset from source position: 0.5°
- Relative optical efficiency: 80%
- NSB rate per pixel: 100 MHz

This configuration was selected in order to give a reasonable estimate of the analysis performance and is therefore also used for the studies in Chapter 4. The camera display of the example event to be reconstructed hereafter is shown in Fig 3.1 (left panel). The properties of the primary γ-ray are as follows:

- Energy (E): 125 GeV

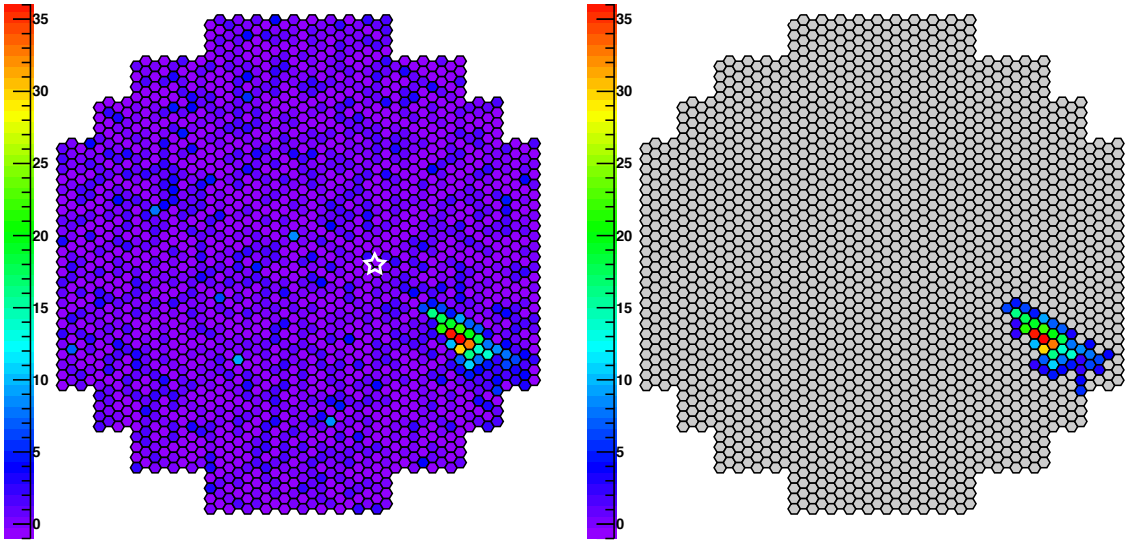

Fig. 3.1: *Left:* display of the camera of the H. E. S. S. II telescope, showing the intensity for a simulated γ-ray (see text for more information) in units of photoelectrons. The true source position is indicated with a white star. *Right:* display of the same event after a *Biggest_2_5* image cleaning (see text for further details). All pixels that were discarded from the image are marked grey.

- Impact distance[1] (R): 130 m
- First interaction depth in the atmosphere (T): 0 (radiation lengths)

Its energy corresponds to the energy threshold of H. E. S. S. I. Strikingly, the shower can be well resolved with the camera of the H. E. S. S. II telescope, already indicating the large capabilities of this instrument at low energies.

In Section 3.2, it is shown how to effectively clean the image in order to remove the pixels that do not belong to the shower. The information contained in the remaining pixels can be used to perform a Hillas analysis, which will be described in the same section. For a better estimation of the properties of the primary particle, one can apply the template method which was mentioned above. The semi-analytical model which is used to create the templates in this work is introduced in Section 3.3.1. In order to find the best parameter estimate, a pixel-wise log-likelihood minimisation is applied (see Section 3.3.2), comparing the measured intensities with those expected from the model templates.

3.2 Reconstruction with Shower Image Parameters

In addition to the Cherenkov light of the particle showers, the pixels of the camera also collect light from NSB. For a reconstruction based on the shape of the shower image parameters, it is thus important to remove these noise pixels from the image. The standard image cleaning procedure used within the H. E. S. S. software consists of two intensity thresholds (Aharonian et al. 2006a). A pixel is only kept if its intensity is above the high-level threshold and at least one of its neighbours exceeds the low-level threshold or vice

[1] The impact distance corresponds to the shortest distance of the projected direction of the γ-ray to the telescope (see Fig. 3.5 for an illustration).

versa. A further optional step consists of removing all pixel clusters (groups of connected pixels passing the first cleaning step) except for that cluster containing the pixel with the highest intensity (so-called cluster cleaning). The nomenclature used henceforth is as follows:

- *Clean/Biggest_(low-level cut in* pe*)_(high-level cut in* pe*)*

The cleaned image is denoted with *Biggest* in case the above-mentioned cluster selection was applied, and with *Clean* in case it was not. Figure 3.1 (right panel) contains the pixels of the example event that pass a *Biggest_2_5* cleaning (all removed pixels are marked grey). As can be seen, the applied method with the selected cut configuration effectively removed the background pixels while keeping most of the shower pixels in this particular case. Generally, changing the threshold values has a strong influence on the subsequent event reconstruction, especially at low energies and for large impact distances. Lowering the intensity cuts directly results in more accepted low-energy events and thus a reduced energy threshold, which is one of the main goals of the analysis presented in this work. However, the cleaned images tend to be noisier for lower thresholds, which has a negative influence on the overall reconstruction performance.

After cleaning the camera image, it is possible to reduce the information of the remaining pixels (i.e. position and intensity) to a few parameters which characterise the shower image (Hillas 1985). The coordinate system, which is used for the calculations in the camera plane, is the so-called *Nominal System* and is extensively described in Gillesen (2004). Its point of origin roughly corresponds to the camera centre[2]. The coordinates are given in units of distance in the camera plane (which is viewed from the telescope dish), divided by the focal length of the telescope (f) and therefore almost equalling angles in units of radian. This definition makes this system also applicable for stereoscopic reconstruction with different telescope types. Suppose that the cleaned image contains n pixels whose coordinates are (x_i, y_i). The first value characterising the cleaned image is the sum of the intensities of the remaining pixels, called *Size*. The amount of Cherenkov light in the cleaned image is strongly correlated with the primary energy E and the impact distance R. With the pixel intensity, a_i, *Size* can simply be calculated as

$$Size = \sum_{i=1}^{n} a_i \ . \tag{3.1}$$

The next step is to compute the *Centre of Gravity* (CoG), which is defined as the barycentre of the pixel positions, each weighted with the amplitude a_i:

$$CoG = \begin{pmatrix} < x > \\ < y > \end{pmatrix} \ , \text{ where } \ < x >= \frac{\sum_{i=1}^{n} a_i \cdot x_i}{\sum_{j=1}^{n} a_j} \ \text{ and } \ < y >= \frac{\sum_{i=1}^{n} a_i \cdot y_i}{\sum_{j=1}^{n} a_j}. \tag{3.2}$$

In addition to the CoG, one can further make use of the second moments of the distribution,

$$\sigma_{x^2} = \frac{\sum_{i=1}^{n} a_i x_i^2}{\sum_{j=1}^{n} a_j} - < x >^2, \ \sigma_{y^2} = \frac{\sum_{i=1}^{n} a_i y_i^2}{\sum_{j=1}^{n} a_j} - < y >^2, \ \sigma_{xy} = \frac{\sum_{i=1}^{n} a_i x_i y_i}{\sum_{j=1}^{n} a_j} - < x >< y > \ . \tag{3.3}$$

Reducing the pixel information of the cleaned image to these first and second moments simplifies the shower to an ellipse (the Hillas ellipse), with its centre being the CoG. For

[2] In case of only one telescope and no mis-pointing, the camera centre and the point of origin of the *Nominal System* exactly match.

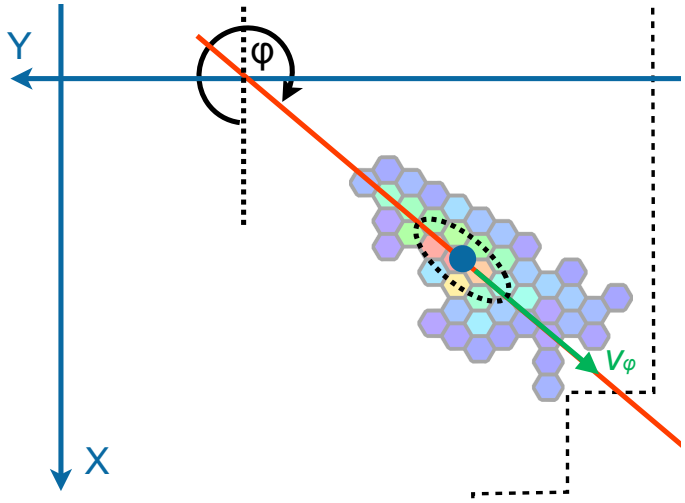

Fig. 3.2: Sketch illustrating the parameterisation of the cleaned shower image, using the same event as in Fig. 3.1. The camera centre is roughly located at the point of origin of the coordinate system. The *CoG* is indicated with the blue dot within the shower image, with the black-dashed Hillas ellipse around it. The length axis is shown as a solid red line. The direction vector $\vec{v}_\varphi$ is drawn in green. φ is measured clockwise because of the orientation of the x and y axes.

the above example event, this is illustrated in Fig. 3.2. In order to derive the semi-major and semi-minor axis of the ellipse (henceforth called length and width, respectively) as well as its orientation, the second moments can be written in a matrix:

$$\begin{pmatrix} \sigma_{x^2} & \sigma_{xy} \\ \sigma_{xy} & \sigma_{y^2} \end{pmatrix}. \tag{3.4}$$

This matrix can be considered as a linear transformation. Due to the definitions above, σ_{x^2} and σ_{y^2} are greater than or equal to zero. If indeed both are greater than zero, which is almost always the case for cleaned shower images that still contain a signal, the matrix can be diagonalised due to its symmetry. The eigenvalues can then be shown to be

$$\lambda_{1/2} = \frac{\sigma_{x^2} + \sigma_{y^2} \pm \sqrt{(\sigma_{x^2} - \sigma_{y^2})^2 + 4\sigma_{xy}^2}}{2}. \tag{3.5}$$

Defining

$$\chi = \sigma_{x^2} - \sigma_{y^2} \tag{3.6}$$

and

$$z = \sqrt{\chi^2 + 4\sigma_{xy}^2}, \tag{3.7}$$

gives

$$\lambda_{1/2} = \frac{\sigma_{x^2} + \sigma_{y^2} \pm z}{2}. \tag{3.8}$$

With $z \geq 0$, $\lambda_1 \geq \lambda_2$, and the length and width can thus be derived to

$$L = \sqrt{\frac{\sigma_{x^2} + \sigma_{y^2} + z}{2}}, \quad W = \sqrt{\frac{\sigma_{x^2} + \sigma_{y^2} - z}{2}}. \tag{3.9}$$

Again referring to the diagonalisation of (3.4), the eigenvectors of the transformation reflect the orientation of the ellipse. They can be shown to be

$$\vec{v}_1 = \begin{pmatrix} \chi + z \\ 2\sigma_{xy} \end{pmatrix} \ , \ \vec{v}_2 = \begin{pmatrix} \chi - z \\ 2\sigma_{xy} \end{pmatrix}, \tag{3.10}$$

where $\vec{v}_1$ is the eigenvector defining the direction of the length axis. Due to the geometry of an electromagnetic shower and its emitted Cherenkov light, the direction of the primary γ-ray is expected to lie somewhere on this axis.

There are two possibilities to reconstruct the direction of a γ-ray, one along the positive and one along the negative orientation of $\vec{v}_1$. Since the actual orientation of $\vec{v}_1$ with respect to the camera centre is hard to comprehend from its definition, it is convenient to define a new vector:

$$\vec{v}_\varphi = (\vec{v}_1 \circ CoG)\, \vec{v}_1 = ... = (\chi + z) \begin{pmatrix} (\chi + z) < x > +2\sigma_{xy} < y > \\ 2\sigma_{xy} < x > +(z - \chi) < y > \end{pmatrix}. \tag{3.11}$$

By definition, $\vec{v}_\varphi$ points out of the camera (see Fig. 3.2). Using Eq. 3.11, the angle enclosed by the x axis of the camera system and $\vec{v}_\varphi$ can easily be derived to:

$$\varphi = \arctan \left(\frac{2\sigma_{xy} < x > +(z - \chi) < y >}{(\chi + z) < x > +2\sigma_{xy} < y >} \right). \tag{3.12}$$

As mentioned above, the source direction of the incoming particle is expected to lie along the length axis of the Hillas ellipse in case of a γ-ray. If the shower triggers more than one telescope of the array, the direction can thus be determined by intersecting the length axes of the Hillas ellipses from the individual camera images. In the case that only one telescope triggers, the direction determination is more complicated since neither the direction from the CoG nor the distance from the CoG to the source direction (called δ from now on) is known.

In order to resolve the direction ambiguity, one can use the asymmetry of the shower image along the length axis. Generally, the intensity distribution of a shower tends to be peaked towards the source direction, as can already be seen by eye for the example event used here. For quantifying the asymmetry of a given shower image, it is useful to first project every pixel on the length axis and calculate its offset from the CoG, as visualised in Fig. 3.3. Defining

$$\vec{v}_{\mathrm{d,i}} = \begin{pmatrix} x_i - < x > \\ y_i - < y > \end{pmatrix} \ , \tag{3.13}$$

this offset turns out to be

$$x_{\varphi,\mathrm{i}} = \cos\varphi \cdot (x_i - < x >) + \sin\varphi \cdot (y_i - < y >) \ . \tag{3.14}$$

By definition, the positive direction of x_φ is the same as the direction of $\vec{v}_\varphi$. Now the asymmetry of the intensity distribution along the length axis can be quantified using its second and third central moments. The asymmetry coefficient (which is also called skewness) can be computed as follows:

$$\gamma = \frac{\mu_3}{\mu_2^{3/2}} = \frac{\frac{1}{Size} \cdot \sum_{i=1}^{n} a_i \cdot x_{\varphi,\mathrm{i}}^3}{\left(\frac{1}{Size} \cdot \sum_{j=1}^{n} a_j \cdot x_{\varphi,\mathrm{j}}^2 \right)^{3/2}} \ . \tag{3.15}$$

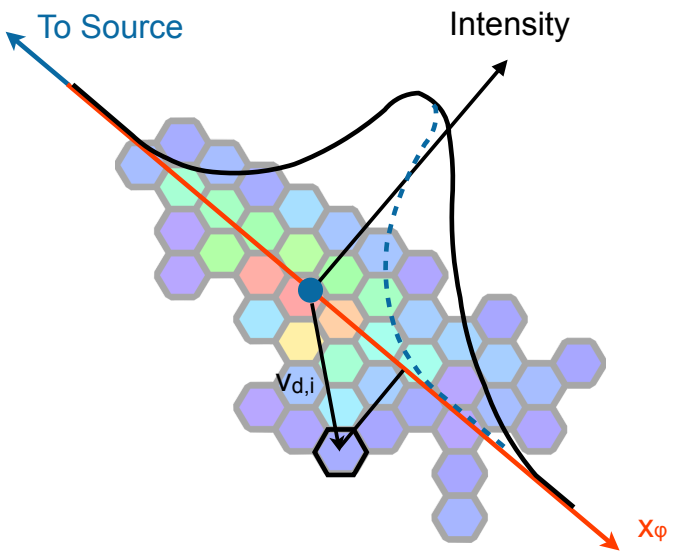

Fig. 3.3: Illustration of the skewness calculation for the example event. The intensity distribution along the length axis is sketched with a black line. If the distribution would continue like the dashed blue line after the maximum, the skewness would be 0.

Table 3.1: Parameters that characterise a cleaned camera image and their values for the event used in this chapter.

Parameter	n	*Size* [pe]	*CoG* (*Nominal System*)	L	W [°]	φ	γ
Value	45	489	$(0.0084, -0.0178)$	0.0026	0.0011	309	0.22

For a distribution that is peaked towards lower values of x_φ (as in Fig. 3.3), Eq. 3.15 gives a positive result and likewise a negative result for those peaked towards higher values. It is thus possible to guess the source direction from the *CoG* by just evaluating the sign of γ. However, it has to be mentioned that due to statistical fluctuations of the shower development and other possible irregularities that may appear in the cleaned image, the sign of the skewness does not always lead to the correct solution. This particularly concerns events that belong to γ-rays with low energies where the cleaned image only consists of a few pixels.

The values of all the parameters introduced above are given in Table 3.1 for the example event. With these parameters, it is possible to reconstruct the properties of the primary particle under the assumption that it is a γ-ray. This is done by first filling lookup tables which relate the measurable parameters with the true primary properties for simulated events. For creating the tables, it is necessary to simulate a large number of MC γ-rays with different properties (i.e. E, R, and T). For each of these events, one can calculate *Size*, L, W, and δ. As the true source direction is needed for the calculation of δ, it is actually one of the parameters to be estimated. The reconstruction of the primary properties then corresponds to the following mapping:

$$(Size,\, L,\, W) \rightarrow (E,\, R,\, \delta,\, (T)) \ . \tag{3.16}$$

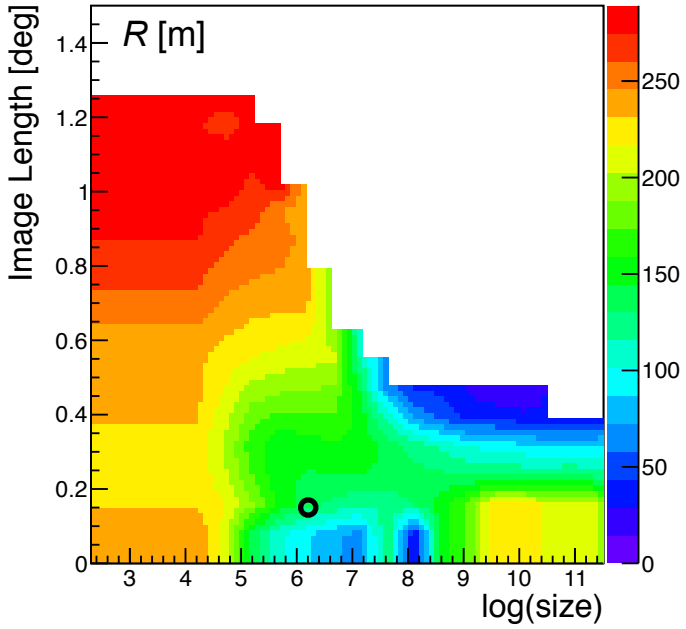

Fig. 3.4: Lookup table containing the mean impact distance R for different values of $\ln(Size)$ and L. To each of the events that were used for the table, a *Clean_2_5* image cleaning was applied. The black circle indicates the reconstructed values of the example event.

Compared to E and R, a variation of T has the lowest influence on the amount and distribution of Cherenkov light in the camera. As it does also not contain any intrinsic information about the γ-ray before reaching the atmosphere, it can be left out in the reconstruction mapping in order to decrease the degeneracy. However, the T values of the simulated events that are used for the calibration of the mapping should be distributed as expected for real events in order to avoid systematic effects. Since T is given in units of radiation lengths, the distribution is simply

$$\frac{\mathrm{d}N_\gamma}{\mathrm{d}T} \propto 2^{-T} \,. \tag{3.17}$$

Looping over all simulated events, lookup tables for E, R, and δ are created, each taking $\ln(Size)$ and L as input parameters. Tables are generated for certain zenith angles θ, relative optical efficiencies and image cleanings. Since the value range of $Size$ extends over several orders of magnitude, its natural logarithm is used for the histograms. The 2D lookup table for the impact distance is shown in Fig. 3.4. The impact distance of the example event can be estimated by taking the value at the location of the black circle. Together with the tables for E and δ, it is then possible to estimate the properties of the primary particle, assuming that it was a γ-ray.

As the last step of this reconstruction method, the approximate γ-ray source direction is determined, and optionally also the coordinate of the impact point. The source direction is reconstructed as

$$Dir = \vec{CoG} + \vec{v}_\delta \text{ , with } \vec{v}_\delta = -\delta \cdot \begin{pmatrix} \cos\varphi \\ \sin\varphi \end{pmatrix} \,. \tag{3.18}$$

All of the above calculations were carried out in the *Nominal System*. For the reconstruction of the impact point, it is however necessary to switch to another coordinate system.

The one used here is the three-dimensional Cartesian *Tilted System* (Gillesen 2004). Its

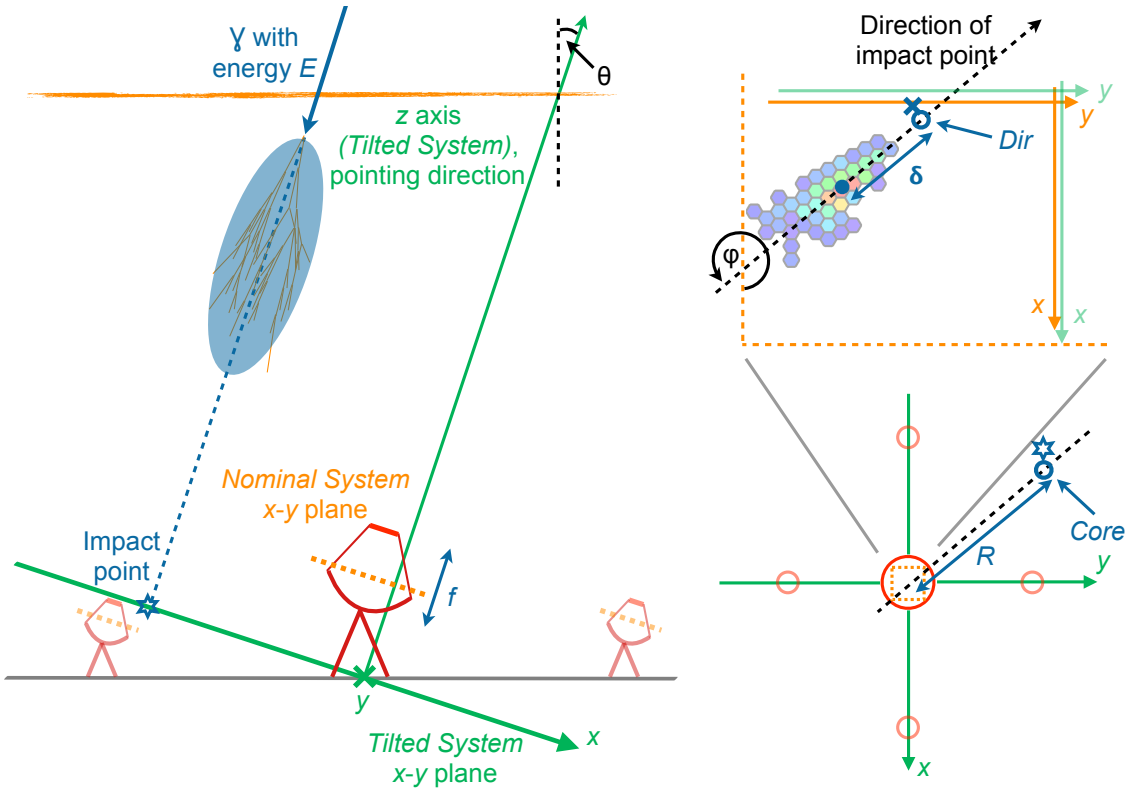

Fig. 3.5: Illustration of the reconstruction of direction and impact point of the example event. Orange and green colours denote the *Nominal System* and *Tilted System* in all sub-figures, respectively. *Left:* schematic side view of H. E. S. S., looking in positive y direction of the *Tilted System*. *Right, upper panel:* reconstruction of the source direction (*Dir*) in the *Nominal System*, but viewed towards negative z direction of the *Tilted System* (i.e. from above). Therefore the system is mirrored at the x axis compared to the previous figures. The true source direction is indicated with a blue cross. *Right, lower panel:* illustration of the *Core* reconstruction. It is the same viewing direction as in the upper panel, but further zoomed out (the *Nominal System* is indicated as an orange-dashed inlay). The true impact point is sketched with a blue star. The indicated coordinates and vectors are not to be taken exactly.

point of origin is the centre of the telescope array, and the $x - y$ plane has the same orientation as the *Nominal System* (see also Fig 3.5). Given the geometry of the direction of the primary particle and the shower, the coordinates of the impact point in the *Tilted System* are given by

$$Core = \vec{v}_{\text{tel}} + \vec{v}_R \text{ , where } \vec{v}_R = -R \cdot \begin{pmatrix} \cos\varphi \\ \sin\varphi \\ 0 \end{pmatrix} . \tag{3.19}$$

This equation is basically valid for arbitrary telescope positions. As the H. E. S. S. II telescope is located exactly in the centre of the array, $Core = \vec{v}_R$ in this work. In case the sign of the asymmetry parameter (Eq. 3.15) is negative, Eq. 3.18 and Eq. 3.19 can optionally be modified by multiplying both $\vec{v}_\delta$ and $\vec{v}_R$ with $\text{sign}(\gamma)$. Considering the

Table 3.2: Actual and Hillas-reconstructed properties of the example event.

Parameter	E [GeV]	δ	R [m]	Dir (*Nominal System*)	$Core$ (*Tilted System*, [m])
True Value	125	0.0123	130	$(0.0002, -0.0087)$	$(-88, 95, -1)$
Reconstructed Value	161	0.0122	122	$(0.0007, -0.0084)$	$(-77, 94, 0)$

geometry of the origin of the γ-ray, the shower location, and the impact point (see left panel of Fig. 3.5), Dir and $Core$ are expected to be reconstructed in opposite directions. However, this is not the case when comparing Eq. 3.18 and Eq. 3.19 since $\vec{v}_\delta$ and $\vec{v}_R$ point in the same direction. This is due to the fact that the telescope mirror leads to an inverting of all coordinates and vectors that are expressed in the *Nominal System*.

Finally, Table 3.2 contains the true and the reconstructed properties of the simulated γ-ray that was accurately analysed here. As can be seen, the agreement between the reconstructed and actual parameters is quite good. In order to further exploit the information that is contained in the camera image and improve the reconstructed values, a modelling approach is used in this work which is described in the next section.

3.3 Reconstruction Using a Semi-Analytical Model

The previous section described how to reconstruct the properties of a VHE γ-ray with a single IACT, reducing the information of the pixels of the cleaned camera image to a small set of parameters. This approach is widely used in ground-based γ-ray astronomy, but it has a major disadvantage: condensing the entire information of the camera image (i.e. the single pixel intensities) to the Hillas parameters, a lot of information is thrown away that is potentially interesting for the event reconstruction and classification.

In 2003, de Naurois et al. introduced an alternative method for the reconstruction of γ-rays which is based on a pixel-wise comparison of the camera image and the expected Cherenkov photon density of a γ-ray with certain properties (the method was described in much greater detail in de Naurois & Rolland (2009), which is therefore the reference that is cited in the remainder of this thesis). In this approach, the information of each pixel is exploited. The method was applied to H. E. S. S. I data and performed very well in terms of angular resolution, energy bias and resolution. Together with multivariate analysis techniques (Ohm et al. 2009), it provides the best sensitivity currently reached in this field. By now, the method has been used for lots of H. E. S. S. publications and became one of the standard analyses in the collaboration. In order to continue this success story of groundbreaking science results, the method is now also going to be used for H. E. S. S. II. For analysing the new data, it is necessary to adapt the software.

Hereafter, it is delineated how to reconstruct a γ-ray with the modelling approach of de Naurois & Rolland (2009) using the information of the H. E. S. S. II telescope only. After depicting the model generation in Section 3.3.1, the chapter ends with a description of the fitting procedure that is used to estimate the properties of the primary particle (Section 3.3.2).

3.3.1 The Shower Model

There are different ways to obtain the average Cherenkov photon density on the ground for γ-rays with given E, R, and T. One possibility is to simulate γ-rays with different parameters and use the photon distribution as a template for the event reconstruction[3]. In order to smooth the statistical fluctuations of the shower development, it is necessary to simulate a lot of events for each parameter set and then average over the resulting distributions. This template generation method is explained in more detail in Mazin (2007) and Parsons & Hinton (2014). The approach chosen by de Naurois & Rolland (2009) and also used in this work is different in the way that the particle distributions of the simulated electromagnetic showers are described by a semi-analytical model. Using this model, it is possible to calculate the theoretical Cherenkov photon density on the ground and in the camera of the telescope. As the model generation part was not substantially changed for this work, it will be only shortly outlined below, closely following de Naurois & Rolland (2009). For a more detailed description, the reader is referred to their work.

Following Greisen (1956), the longitudinal distribution of charged particles in a shower that was initiated by a γ-ray is estimated to (de Naurois & Rolland 2009)

$$\mathcal{N}_e(Y,t) = \frac{a}{\sqrt{Y}} \times \exp\left[t \times \left(1 - \frac{b}{b-1} \times \ln(s)\right)\right] + \left(2 - \frac{a}{\sqrt{Y}}\right) \times \exp(-t) \ .$$

Here t denotes the shower depth in units of radiation lengths. The energy of the γ-ray is redefined to

$$Y = \ln\left(\frac{E}{E_{\mathrm{crit}}}\right) \ , \tag{3.20}$$

with the critical energy $E_{\mathrm{crit}} \approx 83\,\mathrm{MeV}$ (see also Section 2.1). s is defined such as to have a value of 0 at $t = 0$ and of 1 at the shower maximum and is therefore called the shower age. In de Naurois & Rolland (2009), it is given by

$$s = \frac{b}{1 + c \times (b-1)/t} \ . \tag{3.21}$$

Optimising a, b, and c, Eq. 3.20 is fit to the particle distributions that are obtained from MC simulations. The results of the optimisation are (de Naurois & Rolland 2009)

$$a = 1.05 + 0.033 \times Y, \quad b = 2.66, \quad c = 0.97 \times Y - 1.32 \ . \tag{3.22}$$

The modelled longitudinal shower development for different γ-ray energies is shown in Fig. 3.6, together with the averaged distributions that are obtained from the MC sample.

In addition to the longitudinal shower development, the model also takes into account the lateral and angular distribution of the particles of the shower (see de Naurois & Rolland (2009) for further details). Using this description of an average electromagnetic shower created by a γ-ray with a certain primary energy E, first interaction depth T and impact distance R, it is possible to calculate the distribution of Cherenkov light in the camera

[3] Note that this approach is the same as for the lookup table generation (see Section 3.2), with the difference that the whole photon distribution is kept and not only the Hillas parameters.

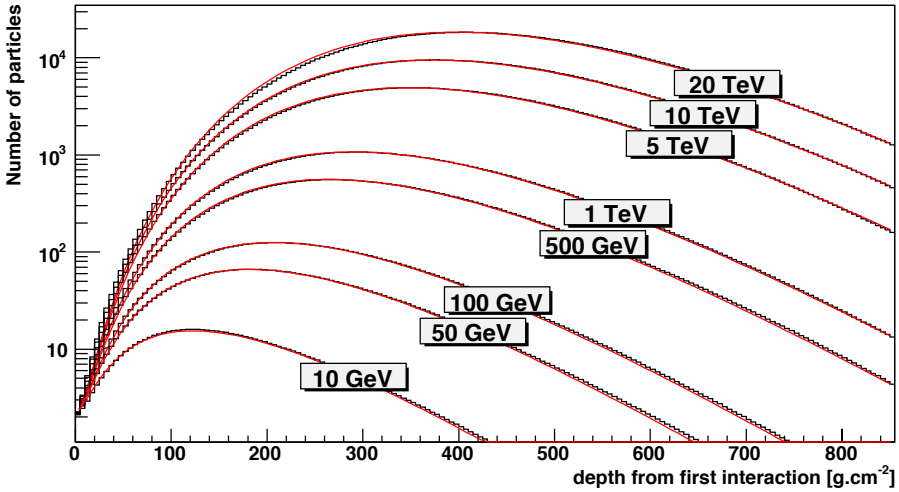

Fig. 3.6: Longitudinal development of the number of charged particles in a shower for different primary γ-ray energies. For each energy, the black line corresponds to the average value as obtained from MC simulations, whereas the modelled distribution is denoted with a red line, respectively. Figure taken from de Naurois & Rolland (2009).

with the following integral (de Naurois & Rolland 2009):

$$\begin{aligned} I(x_T, y_T) \quad = \quad & \int \mathrm{d}z \int \mathrm{d}E' \times \frac{\mathrm{d}\mathcal{N}_e}{\mathrm{d}E'}(t, E') \times \frac{\mathrm{d}t}{\mathrm{d}z}(Y) \\ & \int \mathrm{d}u \times F_u(u(E', s)) \int \frac{\mathrm{d}\phi}{2\pi} \\ & \int \mathrm{d}X_r \int \mathrm{d}Y_r F_{XY}(X_r, Y_r, E', s, u) \\ & \int \mathrm{d}\phi_{ph} \int \frac{\mathrm{d}\lambda}{\lambda^2} \frac{\mathrm{d}^2 n_\gamma}{\cos\theta \, \mathrm{d}z \, \mathrm{d}\lambda} \times \exp(-\tau(z, \lambda)) \times Q_{eff}(\lambda) \\ & \times Col(z, X_r, Y_r, u, \phi, \phi_{ph}) \ . \end{aligned} \tag{3.23}$$

This formula is subdivided into integrals over the (see the reference for more details about the individual variables)

- altitude z or atmospheric depth T, respectively,
- shower particle energy E',
- rescaled direction angle u of the particles with respect to the shower axis, relative to the average one,
- second direction angle (ϕ) of the particle with respect to the telescope, measured in the plane that is perpendicular to the shower axis,
- rescaled lateral coordinates X_r and Y_r of the particles,
- azimuthal Cherenkov photon angle ϕ_{ph} around the shower particle direction,
- Cherenkov photon wavelength λ.

The functions contained in Eq. 3.23 are (if not obvious or already mentioned above):

- $F_u(u(E', s))$: angular distribution of the shower particles, normalised to 1.

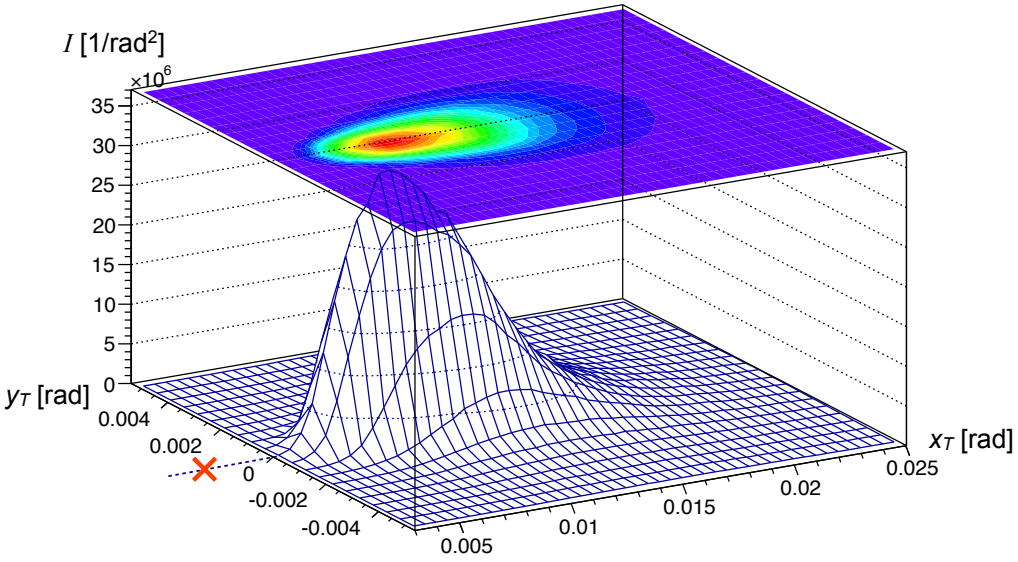

Fig. 3.7: Model template for the H. E. S. S. II telescope, containing the expected density of Cherenkov photons for a γ-ray with zenith angle 18°, primary energy 126 GeV, first interaction depth 0, and impact distance 129 m. The source direction is at the point of origin which is marked with a red cross.

- $F_{XY}(X_r, Y_r, E', s, u)$: lateral distribution of the shower particles, also normalised to 1.
- $(1/\lambda^2) \times (\mathrm{d}^2 n_\gamma / \cos\theta \, \mathrm{d}z \, \mathrm{d}\lambda)$: Cherenkov photon production rate of a shower particle moving with angle θ with respect to the shower axis.
- $\exp(-\tau(z, \lambda))$: atmospheric absorption of Cherenkov photons.
- $Q_{eff}(\lambda)$: quantum efficiency of the detector.
- $Col(z, X_r, Y_r, u, \phi, \phi_{ph})$: average geometrical efficiency to detect Cherenkov photons that are emitted by a shower particle under the angle ϕ_{ph}, with the particle being at location (z, X_r, Y_r) and moving in direction (u, ϕ).

The calculation also takes into account other detector properties, such as the trigger time and the integration time of the readout window. $I(x_T, y_T)$ is symmetrical along the x_T axis and given in units of pe/rad^2. The point of origin of the coordinate system corresponds to the source direction of the γ-ray. For computational reasons, the integration is performed in several discrete steps (see de Naurois & Rolland (2009) for further details). The result is a two-dimensional histogram with a certain bin width which should be smaller than the pixel size. An example for such a model template is shown in Fig. 3.7 for parameters which are very close to the true values of the example event used in this chapter. As can be seen, the distribution is asymmetrically peaked towards the source direction, as already mentioned in Section 3.2. When analysing an event, the bin size of both x_T and y_T is sampled to 40% of the old size.

Model templates are created for certain zenith angles which are set as follows. Let d be the distance from the upper layer of the atmosphere to the ground when pointing to the zenith (see Fig. 3.8). If observing at a zenith angle θ, the distance becomes $d' = d/\cos\theta$. Model template sets are created for zenith angles that correspond to linear steps in d',

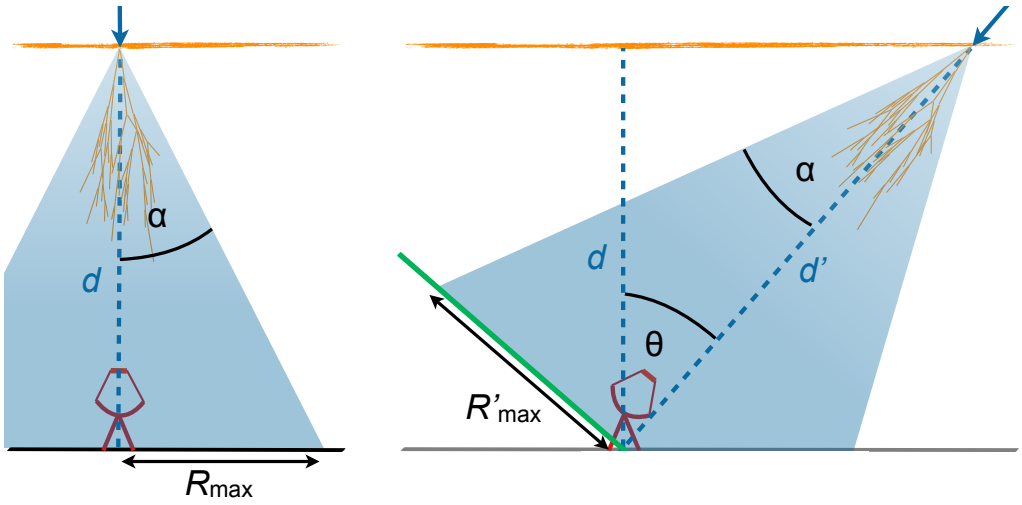

Fig. 3.8: Sketch illustrating the distances d and d' as well as the radii of the Cherenkov light pools. The latter is simplified to a cone with opening angle α.

Table 3.3: Some of the zenith angles used for creating model template sets, following Eq. 3.24.

i	0	1	2	3	...	15	16
$\theta_i[^\circ]$	0	18	25	30	...	55	56

starting with $d' = d$. The spacing was selected such that

$$\theta_i = \arccos\left(\frac{1}{1 + i/20}\right) \quad , \quad i = 0, 1, 2, \ldots \quad . \tag{3.24}$$

Some values of θ_i are given in Table 3.3. Whereas there are not many template sets needed at low zenith angles, the spacing of the angles between two consecutive sets is very small for large i. The analysis of an event is performed with the template set whose θ_i is closest to the current zenith angle. For each θ_i, 31200 templates are created, with

- 40 impact distances, linearly spaced between 0 m and $(400/\cos\theta_i)$ m,
- 65 different energies, ranging from $(5/\cos\theta_i)$ GeV to $(80/\cos\theta_i)$ TeV (logarithmically spaced),
- 12 first interaction depths, linearly spaced between 0 and 5.

Compared to de Naurois & Rolland (2009), the energy range was extended by one order of magnitude to lower energies in order to account for the lower energy threshold of H. E. S. S. II. Simplifying the Cherenkov light pool to a cone with a fixed opening angle, the ratio of the radii of the cones for zenith angle 0° and θ is (see also Fig. 3.8):

$$\frac{R'_{\mathrm{max}}}{R_{\mathrm{max}}} = \frac{d'}{d} = \frac{1}{\cos\theta} \, . \tag{3.25}$$

Therefore, the range of R is scaled by a factor of $1/\cos\theta_i$ for the model template generation. Since the larger light cone also implies a lower photon density (in addition to the greater absorption because of $d' > d$), the energy range is scaled by the same factor. Instead of the energy, Y (see Eq. 3.20) is used for the model generation and reconstruction. As

this variable is defined using the logarithm of the energy, the model templates are linearly spaced in Y.

In the shower model described above, the lateral distribution of charged particles is radially symmetric around the shower axis. This assumption neglects the deflection of these particles due to the earth magnetic field. In fact, the magnetic field leads to a distortion and rotation of the shower images in the camera (Commichau et al. 2008). Neglecting this effect in the reconstruction mechanism implies, e.g., a widening of the point spread function. To prevent this, the semi-analytical shower model could be generated for several azimuth values. Additionally, breaking the symmetry of the lateral distribution of the shower means that it is not possible to use the same model template for all values of φ (e.g. the shape of the Cherenkov image in the camera also depends on the azimuth angle of the impact point).

3.3.2 The Optimisation Method

The previous subsection outlined how to create model templates that contain the average Cherenkov photon density in the camera for a γ-ray with given Y, R, and T. With these templates, the intensity of each pixel in the camera is compared to the prediction from the model for certain parameters. For a single pixel, the probability to measure a signal intensity s (in units of pe) is calculated as (de Naurois & Rolland 2009)

$$P(s|\mu,\sigma_p,\sigma_\gamma,\sigma_c) = \sum_n \frac{\mu^n e^{-\mu}}{n!\sqrt{2\pi(\sigma_p^2+n\sigma_\gamma^2+n^2\sigma_c^2)}} \exp\left(-\frac{(s-n)^2}{2(\sigma_p^2+n\sigma_\gamma^2+n^2\sigma_c^2)}\right) , \quad (3.26)$$

where μ is the expectation value from the model. The equation is basically a discrete convolution of two probability functions:

- $P_\mu(n)$: Poissonian with expectation value μ. The realisation value n corresponds to the number of actual Cherenkov photons arriving at the pixel, but already multiplied with the average quantum efficiency (see Eq. 3.23).
- $\mathcal{N}\left(n, (\sigma_p^2+n\sigma_\gamma^2+n^2\sigma_c^2)\right)$: normal distribution with mean n, reflecting the (quantum-efficiency-corrected) response of the PMT.

σ_p is the pedestal width which is mostly correlated to the NSB rate. σ_γ corresponds to the width of the single photoelectron peak (i.e. the resolution of the PMT), and σ_c takes into account possible calibration uncertainties. Eq. 3.26 is visualized in Fig. 3.9. For small values of μ, the distribution is clearly asymmetrical, exhibiting the pedestal and the single pe peak. For larger μ, the function is approximated by a Gaussian. In order to quantify the agreement of measured and modelled intensities for a set of pixels (from which the broken ones are disregarded), the log-likelihood function is considered (similar to de Naurois & Rolland 2009):

$$\ln L_{\text{set}} = \sum_{\text{pixel } i} \ln L_i = \sum_{\text{pixel } i} -2 \times \ln P(s_i|\mu_i,\sigma_p,\sigma_\gamma,\sigma_c) \ . \quad (3.27)$$

The goal of the model reconstruction is to optimise the γ-ray parameters by minimising the log-likelihood of the whole camera[4]. Before describing the optimisation procedure in

[4] In case of more than one telescope, even the log-likelihood of all participating telescopes has to be minimised.

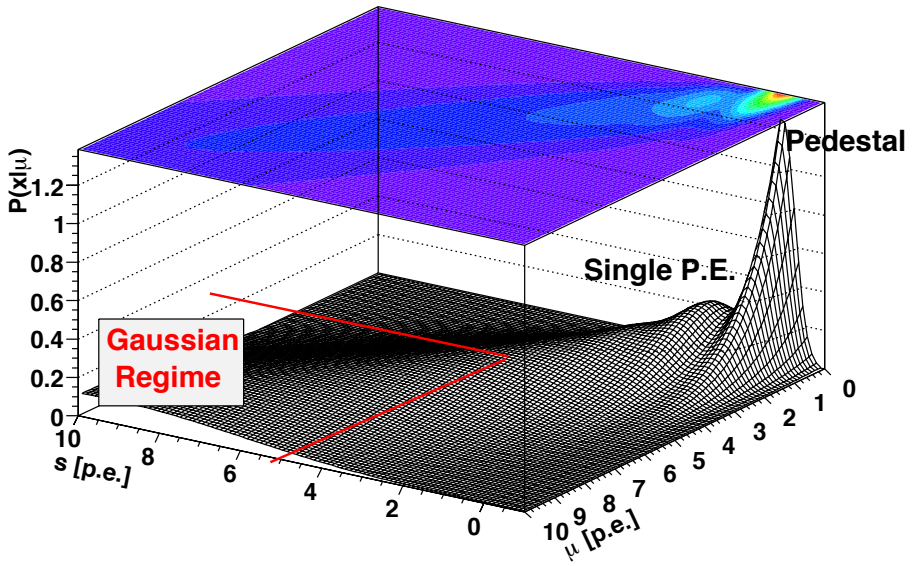

Fig. 3.9: Visualisation of the pixel-wise probability (see Eq. 3.26)) for $\sigma_c = 0$. Figure taken from de Naurois & Rolland (2009).

greater detail, it is necessary to explain how to calculate the model expectation value μ of a pixel at position (x', y') in the *Nominal System* for a given set of parameters.

First of all, one has to recall that the coordinate of the impact point with corresponding impact distance R is defined in the *Tilted System* with the point of origin in the centre of the array. In contrast, the impact distance for a particular model template, denoted ρ from now on, is given with respect to the telescope position. However, as the H. E. S. S. II telescope is located at the centre of the array, no major conversion has to be applied for the single-telescope reconstruction[5]. In this case, the direction angle φ can be calculated as (see also Eq. 3.19)

$$\varphi = \arctan\left(-v_{R,y}, -v_{R,x}\right) \ . \tag{3.28}$$

With an assumed source direction $Dir = (x_S, y_S)$ (*Nominal System*) and the direction angle φ, the coordinates of a pixel in the system of the model templates (see e.g. Fig. 3.7) are given by

$$\begin{pmatrix} x'_T \\ y'_T \end{pmatrix} = \begin{pmatrix} \cos\varphi & \sin\varphi \\ -\sin\varphi & \cos\varphi \end{pmatrix} \begin{pmatrix} x' - x_S \\ y' - y_S \end{pmatrix} \ . \tag{3.29}$$

This mapping corresponds to a translation to the assumed source direction, followed by a subsequent rotation around φ.

Since the model templates are created for discrete values of T, Y, and ρ, they are interpolated in order to estimate the Cherenkov photon density for arbitrary values. In this work, a linear interpolation is used which is described in the following[6]. First, the templates that are adjacent to the assumed values (T', Y', ρ') are selected (see Fig. 3.10). Each template is normalised to 1. The natural logarithm of the integral, $\ln\left(S(T_i, Y_j, \rho_k)\right)$, is saved for the subsequent calculations. Naming the integral of a template S accounts for the fact

[5] A small correction has to be made in order to take into account the offset of the source direction from the pointing position. The overall conversion is explained in Balzer (2014).

[6] This is exactly the same method that was already used by de Naurois & Rolland (2009). It was neither developed nor changed by the author of this thesis, but since this rather important part was only shortly mentioned in the reference, it is described here in more detail.

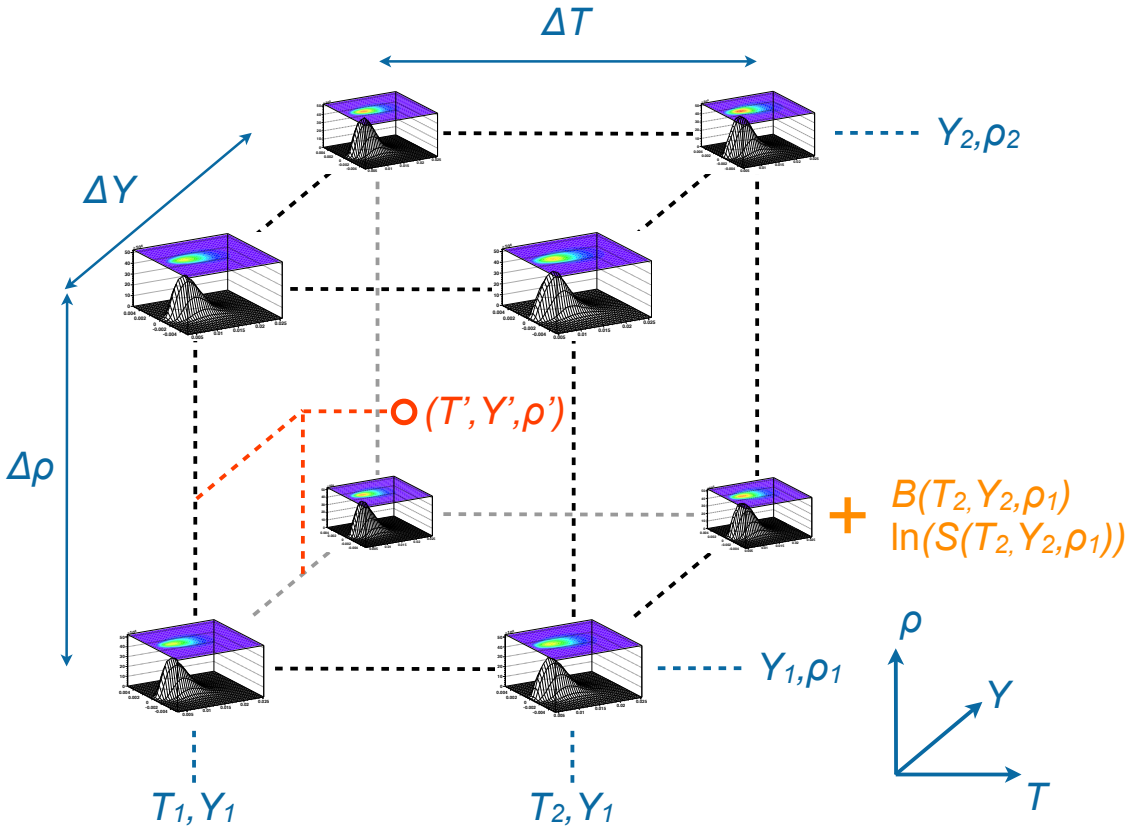

Fig. 3.10: Illustration of the model template grid that is used for the linear interpolation. The assumed values are indicated with a red circle. For each of the adjacent normalised templates, the barycentre B and logarithm of the integral $\ln S$ are saved.

that it is very closely related to the *Size* parameter (see Section 3.2). The intensity of a normalised template is denoted $I_N(x_T, y_T, T_i, Y_j, \rho_k)$. In addition to $\ln S$, a modified barycentre is calculated for each template:

$$B(T_i, Y_j, \rho_k) = \frac{\sum_l x_{T,l} \sum_m I_N\left(x_{T,l}, y_{T,m}, T_i, Y_j, \rho_k\right)^3}{\sum_{p,q} I_N\left(x_{T,p}, y_{T,q}, T_i, Y_j, \rho_k\right)^3} \,, \tag{3.30}$$

where e.g. $x_{T,l}$ corresponds to the x_T value of the centre of bin l. As the model templates are symmetrical along the x_T axis, the barycentre along the y_T direction is always 0. For the definition of B, the third power of the intensity is used in order to stay closer to the maximum and avoid major contributions from the shower tails. The values of B at the grid points (see also Fig. 3.10) can be linearly interpolated to estimate the barycentre at (T', Y', ρ'):

$$B\left(T', Y', \rho'\right) = \sum_{i,j,k=1,2} w_{ijk} \cdot B(T_i, Y_j, \rho_k) \,, \tag{3.31}$$

where

$$w_{ijk} = w_{T,i} \cdot w_{Y,j} \cdot w_{\rho,k}, \text{ with } \; w_{T,1} = \frac{T_2 - T'}{T_2 - T_1}, \quad w_{T,2} = \frac{T' - T_1}{T_2 - T_1} \; \text{ etc.} \tag{3.32}$$

Analogously, the $\ln S$ values at the grid points are interpolated to get $\ln S(T', Y', \rho')$. Furthermore the gradient of B and $\ln S$ is computed. For example, the derivative of B

with respect to T is given by

$$\begin{aligned}\frac{\partial B}{\partial T}(T', Y', \rho') &= [\ w_{Y,2} \cdot w_{\rho,2} \cdot (B(T_2, Y_2, \rho_2) - B(T_1, Y_2, \rho_2)) \\ &+ w_{Y,1} \cdot w_{\rho,2} \cdot (B(T_2, Y_1, \rho_2) - B(T_1, Y_1, \rho_2)) \\ &+ w_{Y,2} \cdot w_{\rho,1} \cdot (B(T_2, Y_2, \rho_1) - B(T_1, Y_2, \rho_1)) \\ &+ w_{Y,1} \cdot w_{\rho,1} \cdot (B(T_2, Y_1, \rho_1) - B(T_1, Y_1, \rho_1))\ ] \\ &/ (T_2 - T_1)\ .\end{aligned} \tag{3.33}$$

Similarly, the other derivatives as well as those of $\ln S$ are obtained. If the offset of the interpolated barycentre to the barycentre at a grid point is defined as

$$\delta B_{ijk} = B(T_i, Y_j, \rho_k) - B(T', Y', \rho')\ , \tag{3.34}$$

then the interpolated photon density is

$$I(x'_T, y'_T, T', Y', \rho') = S(T', Y', \rho') \cdot \sum_{i,j,k=1,2} w_{ijk} \cdot I_N(x'_T + \delta B_{ijk}, y'_T, T_i, Y_j, \rho_k)\ . \tag{3.35}$$

Each of the templates I_N is binned. In order to obtain intensity values for arbitrary (x_T, y_T), the two-dimensional templates are interpolated similar as B in Eq. 3.31. Additionally, the derivatives $\partial I_N/\partial x_T$ and $\partial I_N/\partial y_T$ at $(x'_T + \delta B_{ijk}, y'_T)$ are evaluated, as for the barycentre in Eq. 3.33. Replacing I_N in Eq. 3.35 with $\partial I_N/\partial x_T$ respectively $\partial I_N/\partial y_T$ and afterwards transforming back to the *Nominal System*, one can calculate $\partial I/\partial x$, $\partial I/\partial y$, and $\partial I/\partial \varphi$ for (x', y', T', Y', ρ'). Here, (x', y') are the coordinates in the *Nominal System* that correspond to (x'_T, y'_T). Finally, the derivatives $\partial I/\partial T$, $\partial I/\partial Y$, and $\partial I/\partial \rho$ are computed. The derivatives are needed for the fitting procedure which will be discussed later.

As mentioned in Section 3.3.1, the photon density is given in units of pe/rad^2. For a pixel whose centre is located at (x'_T, y'_T) in the template system, the model expectation value is

$$\mu(x'_T, y'_T) = \frac{I(x'_T, y'_T, T', Y', \rho') \cdot \Omega_p \cdot Eff}{F_p \cdot O_p}\ , \tag{3.36}$$

where Ω_p is the pixel area in units of rad^2, Eff the optical efficiency of the telescope, and F_p corresponds to the flatfield coefficient of the pixel. I and μ and their partial derivatives only differ by a pixel-dependent constant factor. With Eq. 3.36, the pixel-wise probability as given in Eq. 3.26, and also the log-likelihood for a set of pixels (see Eq. 3.27), are calculated.

In order to minimise the log-likelihood, a Levenberg-Marquardt (LM) algorithm (see Levenberg (1944) and Marquardt (1963)) is applied. It is known to be especially efficient if the function to be minimised exhibits a nearly quadratic shape (de Naurois & Rolland 2009). The LM algorithm is an iterative method where the parameter adjustment from step k to $k+1$ is done as follows (Marquardt 1963):

$$\vec{p}[k+1] = \vec{p}[k] - \left(\mathbf{H}[k] + \lambda[k] \cdot \mathrm{diag}\left[\mathbf{H}[k]\right]\right)^{-1} \vec{\nabla}\left(\ln L_{\mathrm{set}}\left(\vec{p}[k]\right)\right)\ , \tag{3.37}$$

where $\vec{p} = (x_S, y_S, \varphi, T, Y, \rho)$. The entries of the gradient can be calculated as

$$\left(\vec{\nabla}\left(\ln L_{\mathrm{set}}\left(\vec{p}[k]\right)\right)\right)_i = \frac{\partial \ln L_{\mathrm{set}}}{\partial p_i}\left(\vec{p}[k]\right) = \sum_{m\,\in\,\mathrm{set}} \left(\frac{\partial L_m}{\partial \mu} \cdot \frac{\partial \mu_m}{\partial p_i}\right)_{\vec{p}=\vec{p}[k]}\ , \tag{3.38}$$

using the fact that $\ln L_{\text{set}}$ is just the sum of the log-likelihood values of the individual pixels of the set (see Eq. 3.27). **H** corresponds to the Hessian matrix of $\ln L_{\text{set}}(\vec{p}[k])$. Its entries are

$$H_{ij} = \frac{\partial^2 \ln L_{\text{set}}}{\partial p_i \partial p_j}(\vec{p}[k]) \approx \sum_{m \in \text{set}} \left(\frac{\partial^2 L_m}{\partial \mu^2} \cdot \frac{\partial \mu_m}{\partial p_i} \cdot \frac{\partial \mu_m}{\partial p_j} \right)_{\vec{p}=\vec{p}[k]} . \tag{3.39}$$

The approximation in the right part of Eq. 3.39 is valid in the quadratic regime of $\ln L_{\text{set}}$ and becomes poorer the greater the deviation from this assumption is. Generally, the LM algorithm can be viewed as a combination of the Gauss-Newton and the gradient descent mechanism, where the factor $\lambda[k]$ is dynamically adjusted after each iteration in order to determine the relative weighting between both (Ranganathan 2004). If $\ln L_{\text{set}}$ decreases from k to $k+1$, the quadratic assumption used in Eq. 3.39 appears to be valid. In this case, $\lambda[k+1]$ is scaled down compared to $\lambda[k]$ (typically by a factor of 10) in order to increase the relative contribution of **H** in Eq. 3.37. In contrast, λ is scaled up by the same factor if the log-likelihood increases with the iteration. For the model reconstruction, an event is considered as converged if $\ln L_{\text{set}}$ decreases in two consecutive iterations, but not by more than 0.01 for each iteration. Furthermore, a minimum of five iteration steps is required. With the Hessian evaluated at the optimised parameter values, it is possible to estimate the fit uncertainty for each parameter as

$$\Delta p_i = \sqrt{H_{ii}} . \tag{3.40}$$

The Levenberg-Marquardt algorithm features a high convergence rate, but is also susceptible to convergence on a distinct local minimum instead of the global minimum. It is thus necessary to take start parameters $\vec{p}[0]$ that are as close as possible to the true values. This is especially important for the single-telescope reconstruction due to the greater degeneracy compared to a stereoscopic analysis. Being a fast and completely independent reconstruction method, the results of the Hillas analysis (see Section 3.2) are used as start parameters for the fitting procedure. As described earlier, the results of this analysis depend on the applied image cleaning thresholds. For the model reconstruction presented in this work, Hillas analyses with the following thresholds are applied (see the beginning of Section 3.2 for the definition):

- *Biggest_2_5*
- *Biggest_3_6*
- *Clean_4_7*

For each cleaning, the source direction and impact point are estimated using Eq. 3.18 and Eq. 3.19 respectively. In addition to this solution, three additional ones are created by replacing φ with $\varphi+90°$, $\varphi+180°$, and $\varphi+270°$. This approach increases the probability of finding correct starting values for images with small *Size* values or those where the image is truncated by the camera border[7]. Using these rotated solutions means that up to twelve sets of starting parameters are available for the reconstruction of an event, increasing the convergence probability of the fit. As the Hillas analysis provides no estimate for the first interaction depth T, a default value of 1 is used for each of the sets. In order to recover information about the shower that was lost due to the cleaning process, each of the cleaned

[7] This method was introduced by M. de Naurois and R. Chalmé-Calvet. The original way the author of this thesis implemented it was to use the normal solution and additionally the one with $\varphi + 180°$ for showers with a negative asymmetry parameter.

Table 3.4: True parameter values of the example event, together with the results from the log-likelihood minimisation. The error on each parameter was estimated using Eq. 3.40.

Parameter	T	$E(Y)$ [GeV]	ρ [m]	$Dir\ (x_S, y_S)$ (*Nominal System*)	φ [°]
True Value	0	125	130	$(0.0002, -0.0087)$	312.68
Reconstructed Value	1.10	126	129	$(0.0008, -0.0094)$	312.25
Error Estimate	0.32	5	6	$(0.0004, 0.0004)$	0.88

images is expanded by two neighbouring rows of pixels. The log-likelihood minimisation is then carried out twice for each of these expanded shower images using the corresponding starting parameters. During the first iteration, T is fixed to its starting value of 1. For the second iteration, T is left free, and for the other parameters the results of the first fit are used as starting values[8]. The log-likelihood values of the successfully fitted objects are compared and the optimised parameters of the object with the lowest $\ln L_{\text{set}}$ are kept. The double-fit procedure is redone for all pixels of the camera, starting with the previously optimised parameters. Using all camera pixels for the event reconstruction is a great advantage of this reconstruction method, allowing a more efficient γ-hadron separation at medium and high energies (see Section 4.1).

The results of the parameter optimisation of the example event are given in Table 3.4. Apparently the reconstructed values agree very well with the true values in this case. The only parameter that exhibits a greater deviation is the first interaction depth T. As already mentioned in Section 3.2, the reconstruction of this parameter is very complicated with a single telescope due to the larger degree of degeneracy. Table 3.4 also contains the error on each parameter as estimated with Eq. 3.40. The error values appear reasonable for this event, but generally their calculation strongly relies on the assumption of a quadratic shape of $\ln L_{\text{set}}$ and therefore may not always be exact.

The optimised intensities that are obtained when applying the model reconstruction to the example event are shown in Fig. 3.11 (*right panel*). Compared to the measured values (*left panel* in the figure), the modelled shower appears smoother and the peak intensities are lower. This is because the former contains statistical fluctuations while the latter is an average expectation. This aspect is already regarded in the likelihood calculation (Eq. 3.26) by using the Poissonian $P_\mu(n)$.

In this chapter, an in depth description of how to reconstruct the parameters of a VHE γ-ray by using the camera image of a single IACT was given. The next step is to quantify the performance by analysing a large sample of events. Furthermore, it is important to evaluate the agreement between a measured and modelled image in order to suppress the hadronic background and also remove events that were not properly reconstructed. These aspects will be discussed in the next chapter.

[8] This double-fit procedure was also introduced by the other two developers.

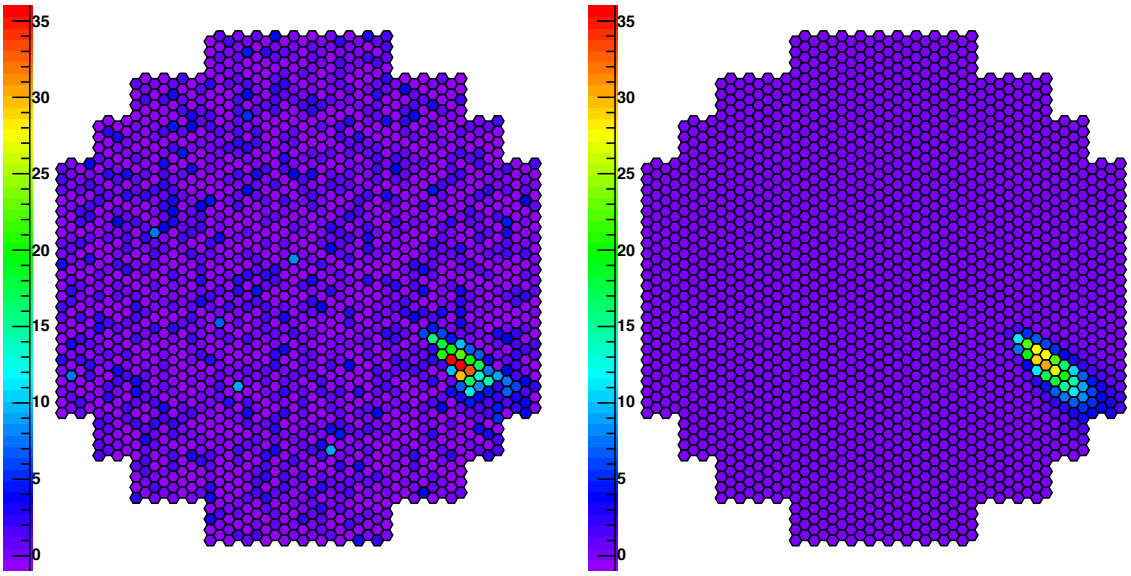

Fig. 3.11: *Left:* camera display, showing the intensity of the example event (identical to the left panel of Fig. 3.1, but shown again here for comparison). *Right:* optimised intensities as obtained from the model reconstruction.

4 Analysis Performance

The preceding chapter showed how to reconstruct the properties of VHE γ-rays using camera images of the H. E. S. S. II telescope. By applying this mechanism to a large sample of simulated events, it is possible to assess the overall performance of the analysis, which will be done in the following. Section 4.1 explains how to separate the γ-rays from the dominant hadronic background. The angular resolution of the analysis is treated in Section 4.2, followed by the energy bias and resolution in Section 4.3. The chapter closes with a description on how to estimate the sensitivity (Section 4.4).

4.1 γ-Hadron Separation

So far only γ-ray-initiated showers have been considered. However, compared to charged cosmic rays they contribute only a very small fraction of all particle showers that are generated in the Earth's atmosphere. In fact, most showers are generated by charged cosmic rays which mainly consist of protons. As already mentioned in Section 2.1, such hadronic showers evolve more irregularly than electromagnetic showers and result in a more irregular Cherenkov light distribution. This can, for example, be seen in the left panel of Fig. 4.1, which contains the intensity of the H. E. S. S. II camera for a simulated proton with an energy of almost 3 TeV. Despite the very large impact distance of nearly 400 m, the camera triggered and displays two sub-showers that were emitted towards the location of the telescope. As the image exhibits these two distinct sub-showers, where one

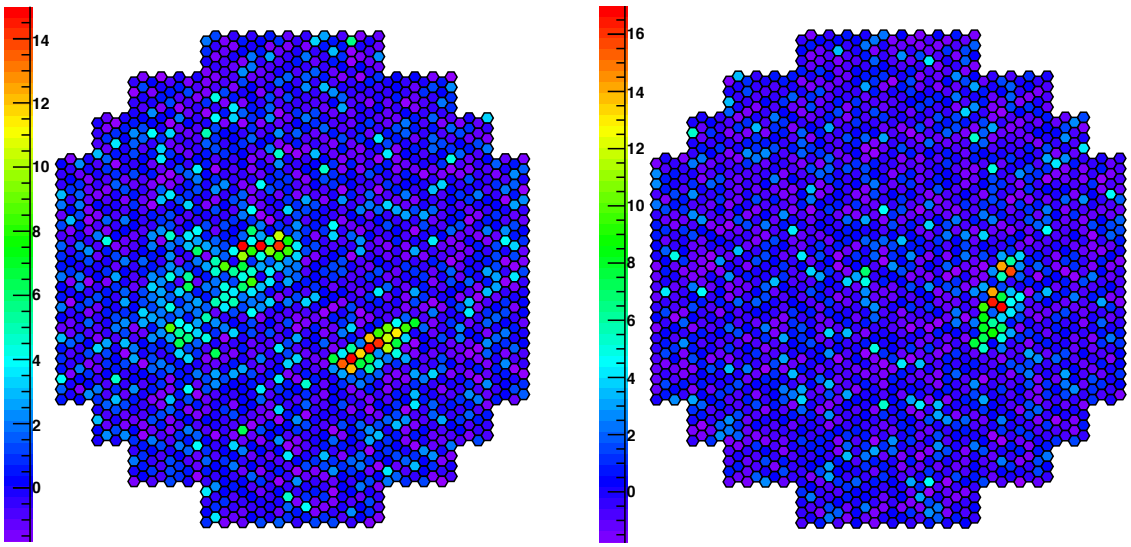

Fig. 4.1: H. E. S. S. II camera displays of two simulated proton events with moderate peak intensities. *Left:* impact distance of 391 m, energy of 2.95 TeV. *Right:* impact distance of 463 m, energy of 121 GeV.

of them (the upper left one) appears quite irregular, this event can even be classified by eye as background. Unlike that, the proton event shown in the right panel of Fig. 4.1 is more ambiguous. In spite of the comparably low energy of 121 GeV and the extremely large impact distance of more than 460 m, the camera was triggered because of a single subshower. The distribution of Cherenkov light does not look like a typical ellipse of a γ-ray, but showers of low-energy γ-rays are also subject to larger relative statistical variations which can lead to a similar shape. Generally it becomes very hard to distinguish between γ-rays and hadrons at low energies, especially if the event reconstruction and classification is done with only one telescope.

In order to classify events as γ- or background-like, there are several approaches. With the Hillas method (Section 3.2), one separation variable is the scaled width which is defined as

$$SW = \frac{W - W_{\mathrm{exp}}(Size, L)}{\sigma_W(Size, L)} \ . \tag{4.1}$$

Here, $W_{\mathrm{exp}}(Size, L)$ and $\sigma_W(Size, L)$ denote the mean and RMS of the width for γ-ray events with the same $Size$ and L and can be taken from lookup tables. Whereas the SW values of γ-ray events peak around 0 with an RMS of 1, background events are expected to cover a large value range as the cleaned camera image tends to be more irregular. It is thus possible to throw away a greater fraction of the background whilst keeping most of the γ-rays by only accepting events within a certain range of SW. The same classification is done for the Hillas length. Instead of manually selecting the cut values of the separation variables, machine-learning algorithms like e.g. *Boosted Decision Trees* can be used to optimise the performance of the analysis (Ohm et al. 2009). The sensitivity achievable with these methods is comparable to that of the model analysis.

In the model analysis, the γ-hadron separation is based on the average expected log-likelihood of each pixel, which is (de Naurois & Rolland 2009)

$$\langle \ln L \rangle \,|_\mu = \int \mathrm{d}s \ln L\,(s|\mu) \cdot P\,(s|\mu) \tag{4.2}$$

for a given model expectation μ. Since $\sigma^2\,(\ln L) \approx 2$, the *Goodness of Fit* for a set of pixels is defined as (de Naurois & Rolland 2009)

$$\mathcal{G}_{\mathrm{set}} = \frac{\sum_{i \in \mathrm{set}} \left[\ln L\,(s_i|\mu_i) - \langle \ln L \rangle \,|_{\mu_i}\right]}{\sqrt{2 \cdot \mathrm{NdF}}} \ , \tag{4.3}$$

where NdF is the number of degrees of freedom. Assuming that the pixel-wise goodness is a random variable, $\mathcal{G}_{\mathrm{set}}$ follows a normal distribution for γ-rays, i.e. $\langle \mathcal{G}_{\mathrm{set}} \rangle = 0$ and $\sigma^2\,(\mathcal{G}_{\mathrm{set}}) = 1$. *Goodness of Fit* values are computed for different pixel sets:

- G: overall goodness, using all available camera pixels.
- SG: shower goodness, taking the pixels of the cleaned image and two adjacent rows.
- BG: background goodness, calculated with all camera pixels that were not used for the shower goodness.

Additionally, the NSB likelihood is defined as

$$G_{NSB} = \frac{\sum_{i \in \mathrm{set}} \left[\ln L\,(s_i|0) - \langle \ln L \rangle \,|_0\right]}{\sqrt{2 \cdot \mathrm{NdF}}} \ . \tag{4.4}$$

Its value is thus correlated to the probability that the event was not caused by a γ-ray but by fluctuations of the NSB. G_{NSB} is thus not supposed to follow a normal distribution in the case of events that originate from γ-rays. By definition, it is almost always

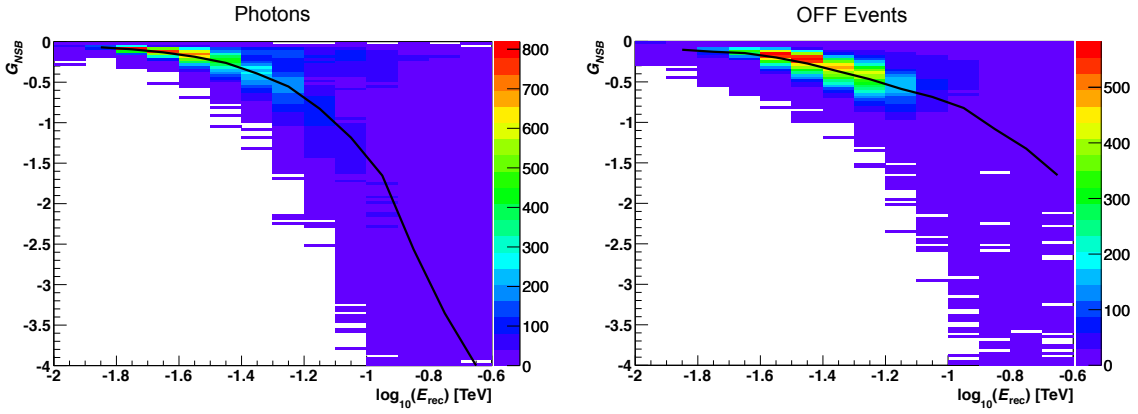

Fig. 4.2: G_{NSB} values of MC photons (*left panel*) and OFF events from real data (*right panel*) for different reconstructed energies. The simulated zenith angle of the photons is 18°, and the OFF events were taken from runs with zenith angles between 14° and 20°, respectively. In both plots, the solid black line corresponds to the mean G_{NSB} value of the respective energy bin.

negative, and a value of 0 means that the triggered event is perfectly compatible with NSB noise. Fig. 4.2 shows the distribution of G_{NSB} of both simulated photons and OFF (i.e. background) events from real data as a function of reconstructed energy. At energies $\gtrsim 100\,\mathrm{GeV}$, the mean of the distribution of the photons is generally located below that of the OFF events, but at lower energies both histograms appear very similar (i.e. a lot of showers of low-energy photons are compatible with NSB noise). Furthermore, it can be seen that using G_{NSB} as a selection variable has a direct influence on the energy threshold because the range of G_{NSB} (and particularly its lowest value) is directly correlated to the energy.

In order to account for deviations from the assumption of $\mathcal{G}_{\mathrm{set}}$ being a normal variable, each of the *Goodness of Fit* variables (except G_{NSB}) is rescaled (similar as the width in Eq. 4.1), using the expectation value and RMS from lookup tables. For example, the scaled shower goodness is defined as

$$SG_{\mathrm{sc}} = \frac{SG - SG_{\mathrm{exp}}\left(Size, R\right)}{\sigma_{SG}\left(Size, R\right)} \,. \tag{4.5}$$

The variables G_{sc} and BG_{sc} are calculated accordingly. Fig. 4.3 contains the distributions of SG_{sc} for simulated γ-rays and protons, respectively. For better comparison, the distributions are shown as a function of reconstructed rather than true energy. As expected from Eq. 4.5, the mean of SG_{sc} is close to 0 for the simulated photons and is independent of the energy. Most of the events exhibit values between -2 and 1. For the protons, SG_{sc} tends to be larger at reconstructed energies $\gtrapprox 100\,\mathrm{GeV}$, and the scatter around the mean is quite large. At lower energies, γ-hadron separation becomes more complicated since the proton distribution begins to resemble that of photons.

Before analysing sources, it is necessary to define suitable cut configurations and test their performances on simulations. The two configurations used in this thesis are defined in Table 4.1. For both of them, only events whose *CoG* lies within 1.4° distance from the camera centre are accepted. This helps to sort out events that are truncated by the camera border and thus cannot be properly reconstructed. Furthermore, only events with $Size > 60$ are used for the analysis in order to lessen systematic uncertainties. In

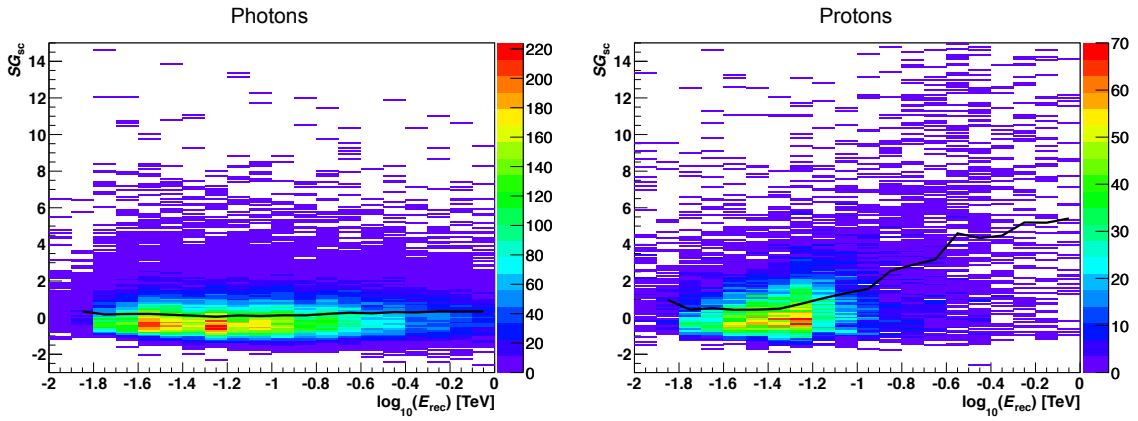

Fig. 4.3: Distribution of SG_{sc} values as a function of reconstructed energy for simulated photons and protons, respectively. The black line denotes the mean values of the scaled shower goodness for each energy bin in both histograms.

Table 4.1: *Standard* and *Loose* cut configuration of the single-telescope model analysis.

	Standard		*Loose*	
Parameter	Lower Cut	Upper Cut	Lower Cut	Upper Cut
$\lvert CoG\rvert$ [°]	0	1.4	0	1.4
$Size$	60	/	60	/
SG_{sc}	-3	0.9	-3	0.9
G_{NSB}	/	-1	*Not Used*	
T	-2	5	-2	5
ΔDir [°]	0	0.2	*Not Used*	

addition to these two pre-cuts, the configurations consist of four (*Standard*) respectively two (*Loose*) cuts that are specific to the model analysis. One of the cut parameters of the *Standard* configuration is the direction error which is defined as

$$\Delta Dir = \sqrt{2} \cdot \sqrt{\Delta x_S^2 + \Delta y_S^2} \ , \tag{4.6}$$

where Δx_S and Δy_S are the estimated errors on the source direction in the camera in units of degrees and are given by Eq. 3.40. All parameter ranges are independent of energy in this work.

The overall aim of the separation is to maximise the significance of a source. The approximate significance gain due to the separation is given by the quality factor

$$Q = \frac{\epsilon_\gamma}{\sqrt{\epsilon_{\mathrm{OFF}}}} \ , \tag{4.7}$$

where ϵ_γ is the ratio of MC γ-rays that pass the separation cuts to those before rejection. ϵ_{OFF} is defined correspondingly for OFF events from real data. Alternatively it is possible to use simulated protons to calculate the background rejection efficiency in Eq. 4.7. However, using the OFF data has the advantage that it also includes events that were triggered by NSB fluctuations.

Fig. 4.4 contains the values of Q for the *Standard* cuts as a function of reconstructed energy. In order to estimate the influence of the individual cuts, Q was also calculated for

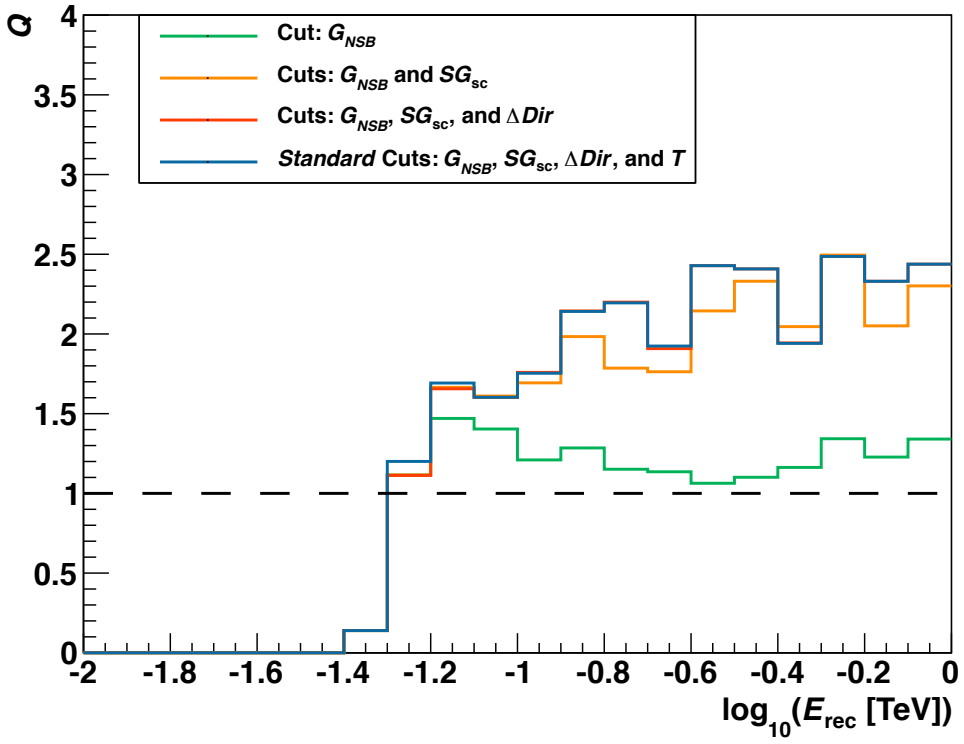

Fig. 4.4: Energy-dependent quality factor of the analysis for the *Standard* cut configuration (blue line) when observing at low zenith angles (18°). To illustrate the contribution of the individual cuts, the quality factor of different sub-configurations is also displayed. For each of the selection variables, the accepted range is independent of energy and given in Table 4.1.

several sub-configurations where cuts were added one at a time (the $|CoG|$ and *Size* cuts are included in all configurations). As expected from Fig. 4.2, using G_{NSB} as a selection variable has a direct influence on the energy threshold of the analysis. As for the *Standard* cuts at low zenith angles, it throws away all events with $E_{\mathrm{rec}} \lesssim 40\,\mathrm{GeV}$ (green line in Fig. 4.4). Compared to a direct cut on the reconstructed energy, the cut on the NSB likelihood has the advantage that the resulting energy threshold is automatically adapted to the zenith angle of the observation. In addition, it results in a quality factor > 1 above the energy threshold.

Adding the SG_{sc} cut leads to a considerable improvement of the quality factor at energies above 100 GeV (orange line). Including the direction error (red) does not change Q significantly, but using this cut helps to improve the angular resolution. Furthermore it must be mentioned that the OFF event statistics is very low at $\log_{10}(E_{\mathrm{rec}}) \gtrsim -0.3$ because of the preceding cuts. In case there are not enough background events left in the respective bin, Q is left unchanged in the calculation compared to the one without the cut; the calculated quality factor is thus underestimated in that case. The same affects the calculation of Q when including the cut on the first interaction depth (i.e. for the complete *Standard* cut configuration; blue line in the figure).

The energy-dependent quality factor for the *Loose* cut configuration is shown in Fig. 4.5. Since no cut on energy or NSB likelihood is being applied, Q is defined down to energies of $E_{\mathrm{rec}} \approx 10\,\mathrm{GeV}$. When taking the distributions from Fig. 4.3 and adjusting the upper

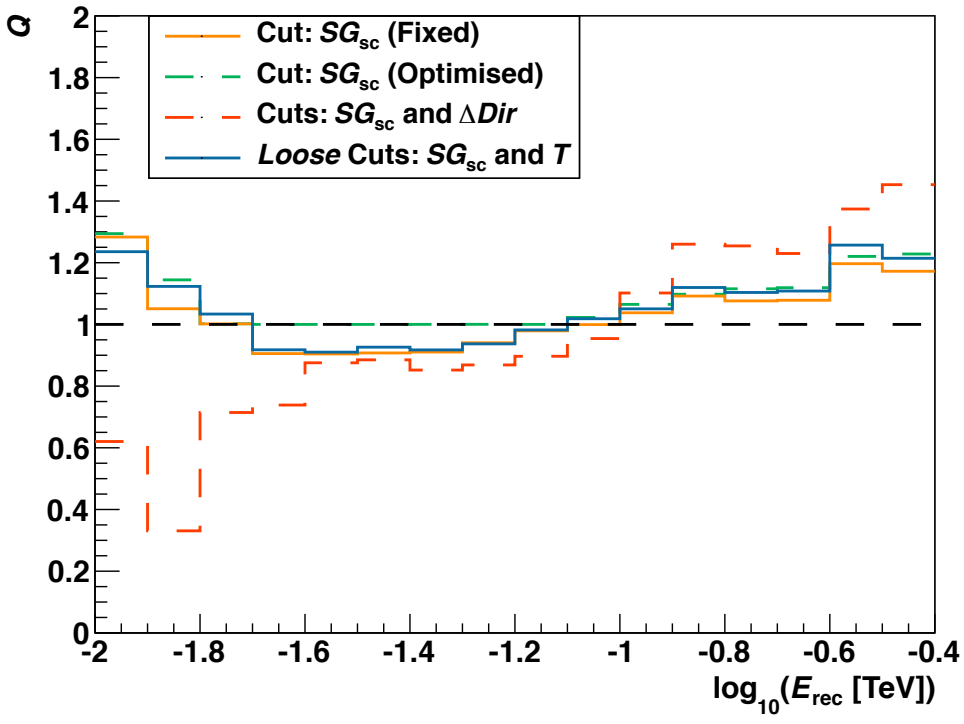

Fig. 4.5: Quality factor as a function of reconstructed energy for the *Loose* cut configuration (blue line), one sub-configuration (orange) as well as two alternative configurations (see text for further details). The calculations are valid for observations at low zenith angles.

limit of SG_{sc} in order to maximise Q, the resulting values are given by the dashed green line in the figure. Fixing the cut to 0.9 for all energies leads to only slightly lower values of Q (orange line). As can be seen, at low energies there is little gain in significance from the separation, as already inferred above from Fig. 4.3. When using ΔDir (same acceptance range as for the *Standard* cuts) instead of T as the second selection variable, the quality factor is represented by the dashed red line. While this configuration leads to larger Q values at higher energies, it performs very poorly at the lowest energies. This is, however, not very surprising as it just proves that the fit procedure correctly estimates larger uncertainties on the fitted source position in this energy regime.

Both cut configurations defined above serve different purposes and are, therefore, complementary. The *Standard* cuts provide a good γ-hadron separation at medium and higher energies at the expense of an increased energy threshold (which is, however, still way below the one of H. E. S. S. I, as will be shown later in this chapter). They are thus ideally suited to create sky maps and energy spectra of hard sources. Alternatively, the *Loose* cuts are designed to detect sources with a soft spectrum at the lowest energies that are currently accessible in ground-based γ-ray astronomy.

4.2 Angular Resolution

The next important performance criterion to be evaluated is the angular resolution of the analysis. A good angular resolution is not only useful to resolve spatial features,

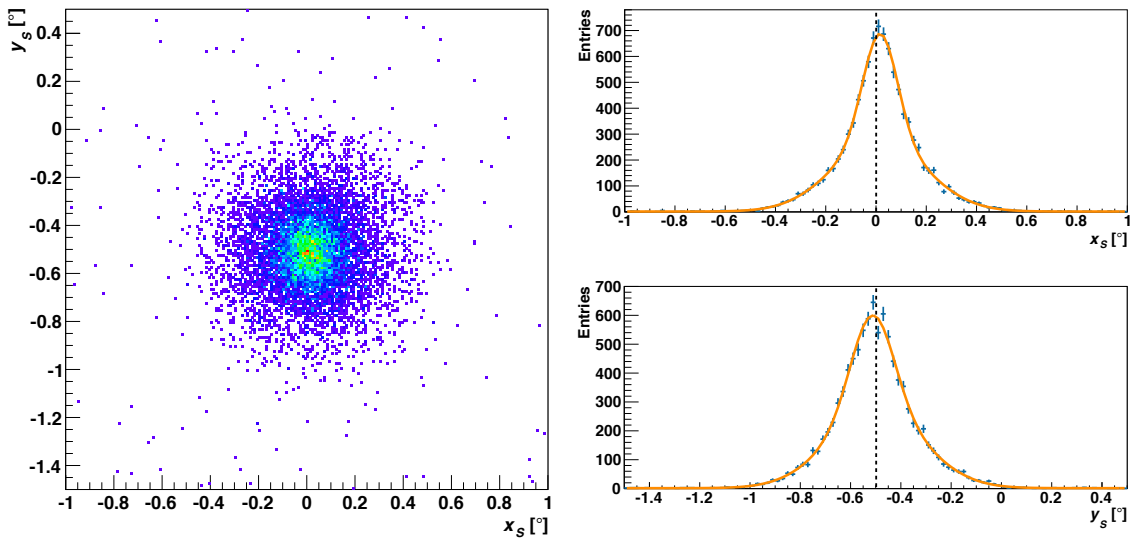

Fig. 4.6: Point spread function for simulated photons with an energy of 80 GeV, a zenith angle of 18°, and a wobble offset of 0.5° in the y direction. *Left:* two-dimensional distribution of all events that pass the γ-hadron separation (*Standard* cuts). *Right:* projections along x_S (upper panel) and y_S (lower panel). The distributions including error estimates are shown in blue. The result of a fit with two Gaussian functions and a constant is overlaid in orange. The dashed black line indicates the true direction.

but also leads to an improved sensitivity. In the following, the angular separation of the reconstructed and the true source direction is examined for a simulated point source. In order to study the energy dependence of the point spread function (PSF), γ-rays were simulated for several fixed energies. Only events that pass the γ-hadron separation cuts (see previous section) are used for the evaluation of the PSF. The simulated pointing offset from the camera centre (henceforth called wobble offset) was set to 0.5° along the y direction.

The two-dimensional distribution of reconstructed directions of γ-rays with an energy of 80 GeV and a zenith angle of 18° is shown in the left part of Fig. 4.6 (after applying *Standard* cuts). Despite the wobble offset and the fact that the analysis is conducted with only one telescope, the PSF appears circularly symmetric. The right part of Fig. 4.6 contains the projections of the distribution along x_S and y_S, respectively. A superposition of two Gaussian functions and a constant was fitted to each of them[1]:

$$f(x_S) = A \cdot \exp\left(\frac{(x_S - x_{01})^2}{2\sigma_1^2}\right) + B \cdot \exp\left(\frac{(x_S - x_{02})^2}{2\sigma_2^2}\right) + C \ . \tag{4.8}$$

The fit results are given in Table 4.2. As can be seen, σ_1 is significantly larger for y_S than for x_S, but the deviation is not large enough to make the 2D PSF appear asymmetric. In order to calculate the angular resolution for different energies, the PSF is thus approximated by two radially symmetric Gaussian functions (without offset) and a constant. This function is then fitted to the ϑ^2 distribution (where ϑ corresponds to the angular distance between reconstructed and true source direction), which generally extends from 0.00 deg^2 to 1.00 deg^2 in this work. For the events with 80 GeV, the ϑ^2 distribution together with

[1] In the equation, x_S has to be replaced with y_S for the projection along the y axis.

Table 4.2: Results of the fits to the x and y projections of the PSF shown in Fig. 4.6 and to the ϑ^2 distribution (Fig. 4.7). The parameter definitions are given in Eq. 4.8.

Parameter	Fit to x Projection	Fit to y Projection	Fit to ϑ^2 Distribution
A	419 ± 16	341 ± 19	1566 ± 53
x_{01} [°]	0.017 ± 0.002	-0.513 ± 0.003	/
σ_1 [°]	0.068 ± 0.003	0.085 ± 0.004	0.075 ± 0.002
B	267 ± 14	259 ± 18	460 ± 19
x_{02} [°]	0.013 ± 0.003	-0.500 ± 0.003	/
σ_2 [°]	0.185 ± 0.003	0.188 ± 0.004	0.184 ± 0.002
C	1.3 ± 0.2	1.5 ± 0.2	0.5 ± 0.1
χ^2/NDoF	97/93	97/93	156/195

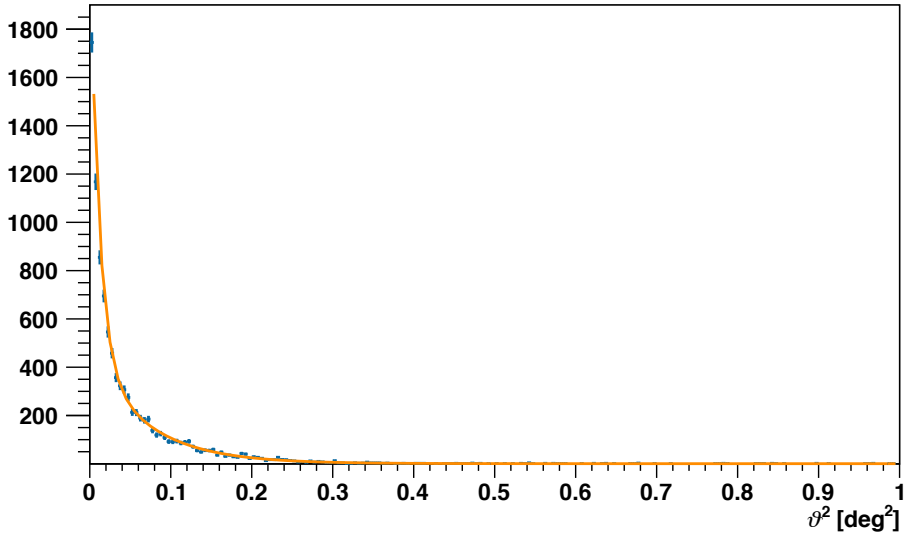

Fig. 4.7: ϑ^2 distribution of the events shown in Fig. 4.6. The histogram entries including error estimates are shown in blue, and the fit to the distribution is illustrated with an orange line.

the fit is shown in Fig. 4.7. As for the projections, the fit results are given in Table 4.2. The good χ^2/NDoF value of the fit to the ϑ^2 distribution justifies the simplification to a radially symmetric PSF in this case.

The angular resolution is calculated via numerical integration of the fit function. In real data, the events that form the constant of the function are expected to be lost during the spatial background subtraction and are thus irrelevant for the angular resolution. Therefore only the two Gaussian functions are used for the integration. First, the overall integral is computed (i.e. from $\vartheta^2 = 0\,\mathrm{deg}^2$ to infinity). Performing a second integration, the upper bound is decreased until the value of the integral is just 68% of the value of the first integration. The square root of this upper bound is then defined as the 68% containment radius ϑ_{68}. The values of ϑ_{68} for different energies are shown in Fig. 4.8 for the zenith angles 18° and 46° and for both cut configurations. The angular resolution for *Loose* cuts is not as good as for *Standard* cuts, which should be regarded as a tradeoff

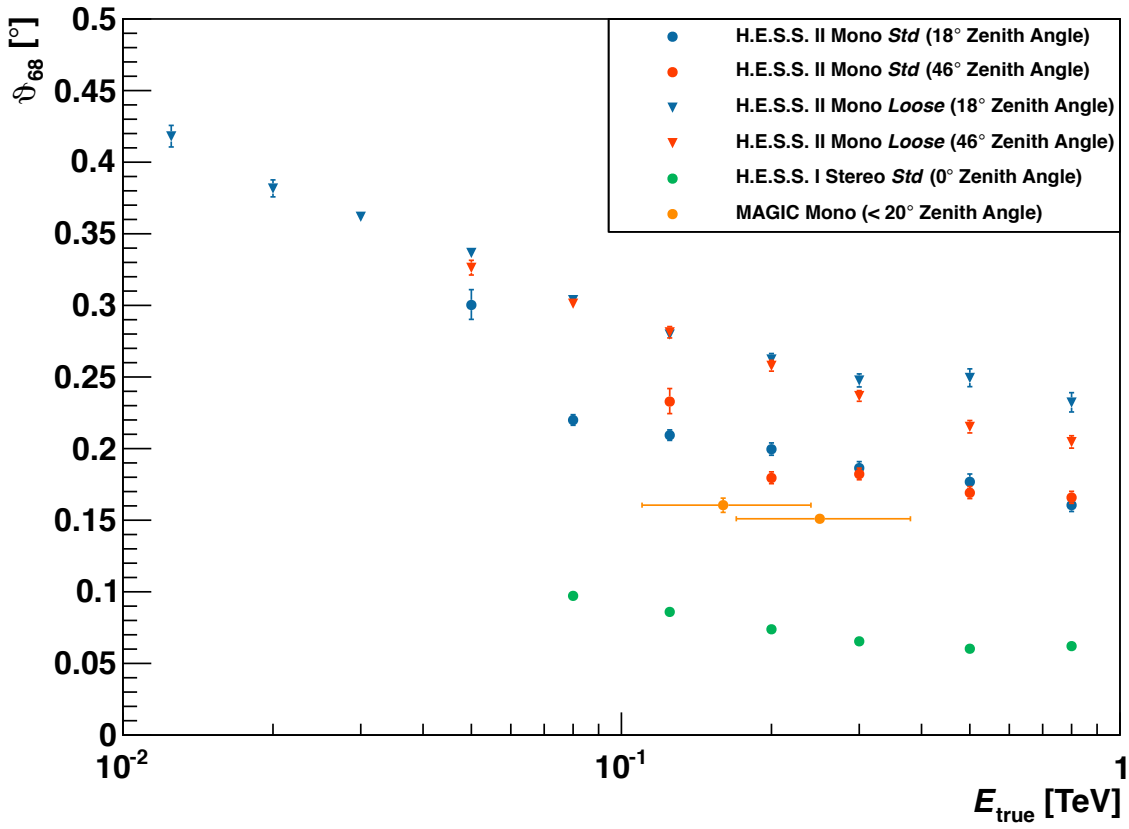

Fig. 4.8: Angular resolution from simulations for different energies. The blue and red points correspond to the results from this work (circles stand for *Standard* and triangles for *Loose* cuts, respectively), whereas the green points are the 68% containment radii for the stereoscopic model analysis with H. E. S. S. I which were taken from de Naurois & Rolland (2009). The angular resolution of the single-telescope reconstruction from MAGIC I (Albert et al. 2008a) is shown in orange. The values in the reference correspond to 39% containment (σ of a single Gaussian function fitted to the ϑ^2 distribution), so they are scaled by a factor of 1.51 in this figure in order to result in 68% containment.

for the much lower energy threshold of the former. Interestingly, the PSF appears to be mostly independent of the zenith angle. Because of the missing stereoscopic information, the ϑ_{68} values of H. E. S. S. II are considerably larger than those of H. E. S. S. I (shown in green, taken from de Naurois & Rolland (2009)). Compared to the single-telescope reconstruction from MAGIC I (orange points, taken from Albert et al. (2008a)), even the *Standard*-cut results from this work are slightly worse in the respective energy range, which can be entirely accounted for by the different determination of the angular resolution (both the extents of the ϑ^2 distributions as well as the adopted fit functions are different). To check this, the values for $E_{\text{true}} = 125\,\text{GeV}$ and $E_{\text{true}} = 200\,\text{GeV}$ were re-calculated with the method adopted by Albert et al. (2008a) and are consistent within errors with the ones given in that reference.

Based on the values of the angular resolution, a maximum ϑ^2 value is added to the cut parameters, which is necessary to calculate the significance of a source. For their standard cut configuration, de Naurois & Rolland (2009) use $\vartheta^2_{\text{max}} = 0.01\,\text{deg}^2$. Due to the lower

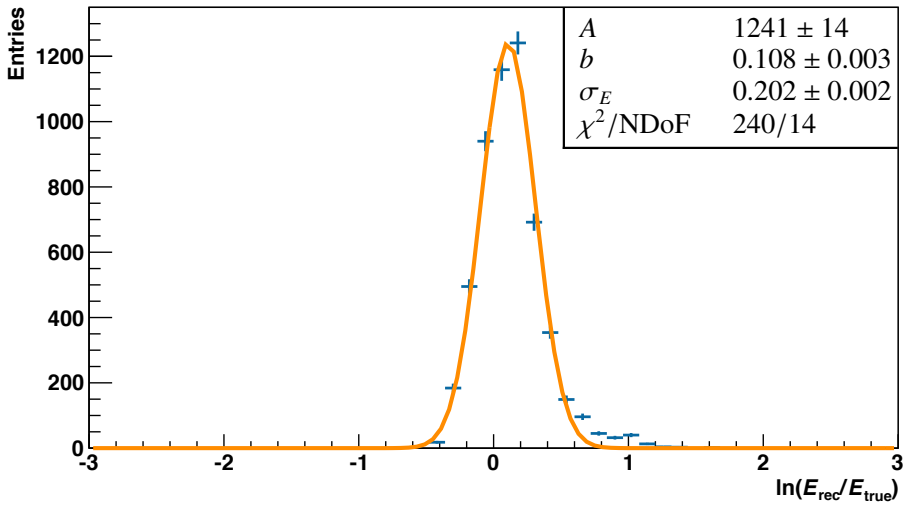

Fig. 4.9: Distribution of $\ln(E_{\mathrm{rec}}/E_{\mathrm{true}})$ for simulated γ-rays with $E_{\mathrm{true}} = 80\,\mathrm{GeV}$, 0.5° wobble offset, and 18° zenith angle after applying *Standard* cuts. The orange line corresponds to the result of a fit with a Gaussian function. The fit parameters are shown on the upper right.

angular resolution of this analysis, $\vartheta^2_{\mathrm{max}}$ was set to $0.03\,\mathrm{deg}^2$ for the *Standard* cuts, and to $0.06\,\mathrm{deg}^2$ for the *Loose* cuts.

4.3 Energy Bias and Resolution

When calculating the energy spectrum of a source, it is necessary to understand the analysis performance in terms of the energy reconstruction, which is being done in the following. This study was conducted similar to that of the angular resolution in the previous section. Simulations of γ-rays with fixed energies were analysed and the previously introduced γ-hadron separation cuts applied. For each true energy, the values of $\ln(E_{\mathrm{rec}}/E_{\mathrm{true}})$ are filled into a histogram.

Fig. 4.9 contains the histogram for photons with a true energy of 80 GeV, 0.5° wobble offset, and 18° zenith angle after applying *Standard* cuts. The entries of the histogram are shown including Poissonian error estimates. The distribution was fitted with a Gaussian function,

$$f(r_E) = A \cdot \exp\left(\frac{(r_E - b)^2}{2\sigma_E^2}\right) , \tag{4.9}$$

where $r_E = \ln(E_{\mathrm{rec}}/E_{\mathrm{true}})$. The function as well as the fit results are also shown in the figure.

The values of the energy bias b and the 68% resolution σ_E for different energies and for both cut configurations are shown in the upper and lower panel of Fig. 4.10, respectively. For comparison, the values from the H. E. S. S. I model analysis (from de Naurois & Rolland (2009)) are also drawn in both plots. As for the energy bias, a common feature of all distributions shown here is an overshoot near the respective energy thresholds. For the H. E. S. S. II analysis at low zenith angles, $|b|$ does not exceed 0.1 at all energies down to 80 GeV for *Standard* cuts and 30 GeV for *Loose* cuts, emphasising the capabilities at

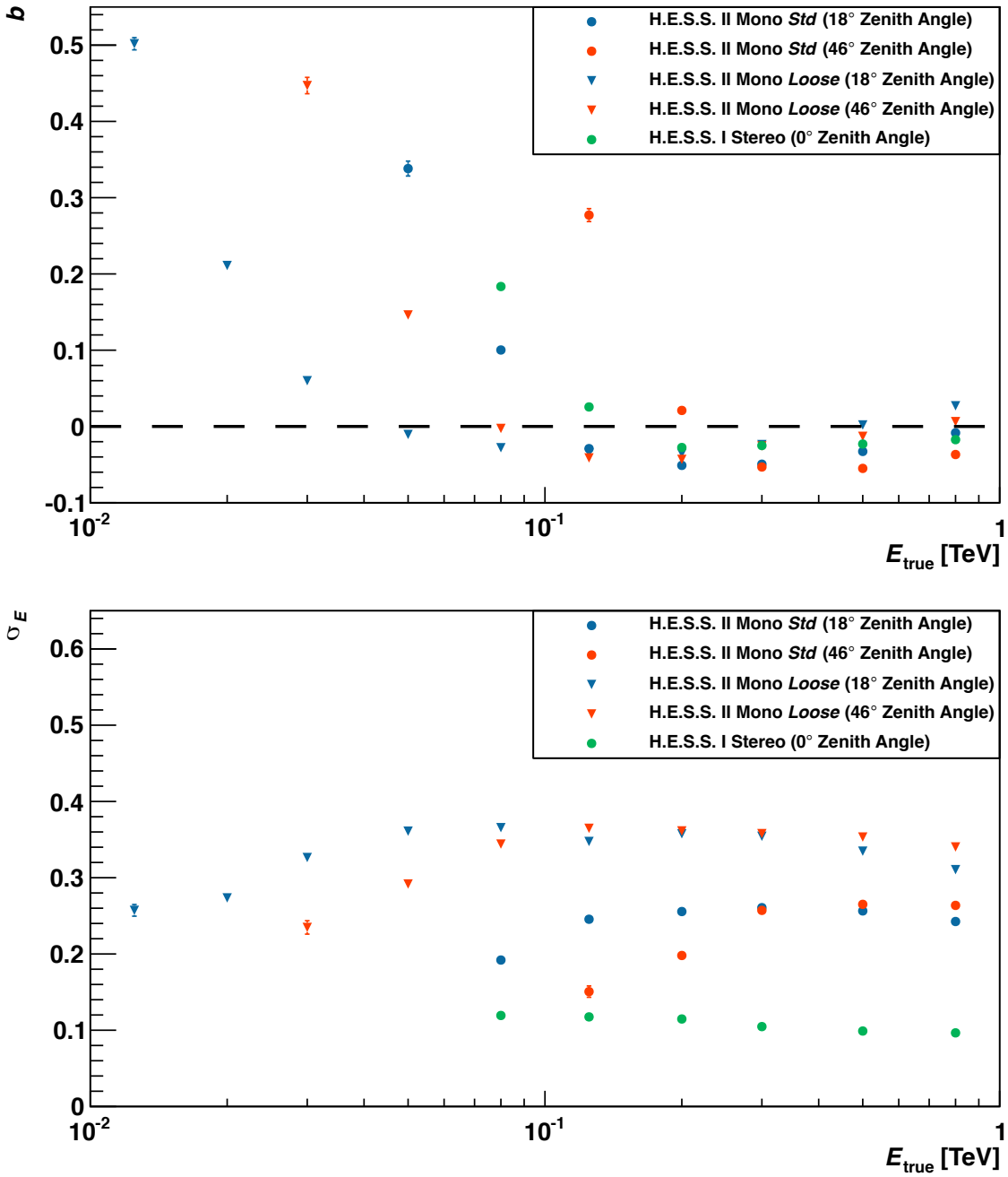

Fig. 4.10: Energy bias (upper panel) and resolution (lower panel) for different energies. The color coding is given in the figure legends. The H. E. S. S. I values were taken from de Naurois & Rolland (2009). b and σ_E are defined in Eq. 4.9.

low energies. At 46° zenith angle, the overshoot is shifted to higher energies due to the increased energy threshold. As for the energy resolution σ_E and for a given cut configuration, there is little difference between the results for both zenith angles. As expected, *Standard* cuts generally provide a better energy resolution because of the tighter event selection. Because of the degeneracy of impact distance and energy reconstruction in the case of only one telescope, the resolution is not as good as for H. E. S. S. I.

4.4 Sensitivity

The final performance characteristic to be determined is the sensitivity of the analysis, which corresponds to the minimum flux of a point-like source that can still be detected significantly within a given time. It strongly depends on other performance criteria, such as the γ-hadron separation and the angular resolution.

For the calculation of the sensitivity, simulated photons, protons, and electrons with a zenith angle of $\theta = 18°$ and an azimuth angle of 180° were analysed[2]. The energies of the events of the simulated photons and electrons are in the range $(5\,\mathrm{GeV}/\cos\theta) - (100\,\mathrm{TeV}/\cos\theta)$, whereas the minimum energy is $(30\,\mathrm{GeV}/\cos\theta)$ in case of the protons. The impact points are randomly distributed around the H. E. S. S. II telescope, and the maximum impact distance was set to $r_{\mathrm{sim}} = (600\,\mathrm{m}/\cos\theta)$ for all particle types. The optical efficiency of the detector was set to 100%. While the photons were simulated at a fixed direction with 0.5° wobble offset (just as for the previous studies), the directions of the protons and electrons scatter around the camera centre up to an angle of $\phi_{p/e} = 5°$.

The simulated events were analysed both with the *Standard* and *Loose* cut configurations that were described in Section 4.1. All subsequent calculations were carried out using ten bins per decade in energy. For each particle type, a two-dimensional histogram with variables $\log_{10}(E_{\mathrm{rec}})$ and $\log_{10}(E_{\mathrm{true}})$ is filled with the events that pass the separation cuts. This histogram is called the migration matrix $\mathbf{M}$. In the following, the nomenclature is such that e.g. $\mathrm{M}_{ji} = \mathrm{M}(E_{\mathrm{true},j}, E_{\mathrm{rec},i})$ corresponds to the entry of the migration matrix at the j-th bin of $\log_{10}(\mathrm{E}_{\mathrm{true}})$ and the i-th bin of $\log_{10}(\mathrm{E}_{\mathrm{rec}})$, respectively. The index j shall always denote an energy bin in the n_{true}-dimensional *simulation/theoretical space*, and i a bin of the n_{rec}-dimensional *detection space*.

In order to estimate the sensitivity of the analysis, it is first necessary to calculate its response using the information given by the simulations. In case of the MC analysis, the reconstruction and analysis performs the following mapping from the *simulation space* to the *detection space*:

$$\vec{N}_{\mathrm{det}} = \vec{N}^{\mathrm{T}}_{\mathrm{sim}} \cdot \mathbf{R} \ . \tag{4.10}$$

In this equation, the histogram $\vec{N}_{\mathrm{det}}$ can be regarded as a vector with n_{rec} dimensions, which is obtained by multiplying the n_{true}-dimensional vector $\vec{N}^{\mathrm{T}}_{\mathrm{sim}}$ with the $(n_{\mathrm{true}} \times n_{\mathrm{rec}})$ response matrix $\mathbf{R}$. For a specific bin i in reconstructed energy, Eq. 4.10 reads

$$N_{\mathrm{det},i} = \sum_j N_{\mathrm{sim},j} \cdot \mathrm{R}_{ji} \ . \tag{4.11}$$

By definition,

$$\sum_j \mathrm{M}_{ji} = N_{\mathrm{det},i} \ , \tag{4.12}$$

[2]To be specific, the zenith angle of the electrons is 0°. The influence of this slight discrepancy should be negligible and, if measurable within the given statistics, even results in a more conservative sensitivity estimate.

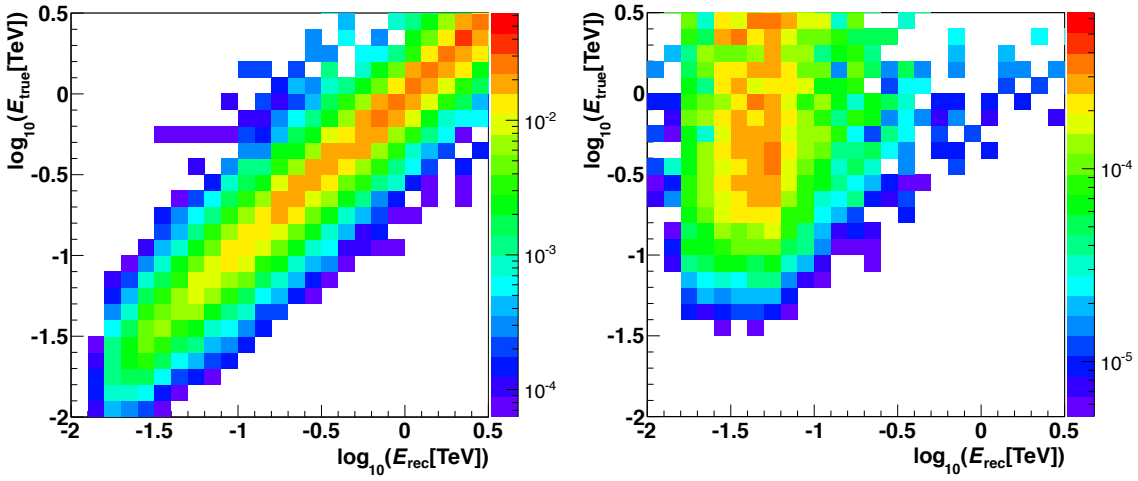

Fig. 4.11: Extracts of the response matrices of photons (left) and protons (right) for $\theta = 18°$ when applying *Loose* cuts. For better visibility, the colour scale is logarithmic.

and combining Eq. 4.11 and Eq. 4.12 then leads to

$$\mathrm{R}_{ji} = \frac{\mathrm{M}_{ji}}{N_{\mathrm{sim},j}} \ . \tag{4.13}$$

The response matrix combines the energy migration and the detection efficiency of the analysis. As an example, Fig. 4.11 contains extracts of the response matrices of photons and protons for $\theta = 18°$ when using the *Loose* cut configuration. As for the photons, the reconstructed energies are distributed around the true values. In contrast, the proton matrix looks more irregular, and the reconstructed energies are generally lower than the true energies.

In order to calculate the sensitivity, it is necessary to assume a spectral distribution for each particle type. For γ-rays, the spectrum of the Crab Nebula as published in Aharonian et al. (2006a) is used,

$$\frac{\mathrm{d}N_\gamma}{\mathrm{d}A\,\mathrm{d}E\,\mathrm{d}t} = 3.76 \times 10^{-7} \times E_{\mathrm{true}}^{-2.39} \times \exp\left(\frac{E_{\mathrm{true}}}{14.3\,\mathrm{TeV}}\right) \frac{1}{\mathrm{m}^2\,\mathrm{s}\,\mathrm{TeV}} \ . \tag{4.14}$$

The diffuse proton flux is assumed to have the following spectral shape (Becherini & Kosack (private communication)):

$$\frac{\mathrm{d}N_\mathrm{p}}{\mathrm{d}A\,\mathrm{d}E\,\mathrm{d}t\,\mathrm{d}\Omega} = 0.096 \times 1.1 \times E_{\mathrm{true}}^{-2.7} \frac{1}{\mathrm{m}^2\,\mathrm{s}\,\mathrm{TeV}\,\mathrm{sr}} \ . \tag{4.15}$$

The factor 1.1 is used to correct the flux in order to take into account contributions from heavier nuclei. The electron flux is given by (Becherini & Kosack (private communication))

$$\begin{aligned}\frac{\mathrm{d}N_\mathrm{e}}{\mathrm{d}A\,\mathrm{d}E\,\mathrm{d}t\,\mathrm{d}\Omega} \quad = \quad & \left[6.85 \times 10^{-5} \times E_{\mathrm{true}}^{-3.21} + \frac{3.186 \times 10^{-3}}{E_{\mathrm{true}} \times 0.776 \times \sqrt{2\pi}} \times \right. \\ & \left. \times \exp\left(-0.5\left(\frac{\ln E_{\mathrm{true}} - \ln 0.107}{0.776}\right)^2\right)\right] \frac{1}{\mathrm{m}^2\,\mathrm{s}\,\mathrm{TeV}\,\mathrm{sr}} \ . \end{aligned} \tag{4.16}$$

The next step is to calculate the number of photons per area for each energy bin:

$$\frac{\mathrm{d}N^{\mathrm{theo}}_{\gamma,j}}{\mathrm{d}A} = T \times \int_{E_{j,\mathrm{low}}}^{E_{j,\mathrm{up}}} \frac{\mathrm{d}N_\gamma}{\mathrm{d}A\,\mathrm{d}E_{\mathrm{true}}\,\mathrm{d}t}\,\mathrm{d}E_{\mathrm{true}}\ , \tag{4.17}$$

where T is the observation time and $E_{j,\mathrm{low}}$ and $E_{j,\mathrm{up}}$ correspond to the energies at the lower and upper edge of bin j, respectively. For the electrons and protons, the computation proceeds correspondingly, but the values are still given per solid angle.

Having calculated $\mathbf{R}_{\gamma/p/e}$, the goal is to derive relations that are similar to Eq. 4.10 but take the theoretical particle distributions as an input (see Eq. 4.17):

$$\vec{N}_\gamma = \left(\frac{\mathrm{d}\vec{N}^{\mathrm{theo}}_\gamma}{\mathrm{d}A}\right)^{\mathrm{T}} \cdot \widetilde{\mathbf{R}}_\gamma \quad , \quad \vec{N}_{p/e} = \left(\frac{\mathrm{d}\vec{N}^{\mathrm{theo}}_{p/e}}{\mathrm{d}A\,\mathrm{d}\Omega}\right)^{\mathrm{T}} \cdot \widetilde{\mathbf{R}}_{p/e}\ . \tag{4.18}$$

Applying the absolute detection efficiencies of Eq. 4.13 to the area in which the γ-rays were simulated, the flux response matrix $\widetilde{\mathbf{R}}_\gamma$ is calculated as

$$\widetilde{\mathrm{R}}_{\gamma,ji} = \frac{\mathrm{M}_{\gamma,ji}}{N^{\mathrm{sim}}_{\gamma,j}/r^2_{\mathrm{sim},\gamma}\pi} = \mathrm{R}_{\gamma,ji} \times r^2_{\mathrm{sim},\gamma}\pi\ . \tag{4.19}$$

The effective area as a function of true energy is then simply given by

$$A_{\mathrm{eff},\gamma,j} = \sum_i \widetilde{\mathrm{R}}_{\gamma,ji}\ . \tag{4.20}$$

Fig. 4.12 shows $A_{\mathrm{eff},\gamma}(E_{\mathrm{true}})$ for the H. E. S. S. II telescope for both the *Standard* and the *Loose* cut configuration. At the energy threshold, the effective area for *Standard* cuts is basically identical to the one of MAGIC I (Albert et al. 2008a). For larger energies, it lies below the ones of H. E. S. S. I (taken from de Naurois & Rolland (2009)) and also MAGIC I, indicating that the event selection is rather tight. The effective area for the *Loose* cut configuration is much bigger. It exhibits acceptable values down to an energy of only 10 GeV and already surpasses 10% of its maximum value by $E_{\mathrm{true}} < 30\,\mathrm{GeV}$.

For the protons and electrons, it is necessary to consider the following when calculating the flux response matrices $\widetilde{\mathbf{R}}$:

- as the particles are simulated within a certain solid angle $\Omega^{\mathrm{sim}}_{p/e} = 2\pi(1-\varphi_{p/e})$, $\vec{N}_{\mathrm{sim}}$ is divided by this value. This is completely analogous to the scaling with the simulation area.
- the solid angles of the analysis regions (defined by the respective $\vartheta^2_{\mathrm{max}}$ cut) of photons, protons, and electrons may be different (actually we are only interested in the flux of protons and electrons within the analysis regions of the photons). The flux response matrices of protons and electrons thus have to be scaled by $\Omega^{\mathrm{det}}_\gamma/\Omega^{\mathrm{det}}_{p/e} = (1-\vartheta_{\mathrm{max},\gamma})\,/(1-\vartheta_{\mathrm{max},(p/e)})$.

The entries of $\widetilde{\mathbf{R}}_{p/e}$ are then given by

$$\begin{aligned}\widetilde{\mathrm{R}}_{(p/e),ji} &= \frac{\mathrm{M}_{(p/e),ji}}{N^{\mathrm{sim}}_{(p/e),j}/\left(r^2_{\mathrm{sim},(p/e)}\pi \cdot \Omega^{\mathrm{sim}}_{(p/e)}\right)} \cdot \frac{\Omega^{\mathrm{det}}_{\gamma,j}}{\Omega^{\mathrm{det}}_{(p/e),j}} \\ &= \mathrm{R}_{(p/e),ji} \times r^2_{\mathrm{sim},(p/e)}\pi \cdot \Omega^{\mathrm{sim}}_{(p/e)} \cdot \frac{\Omega^{\mathrm{det}}_{\gamma,j}}{\Omega^{\mathrm{det}}_{(p/e),j}}\ .\end{aligned} \tag{4.21}$$

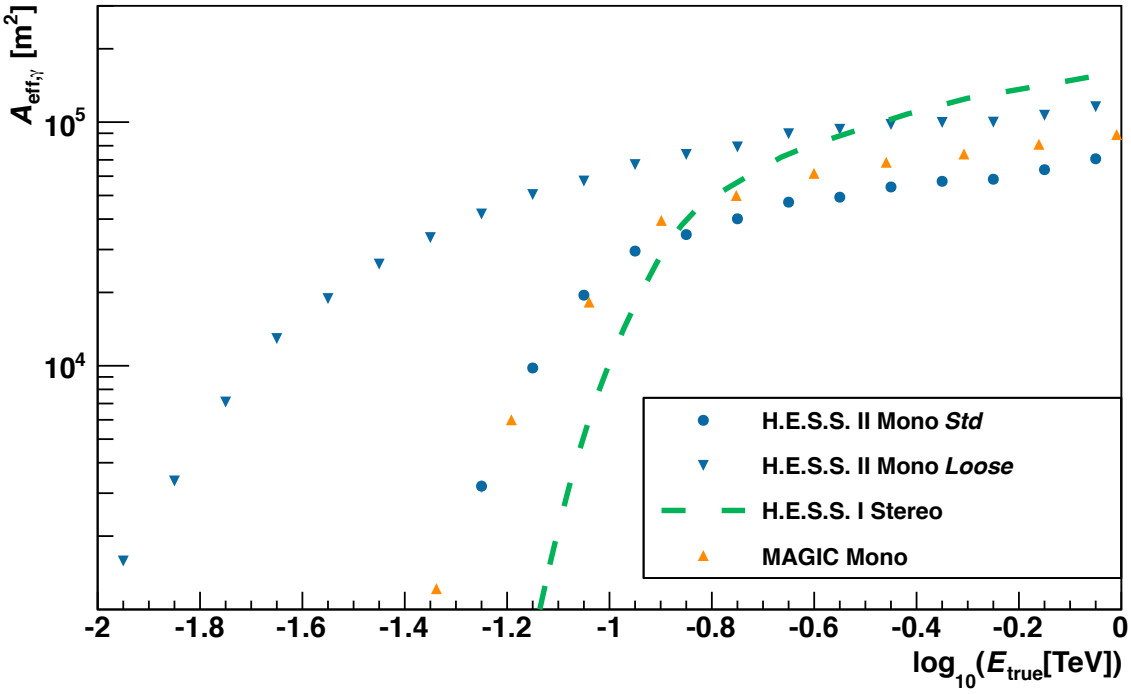

Fig. 4.12: Effective photon collection area (after γ-hadron separation) of different experiments for observations at low zenith angles. The MAGIC values were taken from Albert et al. (2008a), and the H. E. S. S. I ones correspond to *Standard* cuts as published in de Naurois & Rolland (2009).

Instead of calculating the background from simulations, it can alternatively be extracted using OFF events of real observations. For the sensitivity calculation at $\theta = 18°$, good-quality observations of the active galactic nucleus (AGN) PKS 2155-304 with a live time of $T_{\mathrm{OFF}} = 6.4\,\mathrm{h}$ were used. The selected runs were taken at zenith angles between 14° and 20°. Fig. 4.13 contains the energy distribution of OFF events of this data set for both *Standard* (*left panel*) and *Loose* cuts (*right panel*). The distributions are scaled to match the solid angle of the $\vartheta^2_{\mathrm{max}}$ cut that is used for the respective analysis configuration. For comparison, Fig. 4.13 also shows the expected proton and electron background for $T = T_{\mathrm{OFF}}$ as calculated from Eq. 4.18. As can be seen for *Standard* cuts, the simulated background matches reasonably well with the data at reconstructed energies above 100 GeV. At lower energies, the prediction overestimates the measurement. This might be explained by the fact that the simulations are generated for an ideal relative optical efficiency of 100%. As for the *Loose* cuts, the MC distribution is close to the measured one for $\log_{10}(E_{\mathrm{rec}}) > -1.3$ (corresponding to 50 GeV). Just as for the *Standard* cuts, the prediction is too large at very low energies. The good agreement between simulations and data for both cut configurations (apart from the respective threshold regime) indicates that the understanding of both the detector and the analysis are quite advanced. Due to the better statistics, only the OFF background is going to be used in the following sensitivity calculation.

The significance of a source with the flux and spectrum of the Crab Nebula for each $E_{\mathrm{rec},i}$ bin is calculated as

$$S_i = \frac{N_{\gamma,i}}{\sqrt{N_{\mathrm{bkg},i}}} \,, \tag{4.22}$$

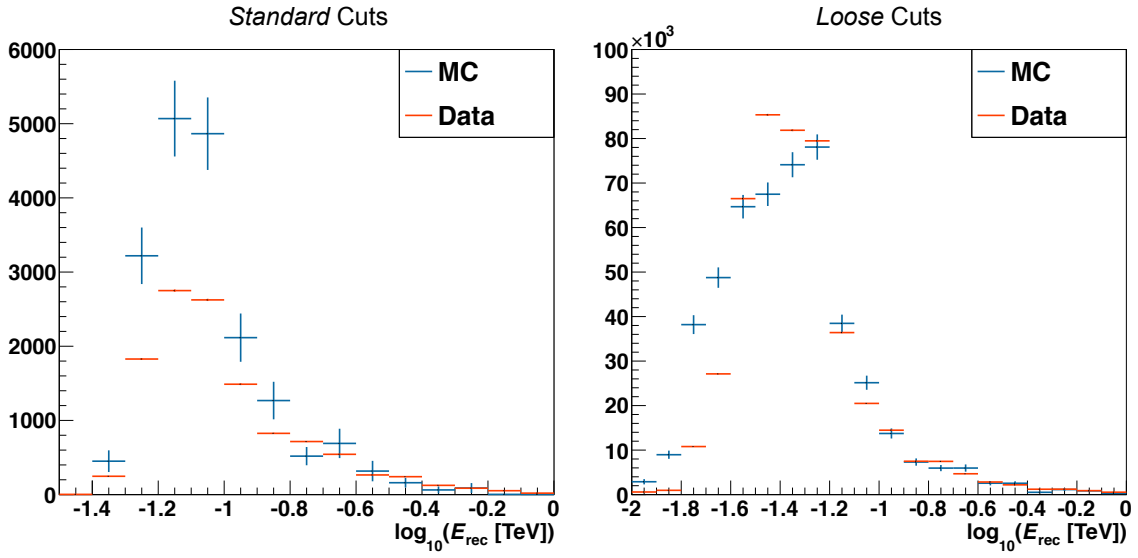

Fig. 4.13: Expected (blue) and measured (red) number of background events as a function of reconstructed energy for *Standard* (*left*) and *Loose* cuts (*right*). Please note that the statistical errors of the measured events are also drawn but hardly visible due to the large statistics. The simulations are generated for a relative optical efficiency of 100%, which could explain part of the difference at lower energies in both panels.

where $N_{\mathrm{bkg},i} = N_{\mathrm{OFF},i} \cdot T/T_{\mathrm{OFF}}$. Requiring a detection significance of 5σ, the differential sensitivity (i.e. the sensitivity for each bin) is simply $5\sigma/S_i$.

The differential sensitivity of the analysis presented in this thesis is shown in Fig. 4.14 for an observation time of 100 hours for both cut configurations. The results where rebinned to five bins per decade, and the minimum number of photons in each bin was set to 10. In order to account for systematic uncertainties in the background determination, $N_\gamma\left(E_{\mathrm{rec},i}\right) \geq f \cdot N_{\mathrm{bkg}}\left(E_{\mathrm{rec},i}\right)$ was required. In order not to overestimate the performance of the analysis, a conservative threshold of $f = 0.05$ is appropriate for normal analyses. Except for the lowest energies, the *Standard* cuts are superior to the *Loose* cuts in this case. For comparison, Fig. 4.14 also contains the differential sensitivity of H. E. S. S. I for $f = 0.05$ as shown in Funk et al. (2013). At medium energies, the sensitivity of H. E. S. S. II using *Standard* cuts is not as good as the one of H. E. S. S. I due to the missing stereoscopic information, but the sensitivity is defined to much lower energies. The differential sensitivity is also displayed for $f = 0.00$, assuming that there are no systematic uncertainties on the background. This is valid for pulsar observations where it is possible to use the phasogram to define ON and OFF regions. The *Loose* cut set performs very well at low energies, implying that H. E. S. S. II is a very sensitive instrument to detect pulsed emission. The sensitivity is indeed located distinctly below the best-fit spectrum of the Vela pulsar as measured with Fermi-LAT (Tavernier (private communication)). As this source can be observed with H. E. S. S. II at $\theta \geq 22°$ (i.e. only slightly larger than the zenith angle used for this sensitivity estimate), it should be significantly detectable in a reasonable amount of time with the *Loose* cuts introduced here.

With the lower energy threshold, H. E. S. S. II reaches energies which were previously only accessible to space-based satellites like the Fermi-LAT. This instrument is almost background-free at GeV energies, but its effective area is several magnitudes below that of

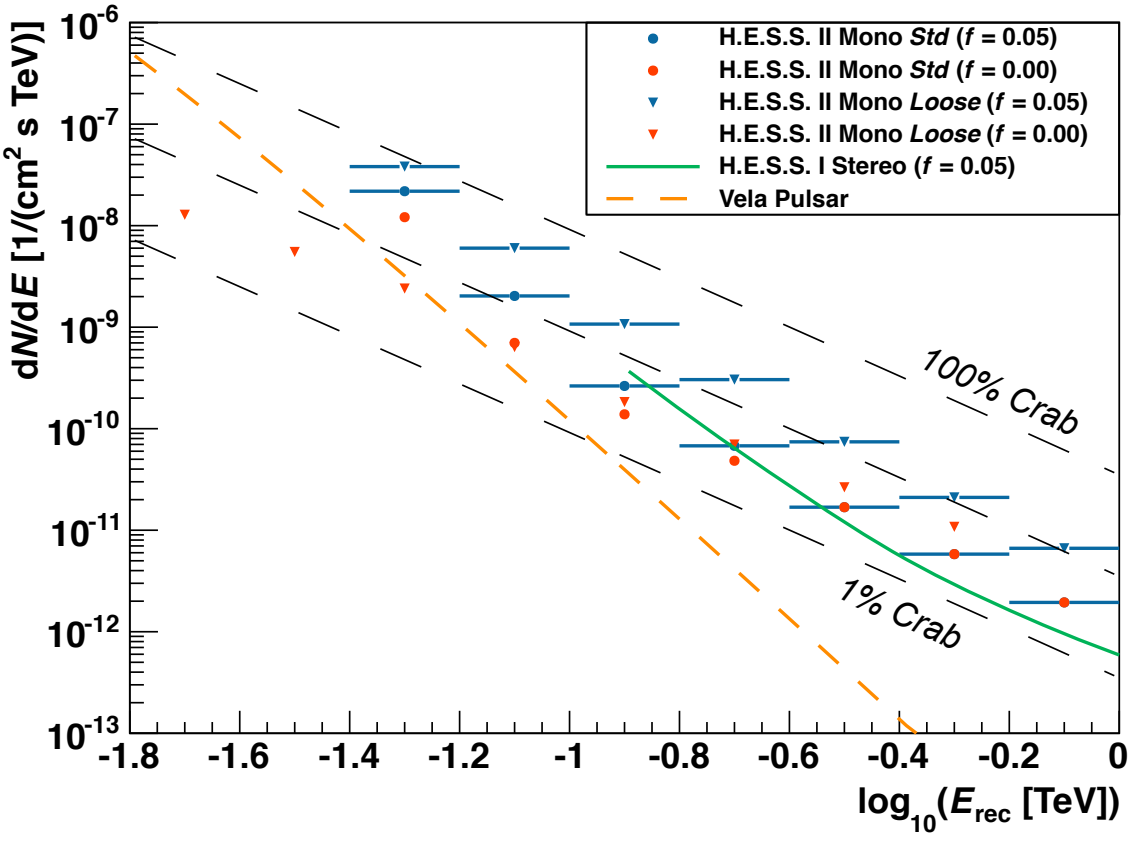

Fig. 4.14: Differential sensitivity of H. E. S. S. I and H. E. S. S. II when observing at low zenith angles. The assumptions are an observation time of 100 hours, a detection significance of 5σ, and a minimum of 10 excess counts for each bin. The curve for H. E. S. S. I is from Funk et al. (2013) and was created using four bins per decade, whereas the results from this work were rebinned to five bins per decade, providing a slightly more conservative estimate. Fractions of the Crab Nebula flux (taken from Aharonian et al. (2006a)) are shown as black dashed lines for comparison (the middle line corresponds to 10% of the Crab Nebula flux). A fit to the Fermi-LAT spectrum of the Vela pulsar is indicated in dashed orange (Tavernier (private communication)). In contrast to the sensitivities, the spectra of the Vela pulsar and the Crab Nebula are both given as a function of true energy.

H. E. S. S. II. Both detectors are, therefore, somewhat complementary at energies $\sim 50\,\mathrm{GeV}$. This is illustrated in Fig. 4.15, which shows the differential sensitivity of H. E. S. S. II and Fermi-LAT as a function of time, separately for energies $\sim 20\,\mathrm{GeV}$, $\sim 50\,\mathrm{GeV}$, and $\sim 80\,\mathrm{GeV}$. Due to its large effective area, H. E. S. S. II is able to detect sources on much shorter time scales than Fermi-LAT, making it especially well-suited to observe transient phenomena such as Gamma-Ray Bursts (GRBs). Fig. 4.15 exhibits one more interesting feature which is worth mentioning. Due to the systematic uncertainty in the background determination, $\mathrm{d}N/\mathrm{d}E$ stays constant in time after $\sim 10^3 - 10^5\,\mathrm{s}$, depending on the energy. This implies that it is not possible to detect a source at low energies just by increasing the observation time.

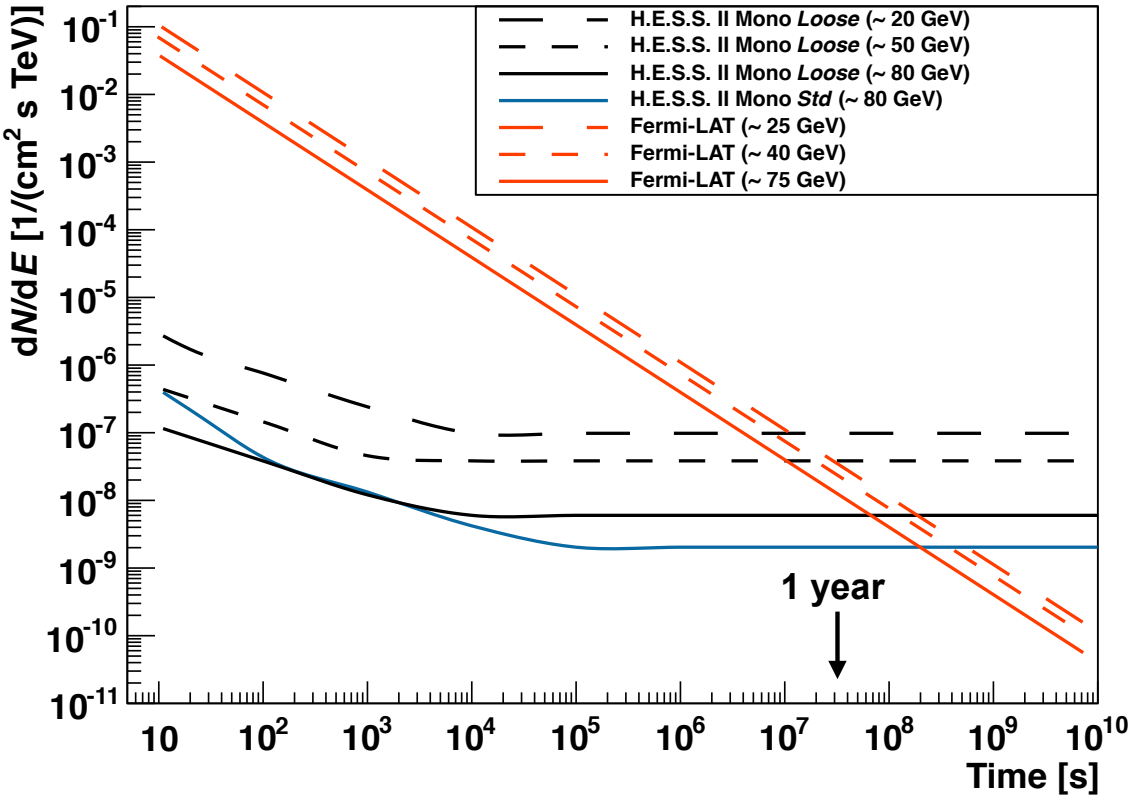

Fig. 4.15: Differential sensitivity as a function of time for energies $\sim 20\,\mathrm{GeV}$, $\sim 50\,\mathrm{GeV}$, and $\sim 80\,\mathrm{GeV}$. The energy values in the legend refer to the mean of the respective bin which was used to calculate the sensitivity (and thus differ slightly between H.E.S.S. II and Fermi-LAT due to the different binning.). A minimum of 25 photon counts was required for both H. E. S. S. II and Fermi-LAT. The values of the latter were taken from Funk et al. (2013). The plot was inspired by Fig. 5 of the same reference.

5 The Crab Nebula and the Galactic Centre Region

After an extensive evaluation of its performance, the single-telescope model analysis will now be applied to real data of two sky regions observed with the H. E. S. S. II telescope. Whereas one source (the Crab Nebula) is point-like and can only be observed at large zenith angles, the other (the Galactic Centre) is surrounded by diffuse emission and was observed at various zenith angles. They are, therefore, complementary and ideally suited as testbeds for the analysis.

5.1 Analysis of the Crab Nebula

In the following, an analysis of the Crab Nebula is presented. Being a strong point-like source that has already been observed with many different instruments, this so-called standard candle of γ-ray astronomy is perfect for a first test of the single-telescope model analysis.

5.1.1 The Crab Nebula - a Unique Astrophysical Laboratory

The Crab Nebula is the remnant of a core-collapse supernova that was recorded by European and Eastern astronomers in the constellation of Taurus in 1054 AD (Duyvendak 1942; Mayall & Oort 1942). With an apparent visual magnitude of up to $m_\mathrm{v} \approx -6$, the explosion was visible to the naked eye during daytime for around three weeks, and during nighttime for nearly two years (Collins et al. 1999). The remnant was discovered in the 18th century and was the first astrophysical object to be included in Charles Messier's catalogue (and is, therefore, also called M1). By now, it is one of the best-studied astrophysical objects. The remnant is located at a distance of $\approx 2\,\mathrm{kpc}$ (Trimble 1968) and consists of four different components (following Hester (2008); for an extensive treatment of the single components, the reader is referred to that reference):

- A central pulsar (called the Crab Pulsar) which is the actual remnant of the progenitor star. It has a rotation period of $P = 33\,\mathrm{ms}$ (Cocke et al. 1969) and a comparatively large spin-down power of $\dot{E} \approx 5 \times 10^{38}\,\frac{\mathrm{erg}}{\mathrm{s}}$.
- A pulsar wind nebula (PWN) that consists of a highly relativistic electron-positron plasma which emits photons over a wide energy range (from radio wavelengths up to TeV energies) via synchrotron and Inverse Compton (IC) radiation.
- Thermal ejecta from the explosion, confining the PWN and visible due to emission lines from several elements and excitation states (see e.g. Graham et al. 1990; Blair et al. 1992).
- Freely expanding ejecta which is almost invisible due to lack of emission.

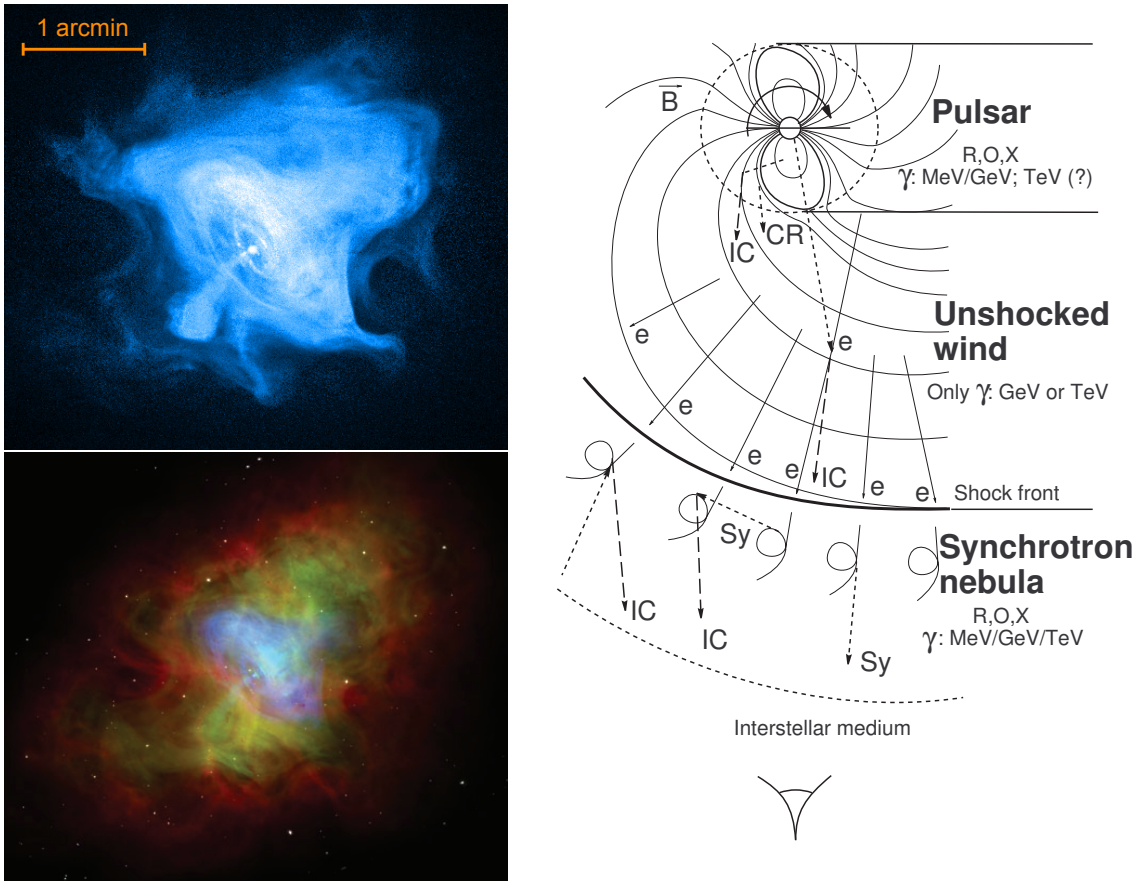

Fig. 5.1: *Left, upper panel:* central part of the Crab's PWN as seen with the *Chandra* X-ray observatory (taken from Seward et al. (2006)). *Left, lower panel:* composite multiwavelength image of the whole synchrotron PWN (Hester 2008). Blue corresponds to X-rays measured with *Chandra* (just like in the upper panel), green to optical emission recorded with the *Hubble Space Telescope*, and red to radio emission measured with the Very Large Array. *Right:* sketch illustrating the different emission regions in a PWN complex, taken from Aharonian & Bogovalov (2003).

The upper left panel of Fig. 5.1 contains an image of the central part of the Crab Nebula as seen with *Chandra* in X-rays (published by Seward et al. (2006)), with the Crab Pulsar clearly visible in the centre as a bright point. The image reveals detailed structures in the nebula due to the $\sim$ arcsecond resolution of the telescope. An extensive treatment of all of them is, however, beyond the scope of this thesis and is also not necessary to comprehend the basic mechanisms of the PWN, which will be outlined in the following. The current understanding is that a large part of the pulsar's spin-down luminosity is released as a relativistic particle wind, mainly consisting of electrons and positrons and including a toroidally shaped magnetic field (Rees & Gunn (1974); see also sketch in the right part of Fig. 5.1). In the inner part of the system, the pulsar wind expands almost freely. The ram pressure of the wind and the pressure of the PWN are in balance at a certain distance from the pulsar, marking the end of the free outflow (Gaensler & Slane 2006). At this termination region, the plasma is shocked (in the *Chandra* image in Fig. 5.1, the termination shock is supposed to be near the torus which is close to the pulsar). As suggested by Fermi (1949), charged particles can be accelerated in such shock fronts due to

consecutive magnetic scattering. The resulting energy distribution of the shocked particles follows a power law,

$$\frac{\mathrm{d}N}{\mathrm{d}E} \propto E^{-p} \ , \tag{5.1}$$

and the spectral index p has a value of ≈ 2 (newer references such as Spitkovsky (2008) show that the actual spectral shape might be more complex, but Eq. 5.1 is still regarded as a valid simplification).

The region downstream of the termination shock is the actual PWN. Here the plasma moves outwards at a much lower velocity compared to the unshocked flow of the upstream region. Near the shock, the plasma speed is $\approx c/3$ (Kennel & Coroniti 1984), and the flow decelerates further out since the PWN is confined by the external ejecta. During the outward propagation, the leptons in the plasma lose energy due to adiabatic cooling and photon emission. When traversing the magnetic field, which has an average strength of a few tens or hundreds of μG (Marsden et al. 1984), the leptons are deflected and emit synchrotron radiation over a broad energy range (Blumenthal & Gould 1970); from radio wavelengths up to γ-rays with GeV energies (Loparco & Fermi LAT Collaboration 2011). Due to the cooling of the leptons, the size of the synchrotron nebula is smaller for higher energies, as can be seen in the lower left panel of Fig. 5.1.

In addition to synchrotron radiation, the other non-thermal photon emission process in the Crab Nebula is Inverse Compton (IC) emission. As depicted in Blumenthal & Gould (1970), an energetic electron/positron can transfer a great fraction of its energy to a photon by electromagnetic scattering. This effect allows for maximum photon energies of several tens of TeV in a PWN scenario. The process is closely related to normal Compton scattering by a Lorentz transformation. In the case of the Crab Nebula, most of the seed photons for the IC scattering are provided by the synchrotron emission (see e.g. Zhang et al. 2008).

Statistically significant VHE emission from the Crab Nebula was first detected with the Whipple telescope (Weekes et al. 1989), an experiment that pioneered the IACT technique. Being the brightest steady source of TeV γ-rays, the Crab has since become the standard candle of VHE γ-ray astronomy. It was observed by all major IACTs, such as e.g. HEGRA (Aharonian et al. 2000b), H.E.S.S. I (Aharonian et al. 2006a), MAGIC I and MAGIC II (Albert et al. 2008b; Aleksić et al. 2012), and VERITAS (Celik 2008).

Despite being studied in the γ-ray energy range for several decades, the Crab still holds surprises and remains an object of active research. In 2008, the MAGIC collaboration discovered pulsed γ-rays with energies above 25 GeV from the Crab Pulsar. As shown by VERITAS, the energy spectrum of the pulsed emission extends up to at least 400 GeV (Aliu et al. 2011). In addition to that, MAGIC recently discovered bridge emission (i.e. emission between the pulse peaks) above 50 GeV from the Crab Pulsar (Aleksić et al. 2014). All these results challenge the current theoretical models of γ-ray emission from pulsars and, therefore, lead to a better understanding of these objects. Another breakthrough discovery was the detection of flares in the Crab Nebula with Fermi-LAT and AGILE at energies above 100 MeV (Abdo et al. 2011; Tavani et al. 2011; Mayer et al. 2013). During the flares, the flux of the nebula increased by more than a factor of 20 on time scales of only a few hours implying that the emission region is small compared to the size of the whole nebula. During the March 2013 flare, the Crab Nebula was observed by both VERITAS and H. E. S. S. in order to search for a VHE counterpart to such flares, but no significant flux enhancement was detected by either of the instruments (Aliu et al. 2014; H.E.S.S. Collaboration et al. 2014). Another interesting research topic is the still

unknown extent of the Crab Nebula in VHE γ-rays. Modern techniques, such as the model analysis, enable angular resolutions down to several arcminutes for H. E. S. S. I (de Naurois & Rolland 2009). Up to now, no IACT has been able to measure the size of the emission region. Upper limits on the extent were published by HEGRA (Aharonian et al. 2000a) and MAGIC I (Albert et al. 2008b) and constrain the IC emission to be contained within the synchrotron nebula. In contrast, the IC nebula of many other PWNe is more extended than the synchrotron nebula, for e.g. HESS J1825-137 (Aharonian et al. 2006e), HESS J1303-631 (H.E.S.S. Collaboration et al. 2012), and HESS J1837-069 (Aharonian et al. 2006c). A more detailed statement about the extent of the VHE Crab Nebula would thus lead to a better understanding of the γ-ray emission regions of these objects.

Due to its declination of $\delta = +22.01°$, the Crab Nebula can only be observed with H. E. S. S. at zenith angles of more than 45°, leading to an energy threshold of $\approx$ 400 GeV for H. E. S. S. I (Aharonian et al. 2006a). Both MAGIC and VERITAS are located in the northern hemisphere and are able to study the source at lower zenith angles, thus allowing a reduced energy threshold. MAGIC, for example, measured the spectrum of the Crab Nebula down to energies well below 100 GeV (Albert et al. 2008a; Aleksić et al. 2012). With the analysis presented in this thesis, H. E. S. S. II is also expected to reach down to $\approx$ 100 GeV even at that large zenith angles. The Crab Nebula is, therefore, perfectly suited to test the analysis at large zenith angles. Below 400 GeV, the results can be cross-checked with those of MAGIC and VERITAS obtained at low zenith angles, and at larger energies also with H. E. S. S. I.

5.1.2 Data Set

The Crab Nebula is observable with H. E. S. S. from August/September to March/April (depending on the maximum accepted zenith angle). It was a prime target during the H. E. S. S. II commissioning phase, which lasted from July 2012 to March 2013, and was again observed starting in September 2013. As the settings of the camera of the H. E. S. S. II telescope were frequently changed during the commissioning phase, all of the runs taken at that time were not used for the analysis presented here.

Each of the runs was calibrated with the French calibration software of the H. E. S. S. collaboration. The calibration includes the determination of the pedestal, gain of the high-gain channel, high-gain/low-gain ratio, and the flat-field coefficient of each camera pixel. It also checks if the pixel is broken. This calibration mechanism is extensively described in Aharonian et al. (2004b) for the cameras of the H. E. S. S. I telescopes and is quite similar for the H. E. S. S. II telescope. Once a run is calibrated, the pixel intensity is given in units of pe, and the run is ready for the model reconstruction (see Chapter 3). As an example, Fig. 5.2 shows the distribution of broken pixels (*left panel*) and mean pedestal values (*right panel*) for the first run that was used for the analysis. The small amount of broken pixels as well as the smooth distribution of mean pedestal values (except for the broken pixels) indicate that the calibration of this run was successful.

In order to ensure a high quality standard of the subsequent analysis, only runs that fulfil all of the following requirements are kept for the analysis (they refer to the H. E. S. S. II telescope only, even if other telescopes participated in the run):

- the amount of broken pixels is less than 15%;
- the run lasted for at least 5 minutes;

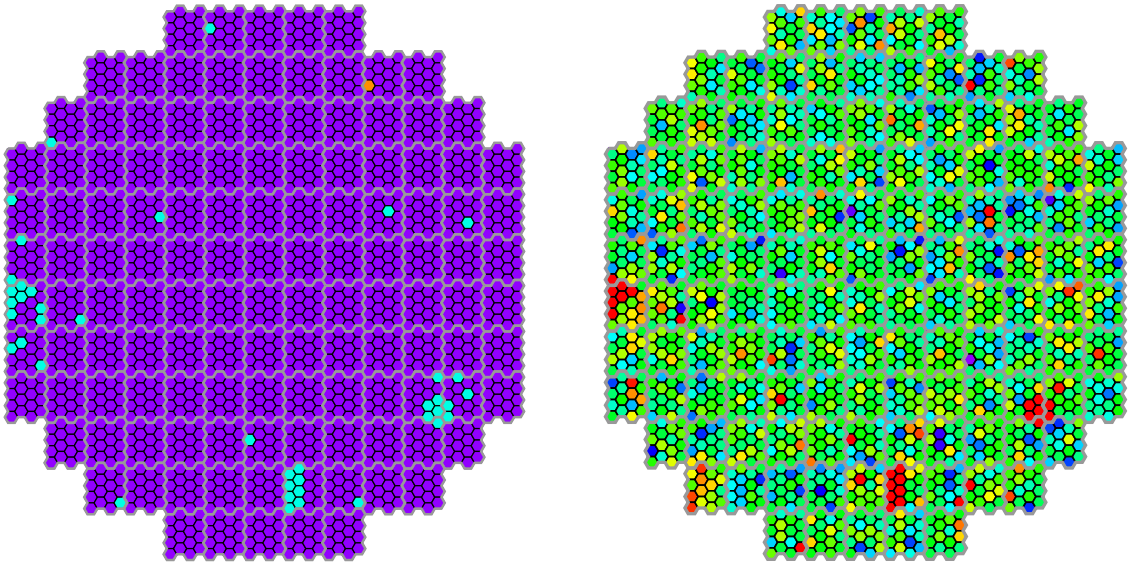

Fig. 5.2: *Left panel:* distribution of broken pixels of the high-gain channel in the H. E. S. S. II camera for the first run of the analysis. Purple means that the respective pixel is not broken and therefore usable. The pixel on the upper right that is marked orange is not used because of a bad high-gain/low-gain ratio, and the ones in light blue are excluded due to unspecified calibration problems. *Right panel:* distribution of mean pedestal values of the high-gain channel for the same run in the ADC range of $[-12600, -11000]$.

- the mean trigger rate is above 1200 Hz;
- the dispersion of the trigger rate is below 10%.

These criteria are inspired by the ones described in Aharonian et al. (2006a) for H. E. S. S. I. The lower limit on the mean trigger rate was chosen after checking the rate of some runs of the whole data set. The mean rate of most runs is around 1500 Hz, and thus the required minimum corresponds to 80% of that value. In addition to the aforementioned selection cuts, all runs with a pointing offset of more than 1.0° as well as the ones with a zenith angle above 55° were excluded from the analysis.

After the run selection, the data set used for the analysis consists of 41 observation runs with a total live time of 16.2 hours. The runs were taken between 15th September 2013 and 4th January 2014. The zenith angles of the observations range between 45° and 55°. All runs were conducted in wobble mode (Fomin et al. 1994) with different pointing offsets between 0.5° and 1.0° in both positive and negative right ascension as well as declination. Pointing corrections were applied in order to take into account distortions of the telescope structure which lead to shifting and/or rotation of the camera (details about the pointing corrections are given in Gillesen (2004)).

5.1.3 Results

The selected data were analysed with the *Standard* and *Loose* configuration for the γ-hadron separation presented in Sec. 4.1. $\vartheta^2_{\mathrm{max}}$ was set to $0.03\,\mathrm{deg}^2$ for the *Standard* cuts and to $0.06\,\mathrm{deg}^2$ for the *Loose* cuts, respectively. The target region was centred on the

position of the Crab Pulsar, which was determined with high-precision radio measurements by Lobanov et al. (2011). For the subsequent studies, the background was estimated using the *reflected-region* method which is presented in Berge et al. (2007). For the definition of the OFF (i.e. background) regions, a circle with a radius of 0.4° around the source was excluded to avoid protrusion of events from the source into the background regions. As for the *Standard* cut configuration, the number of possible OFF regions with this configuration is $n_{\mathrm{OFF,max}} = 6$ for a wobble offset of 0.5°, and $n_{\mathrm{OFF,max}} = 15$ for an offset of 1.0°. For the *Loose*-cut analysis, n_{OFF} was fixed to 1, and for each run the ON region was mirrored at the camera centre to obtain the OFF region. This approach ensures a maximum angular separation of target and background region and thus leads to a better spatial background estimation for this configuration with decreased angular resolution.

The number of excess events in the ON (i.e. source) region is given by (Li & Ma 1983)

$$N_{\mathrm{Exc}} = N_{\mathrm{ON}} - \alpha N_{\mathrm{OFF}} \ , \tag{5.2}$$

where $N_{\mathrm{ON/OFF}}$ is the total number of γ-like events in the ON and OFF regions, respectively. The scaling factor α generally corrects for differences of solid angle, observation time, and acceptance of the signal and background regions. Using the *reflected-region* background method, α is simply $1/n_{\mathrm{OFF}}$ for each observation run (Berge et al. 2007). Averaging over all runs used for the analysis presented here, it amounts to $\alpha = 1/8.52$ for the *Standard*-cut analysis, and simply $\alpha = 1$ for the *Loose*-cut analysis. The development of N_{Exc} with respect to the number of rescaled OFF events for both configurations is shown on a run-by-run basis in the *upper* and *lower left panels* of Fig. 5.3. For a steady source and a good data set, the distribution is expected to rise linearly. For the analysis using the *Standard* cuts, the data are clearly linear and only scatter sparsely around the best-fit line. In contrast, the distribution for the *Loose*-cut analysis exhibits a much stronger scattering, which is mostly due to the lower signal-to-background ratio.

The significance of a source is calculated with Eq. (17) from Li & Ma (1983):

$$S_{\mathrm{LiMa}} = \sqrt{2}\left\{ N_{\mathrm{ON}} \cdot \ln\left[\frac{1+\alpha}{\alpha}\left(\frac{N_{\mathrm{ON}}}{N_{\mathrm{ON}}+N_{\mathrm{OFF}}}\right)\right] + N_{\mathrm{OFF}} \cdot \ln\left[(1+\alpha)\left(\frac{N_{\mathrm{ON}}}{N_{\mathrm{ON}}+N_{\mathrm{OFF}}}\right)\right]\right\}^{1/2} \tag{5.3}$$

The index "LiMa" will be omitted in the following, but all significances in this chapter are calculated with this formula (as opposed to Eq. 4.22). The rise of the significance as a function of rescaled OFF events is illustrated in the *upper* and *lower right panels* of Fig. 5.3 for *Standard* and *Loose* cuts, respectively. A square root function fitted to the results describes the data very well.

The ϑ^2 histogram for the *Standard*-cut analysis is shown in the *upper left panel* of Fig. 5.4. The distribution of events from the OFF regions appears to be flat, whereas the one from the ON region clearly peaks at zero. Both distributions are well compatible with each other at $\vartheta^2 \gtrsim 0.1\,\mathrm{deg}^2$, confirming that the calculation of the background distribution is correct for this point-like source. As for the ϑ^2 histogram which is obtained when applying *Loose* cuts (*lower left panel* of Fig. 5.4), the background is much more prominent, and it declines with increasing angular distance. Due to the worse angular resolution, compared to the *Standard* analysis, the excess is less peaked and more dispersed. Strikingly, the ON and OFF distributions merge at large ϑ^2 values, indicating that the background estimation also works for this low-energy cut set.

The event statistics for both analyses are shown in the respective ϑ^2 histograms. Regarding the *Standard* analysis, the signal-to-background ratio amounts to $N_{\mathrm{Exc}}/(\alpha N_{\mathrm{OFF}}) = 3.9$,

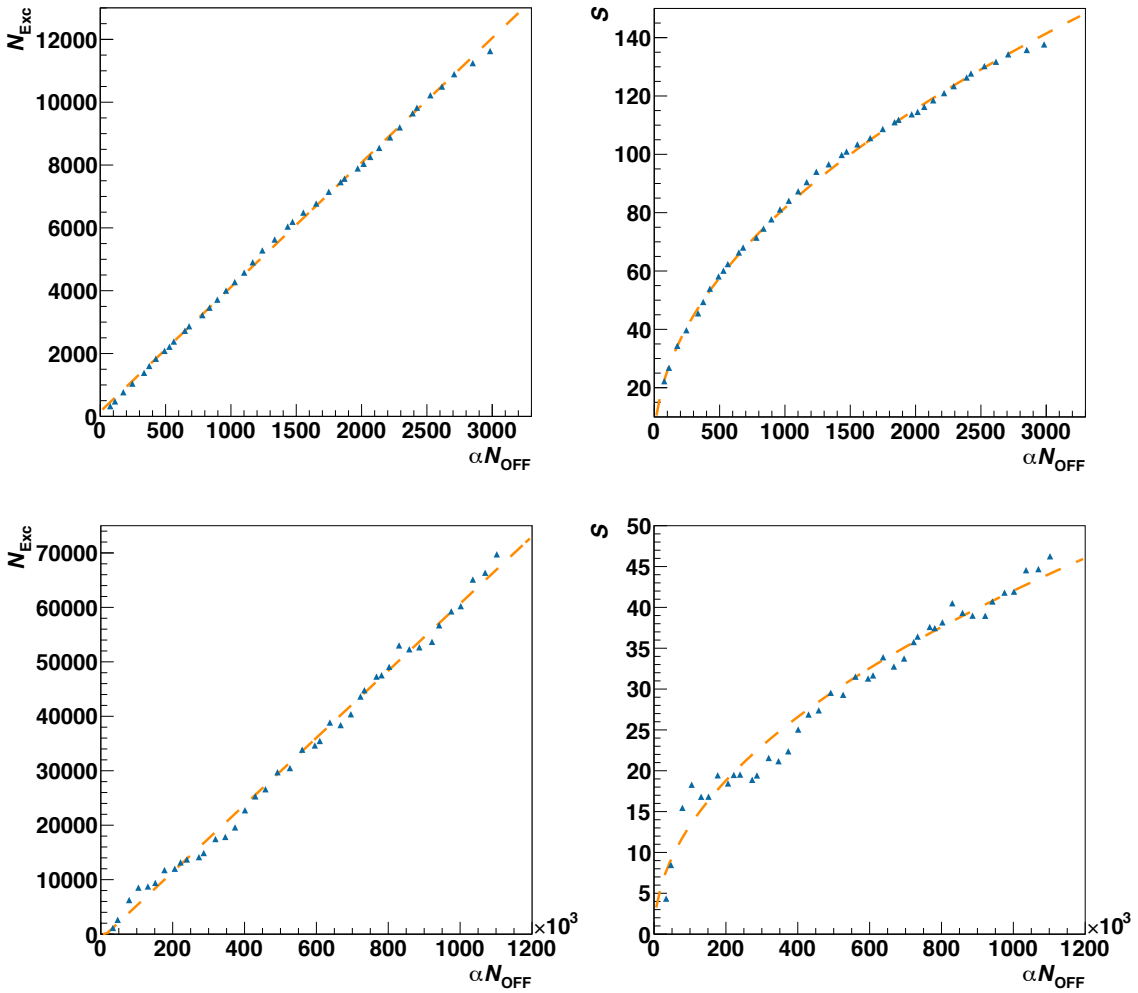

Fig. 5.3: *Upper panel:* development of N_{Exc} (*left*) and S (*right*) with respect to the amount of rescaled OFF events for the *Standard*-cut analysis, obtained on a run-by-run basis. In both histograms, the measured values are shown in blue, and the dashed orange line corresponds to a fit to the data. *Lower panel:* the same as in the *upper panel*, but for the *Loose*-cut analysis.

which is very large for a single-telescope analysis of this source. For instance, Albert et al. (2008a) only obtained $N_{\mathrm{Exc}}/(\alpha N_{\mathrm{OFF}}) = 0.18$ ($E > 110\,\mathrm{GeV}$) and $N_{\mathrm{Exc}}/(\alpha N_{\mathrm{OFF}}) = 1.30$ ($E > 200\,\mathrm{GeV}$). Although the analysis shown here was carried out with *Standard* cuts which are not optimised for a low energy threshold or a maximum effective area, the measured excess rate of $11.9\,\gamma/\mathrm{min}$ is quite large. For comparison, Aharonian et al. (2006a) only obtained $6.0\,\gamma/\mathrm{min}$ by applying a Hillas analysis with *Standard* cuts to the H. E. S. S. I data. Most of this difference is due to the lower energy threshold of H. E. S. S. II. However, the value is still slightly larger compared to the excess rate obtained with MAGIC I at an even lower threshold (Albert et al. 2008a, $\approx 11\,\gamma/\mathrm{min}$ with energies $> 75\,\mathrm{GeV}$). As for the *Loose*-cut results shown in this work, the excess rate reaches a range that has never been obtained before for a steady source in γ-ray astronomy. With around 1.2 γ-rays being detected every second, the rate is half as high as the one measured with H. E. S. S. I in 2006 during the exceptionally bright flare of PKS 2155-304 (Aharonian et al. 2007).

The source significance as a function of the applied $\vartheta^2_{\mathrm{max}}$ cut is shown in Fig. 5.4 on the

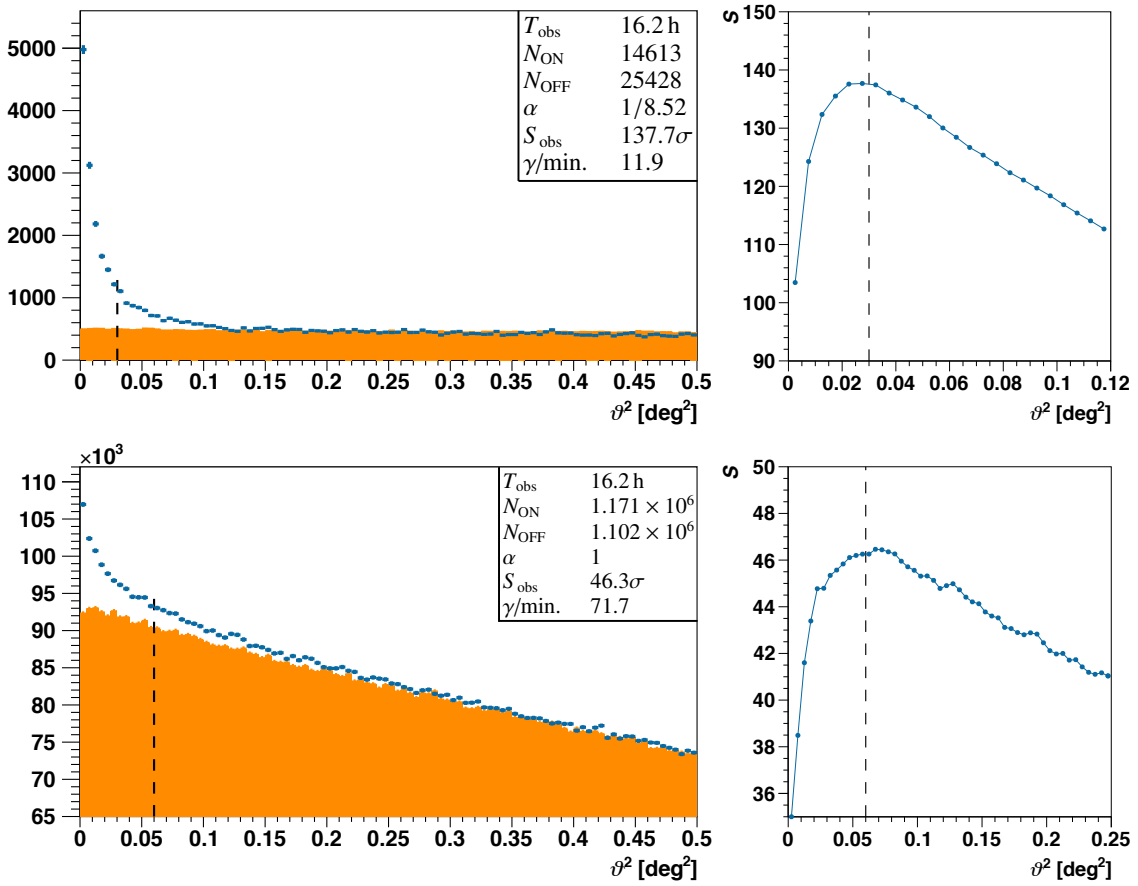

Fig. 5.4: *Left:* ϑ^2 histograms of γ-like events from the Crab Nebula for *Standard* (*top*) and *Loose* cuts (*bottom*), respectively. The distribution around the source position is shown in blue, and the one from the OFF regions, scaled with α, in orange. *Right, top and bottom:* significance as a function of the applied ϑ^2_{max} cut for both configurations. The value that was used for the analysis is illustrated with a dashed black line in all plots.

right. Both for the *Standard* (*top*) and the *Loose* configuration (*bottom*), the value that was chosen for the respective analysis (shown as a dashed black line) is situated at the maximum and is thus well suited to detect point sources.

With the obtained significance of $S_{obs} = 137.7\sigma$ (for the *Standard* cuts), the integral sensitivity of the analysis in the given zenith angle range ($45° - 55°$) was calculated. For a detection significance of $S_{min} = 5\sigma$ and an observation time of 50 h, the minimum detectable flux of a source is

$$\frac{S_{min}}{\sqrt{50\,\mathrm{h}/T_{obs}} \cdot S_{obs}} = 0.021 \tag{5.4}$$

in units of the Crab flux. Calculating the other way round, the Crab Nebula is significantly detectable after less than 80 s of observation. The significance accumulation per observation time $S_{obs}/\sqrt{T_{obs}[\mathrm{h}]} = 34.2\sigma$ is distinctly larger than the one obtained with H. E. S. S. I using a standard Hillas analysis (27.0σ, as published in Aharonian et al. (2006a)).

To check how the ϑ^2 distribution of the Crab Nebula compares to simulations, simulated γ-rays from a point source with a power-law spectrum with index 2.4 (nearly equalling

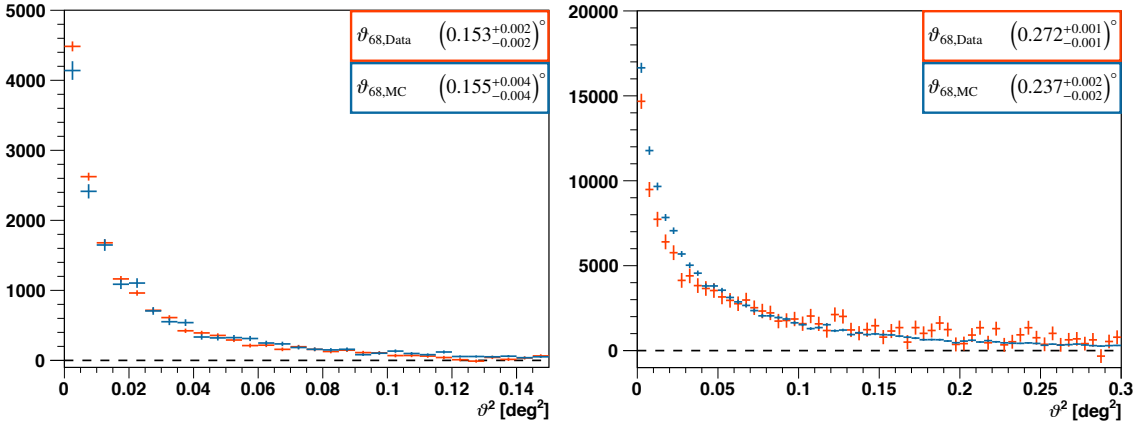

Fig. 5.5: MC-data comparison of ϑ^2 distributions around the source position for *Standard* (*left*) and *Loose* (*right*) cuts. The blue crosses correspond to simulated γ-rays from a point source with spectral index 2.4 at 50° zenith angle whereas the distribution of the measured excess is plotted in red. Shown in the upper right are the ϑ_{68} values for both simulations and data which were calculated as described in Section 4.2.

the one measured by Aharonian et al. (2006a)) were analysed. The zenith angle of the simulations was set to 50°, right in the middle of the range in which the observation runs were taken. The resulting ϑ^2 histogram of the analysis with *Standard* cuts is shown in Fig. 5.5 (*left panel*), together with the measured excess from Fig. 5.4. The simulated distribution was scaled by a factor of 4.28 such that its integral in the displayed range is identical to the one of the excess. As can be seen, the measured and simulated distributions match very well. For both of them, the 68% containment radius ϑ_{68} was calculated as described in Section 4.2, using the displayed histogram range for the fit. The resulting values agree up to the third decimal place, so the angular resolution obtained from MC simulations appears to be correct. The same MC-data comparison was carried out using *Loose* cuts (see the *right panel* of Fig. 5.5). Although the ϑ_{68} values of simulation and data do not match as well as for the *Standard* cuts, the overall agreement of the spatial event distribution is very good, notably also at larger offset from the source position.

In contrast to source-dependent analysis techniques (as, e.g., used for the first VHE γ-ray detection of the Crab Nebula with Whipple (Weekes et al. 1989)), the reconstruction method used in this thesis estimates the source direction of each event. This approach allows analysis results to be visualised with sky maps, which is particularly helpful when analysing the morphology of extended sources or measuring source positions. Only the results from the *Standard* cuts will be used in the following.

For producing sky maps, it is first necessary to compute the acceptance in the FoV of the camera. FoV acceptance maps are calculated for each run. In each of these run-wise maps, the exclusion regions are ignored (which is only the Crab Nebula in this case). Finally the maps are superimposed to get one overall map. The FoV acceptance map for the analysis of the Crab Nebula is shown in Fig. 5.6 (*upper left panel*). Due to the different wobble offsets, the target exclusion region does not affect the appearance of the superimposed map, which is quite smooth and does not exhibit any obvious features. Remarkably, the map extends well beyond the optical FoV of the camera. The analysis is thus able to detect sources that are outside the FoV.

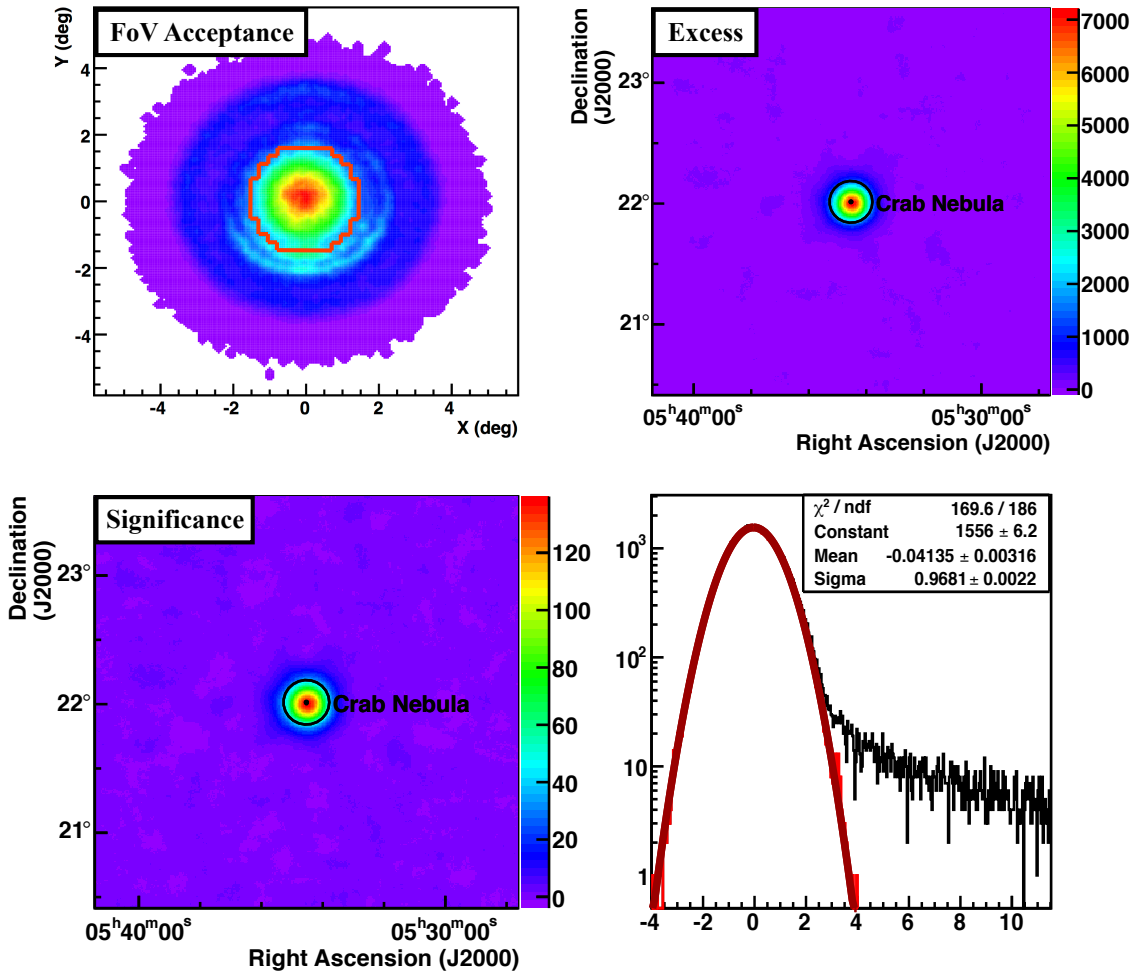

Fig. 5.6: *Upper left:* accumulated FoV acceptance map for γ-like events, oversampled with a radius of 0.1°. The actual FoV of the camera is indicated in red. *Upper right:* excess map around the source position. The black circle denotes the region that is defined by the $\vartheta^2_{\max}$ cut. It is centred on the position of the Crab Pulsar. *Lower left:* significance map, calculated using the *ring background* method (Berge et al. 2007). *Lower right:* distribution of values of the significance map (zoomed in for better visibility). The distribution for the whole map is shown in black, whereas the target region was excluded for the red histogram entries. The background distribution was fitted with a Gaussian function (solid red line), and the fit statistics are also given.

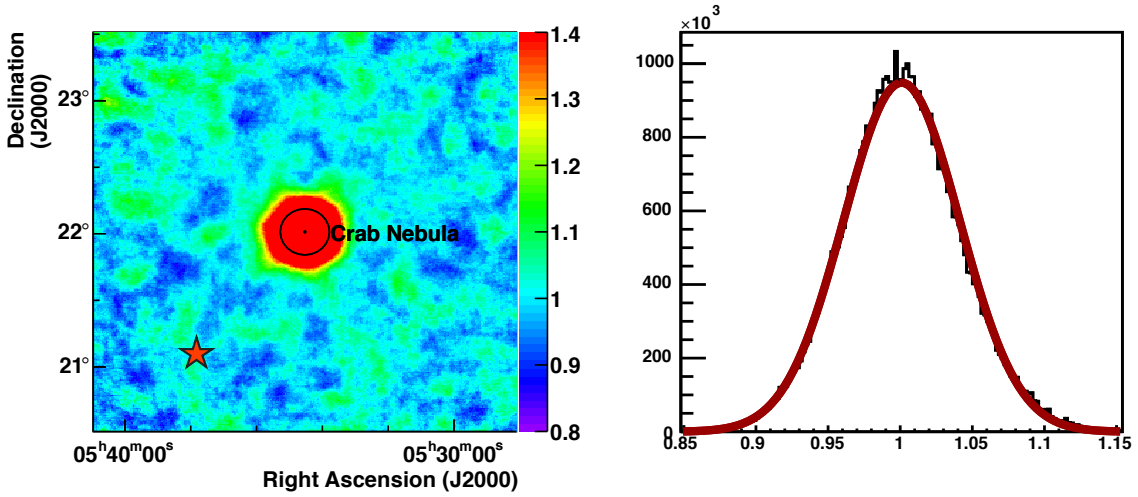

Fig. 5.7: Oversampled map of γ-ray candidates (*left*), normalised with the acceptance map. The position of the 3 mag star ζ Tauri is indicated with a red star. The distribution of entries of the map is shown on the *right* in black and was fitted with a Gaussian (red).

For the calculation of the excess map, the *ring background* method (Berge et al. 2007) was used. It is shown in Fig. 5.6 (*upper right*). The map is oversampled with a sampling radius of 0.1° and has a bin size of 0.01° in both right ascension and declination, respectively. Outside the source region, the map is flat and the values are close to zero. As expected from simulations (Section 4.2), the shape of the signal appears radially symmetric. Fitting the central part of the map with a two-dimensional Gaussian, the peak of the emission is located at right ascension $\alpha = 5\,\mathrm{h}\,34\,\mathrm{m}\,29.71\,\mathrm{s} \pm 0.02\,\mathrm{s}$ and declination $\delta = 22°\,00\,\mathrm{m}\,24.12\,\mathrm{s} \pm 0.25\,\mathrm{s}$ (the errors are solely statistical). This corresponds to an offset of ≈ 40 arcsec from the pulsar position (taken from Lobanov et al. (2011)). The offset can at least partly be accounted for by the systematic error of the pointing precision.

A significance map with the same binning as for the excess map is shown in the *lower left panel* of Fig. 5.6. The distribution of its values is shown in the *lower right*, separately for the whole map (black) and for all bins that are not part of the target exclusion region (red). The latter distribution was fitted with a Gaussian (smooth red line) to test if the significances are randomly distributed. As can be seen from the fit statistics, the significance map is well normalized.

As a further check, Fig. 5.7 shows the map of γ-ray candidates (*left panel*), normalised with the acceptance map. Apart from the region around the source, the map is flat, which is even the case around the relatively bright star ζ Tauri. This means that the data-taking (by switching off PMTs) as well as the analysis (by handling these pixels which are then marked as broken) are well capable of dealing with locally enhanced NSB. The distribution of entries of the map is shown in the *right panel* of the figure. The distribution peaks around 1 and can be well approximated with a Gaussian function.

The distributions of G_{NSB} and SG_{SC} values before and after applying *Standard* cuts are shown in Fig. 5.8, separately for the events in the ON region (blue) as well as for those in the OFF regions (red), scaled with α for comparison with the ON distribution. Subtracting the latter from the former leads to the distribution of the excess events which is displayed in green in all panels. As can be seen in the *upper left* panel of Fig. 5.8, most of the events

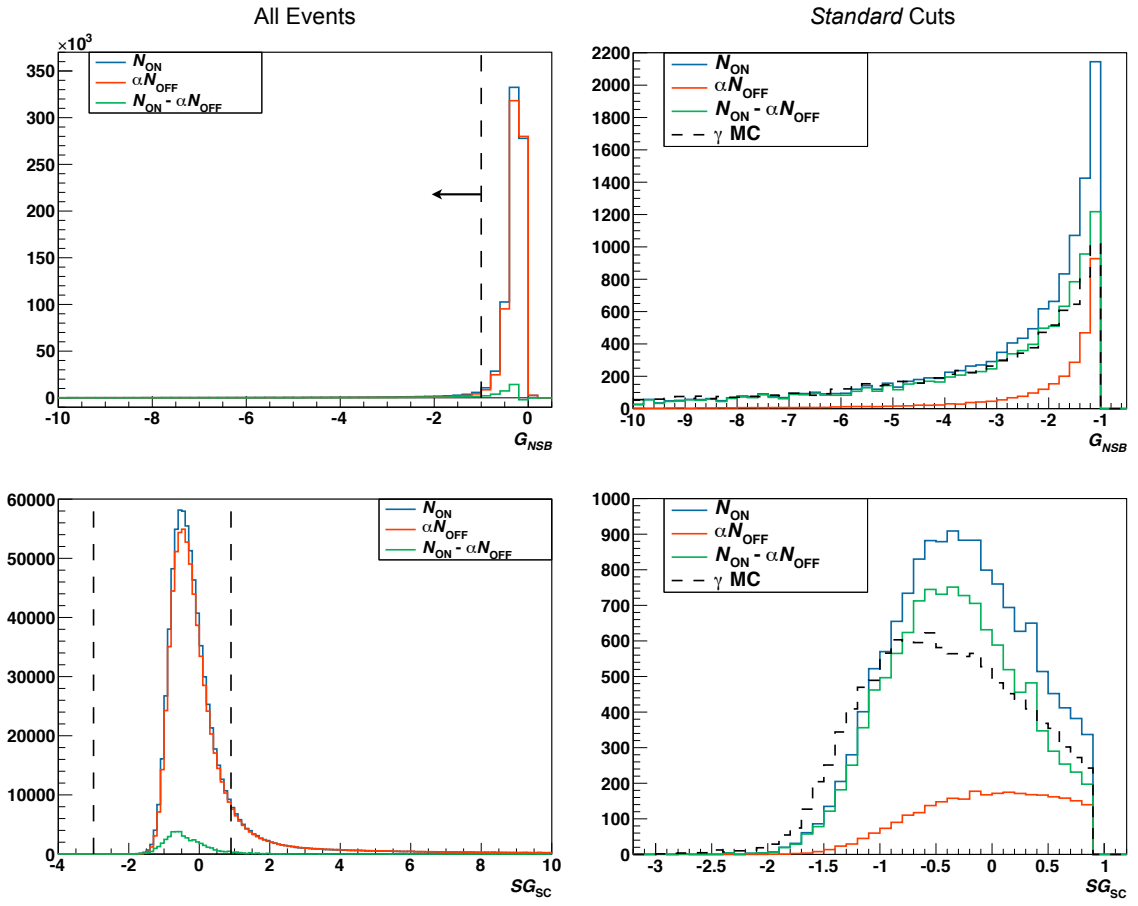

Fig. 5.8: *Top:* distribution of G_{NSB} values before γ-hadron separation (*left*). The acceptance range of this variable (when applying *Standard* cuts) is shown with a black dashed line and an arrow. The distribution of values after applying all *Standard* cuts is shown on the *right*, together with the one that is obtained when using simulated γ-rays (the integral of the latter is normalised to the one of the excess events). *Bottom:* the same as above, but for the SG_{SC} variable. The acceptance range for both the *Standard* and *Loose* configuration is indicated with two dashed black lines in the left plot. The number of OFF events is scaled with α in all plots.

(more than 95% of the ones in the ON region) exhibit G_{NSB} values above -1 and are thus removed when applying *Standard* cuts. This behaviour was already expected from the discussion in Chapter 4.1. Regarding the G_{NSB} distribution after applying *Standard* cuts (*upper right* panel), most of the excess is located near the cut position, but there the signal-to-background ratio is also lower. The distribution of simulated γ-rays (at a zenith angle of 46°) is shown in the same plot, scaled such that the integral is normalised to the one of the excess events.

As for the SG_{SC} distribution before γ-hadron separation (*lower left* panel in Fig. 5.8), it looks considerably different than the one for H. E. S. S. I (see Fig. 19 in de Naurois & Rolland (2009)). Whereas most of the background events can be removed by cutting on this variable in the case of stereoscopic reconstruction, the greater part of the OFF events are located in the γ acceptance region when only using one telescope. After applying the

other *Standard* cuts, the remaining excess dominates over the OFF events at all accepted values of SG_{SC}, where the greatest part of the background is situated on the right (which is similar to H. E. S. S. I and also expected from the definition). Compared to the simulated γ-rays, the peak of the excess event distribution is slightly shifted to the right. This shows that the MC simulations do not perfectly describe the real events, however, the agreement is still quite good.

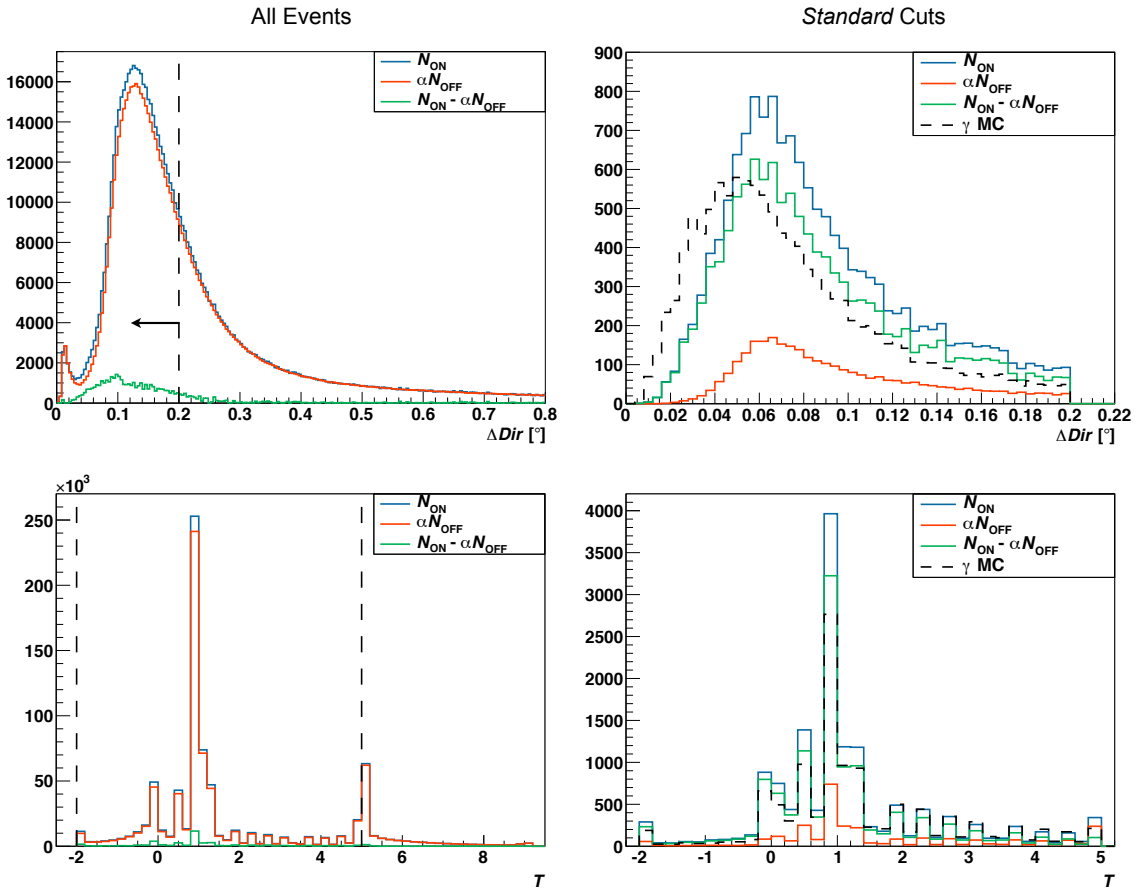

Fig. 5.9: *Top:* distribution of ΔDir values before (*left*) and after (*right*) applying *Standard* cuts, illustrated just as in Fig. 5.8. *Bottom:* the same as above, but for the reconstructed first interaction depth T.

Fig. 5.9 shows the distribution of the direction error ΔDir and the first interaction depth T separately for the data set before separation and after applying *Standard* cuts (analogously to Fig. 5.8). Concerning the ΔDir distribution of the unselected events (*upper left* panel in Fig. 5.9), $\approx 60\%$ are within the *Standard*-cut acceptance range, and this fraction is even larger for the excess events. In addition to a large peak, both the ON and the OFF distributions feature an equally small and thin local maximum at $\Delta Dir \approx 0.02$. It is completely removed by the ON$-$OFF subtraction and also after the *Standard*-cut γ-hadron separation (see *upper left* panel in the figure). Comparing the excess distribution after *Standard* cuts with the simulated one, it can be seen that the estimated uncertainty on the fitted direction is generally slightly lower for the MC γ-rays, which can also be ascribed to the limitations of the MC simulations (as for SG_{SC}).

The reconstructed first interaction depths T of the whole sample are displayed in the *lower left* panel of Fig. 5.9. All of the distributions feature a distinct peak at $T = 1$ and several

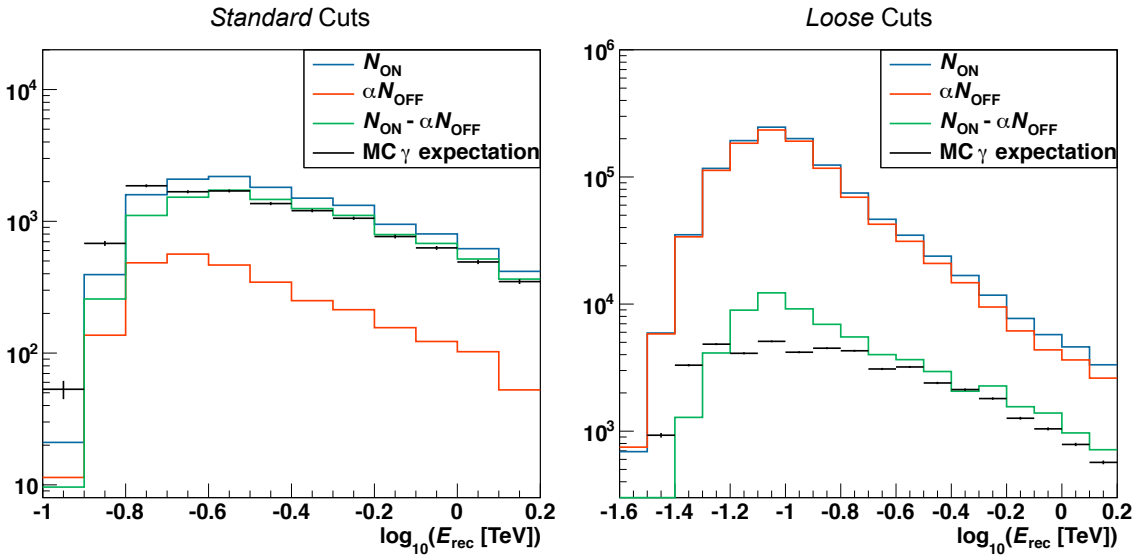

Fig. 5.10: Energy distribution of signal and background events for the Crab Nebula analysis for both *Standard* and *Loose* cuts. The simulated distribution of γ-rays (using events with $\theta = 46°$ and the Crab Nebula spectrum from Aleksić et al. (2012)) is shown in black in both panels.

smaller ones which correspond to the other 11 values of the model templates. As the first interaction depth is the fit parameter that generally has the least influence on the shower image, it seems that the fitted values either tend to stick at the starting parameter ($T = 1$) or favour the template values instead of the interpolated ones. This even remains after applying the *Standard* cuts, and the shape of the distribution of simulated γ-rays is very similar to the one of the excess events.

As a further check, Fig. 5.10 contains the energy distribution of the events for both the *Standard* (*left*) and the *Loose* (*right*) cut configuration. Regarding the *Standard* cuts, the excess dominates over the background except for the first displayed bin. The signal-to-background ratio increases with larger energy, which is expected due to the better γ-hadron separation. The figure also contains the expected distribution of γ-rays, using simulations at 46° zenith angle. The assumed source spectrum is the one published in Aleksić et al. (2012), and it is folded with the instrument response as described in Section 4.4. The agreement with the measured excess is excellent at energies above 200 GeV. At lower energies, the simulated excess exceeds the measured excess, which might be because the fixed zenith angle of the simulations is at the lower end of the range of the observations (46° as compared to $[45°, 55°]$).

As for the *Loose* cuts, the excess is situated distinctly below the OFF events for all energies. Strikingly, signal events are measured as low as $E_{\mathrm{rec}} \approx 40$ GeV with this configuration despite the large zenith angle, emphasising the great low-energy capabilities of the H. E. S. S. II telescope. As is apparent from the simulated distribution, an excess in this domain is indeed expected. Generally the agreement between simulation and measurement is not as good as for the *Standard* cuts, where both deviate by a factor of ≈ 2 at around 100 GeV (in addition to a deviation at the threshold that is similar to the one seen in the *Standard*-cut distribution). However, since the signal-to-background ratio is rather low for this source, the analysis is quite prone to systematic background uncertainties. The *Loose* cuts are actually designed for the analysis of pulsars and strong transient sources

Table 5.1: Fit results of different spectral models applied to the *Standard*-cut analysis of the Crab Nebula. The errors are purely statistical.

Parameter	Standard Power Law	Exponential Cutoff Power Law	Curved Power Law
φ_0 $[10^{-10}/(\mathrm{cm}^2\ \mathrm{s\ TeV})]$	2.00 ± 0.02	3.08 ± 0.03	4.30 ± 0.05
E_0 [TeV]	0.435	0.370	0.324
Γ	2.48 ± 0.01	2.22 ± 0.03	2.26 ± 0.02
E_c [TeV]	/	3.9 ± 0.4	/
b	/	/	0.146 ± 0.014
$\ln L$	-98.5	-37.9	-32.7
χ^2/NDF	197/45	76/44	65/44

where the systematic uncertainties on the background are compensated by the fact that precise OFF data can be found in the quiescent phases of the sources.

After this MC-data comparison which revealed that the single-telescope model analysis for H. E. S. S. II is already quite well understood, the energy spectrum of the Crab Nebula shall be discussed in the following. It is calculated using the forward-folding method described in Piron et al. (2001). In short, this approach consists of a maximum likelihood algorithm that is applied to the measured energy distributions of ON and OFF events by taking into account the detector response and a spectral model. It has to be noted that the lookup tables that are used to obtain the following results correspond to a relative optical efficiency of 100% (the tables for the correct efficiencies ($\approx 85\%$) were not yet generated). All results are, therefore, to be considered preliminary and will change slightly in an upcoming publication.

For the spectral analysis, the energy threshold of each run is set to the value where the effective area reaches 10% of its maximum. The threshold of the analysis presented here is $E_\mathrm{min} \approx 145\,\mathrm{GeV}$ as compared to $E_\mathrm{min} \approx 410\,\mathrm{GeV}$ for H. E. S. S. I (Aharonian et al. 2006a), corresponding to a reduction of about 65%.

Three spectral models are applied to the data set. The first is a standard power-law model, as it was used by, e.g., HEGRA to describe the spectrum of this source (Aharonian et al. 2000b). In the present work, it is defined as

$$F_\mathrm{PL}(E) = \left(\frac{\mathrm{d}N}{\mathrm{d}E\,\mathrm{d}A\,\mathrm{d}t}\right)_\mathrm{PL} = \varphi_0 \left(\frac{E}{E_0}\right)^{-\Gamma} , \tag{5.5}$$

with the reference energy E_0, the flux normalisation φ_0, and the spectral index Γ. The fit results are given in Table 5.1. The second spectral model is an exponential cutoff power law, which yields the best description of the Crab Nebula spectrum for H. E. S. S. I (Aharonian et al. 2006a):

$$F_\mathrm{EPL}(E) = \varphi_0 \left(\frac{E}{E_0}\right)^{-\Gamma} \exp\left(-\frac{E}{E_\mathrm{c}}\right) , \tag{5.6}$$

where E_c is the cutoff energy, and the other parameters are identical to those defined above. As can be seen in Table 5.1, this model provides a much better description of the data than the standard power law. Compared to the reference, the best-fit results of both Γ and E_c from this work exhibit a significant deviation. As the H. E. S. S. II spectrum extends down to lower energies, this is not really surprising. Being able to observe the Crab

Table 5.2: Parameters of the Crab Nebula spectrum as measured with H. E. S. S. I (Aharonian et al. 2006a), MAGIC I (Albert et al. 2008a), MAGIC II (Aleksić et al. 2012), and H. E. S. S. II (this work). The curvatures of the MAGIC I and MAGIC II spectra were converted to match the definition and reference energy of the H. E. S. S. II spectrum.

Parameter	H. E. S. S. I	MAGIC I	MAGIC II	H. E. S. S. II
Γ	2.39 ± 0.03	2.31 ± 0.06	2.32 ± 0.02	2.26 ± 0.02
E_c [TeV]	14.3 ± 2.1	/	/	/
b	/	0.12 ± 0.03	0.06 ± 0.02	0.15 ± 0.01
$\Phi(E > 1\,\mathrm{TeV})$ $[10^{-12}/(\mathrm{cm}^2\ \mathrm{s})]$	22.6 ± 0.8	18.5*	21.4*	16.1 ± 0.5

*: the error could not be calculated as the covariance matrix is missing in the reference.

Nebula at much lower zenith angles, MAGIC I and MAGIC II measured the spectrum to below 70 GeV (Albert et al. 2008b; Aleksić et al. 2012). According to these publications, the energy spectrum over the whole measured range can be best described by a curved power law, which is, therefore, the third model tested in the present work. It is given by

$$F_\mathrm{CPL}(E) = \varphi_0 \left(\frac{E}{E_0}\right)^{-(\Gamma + b \ln(E/E_0))}, \tag{5.7}$$

with the curvature parameter b. The fit results (also given in Table 5.1) state that this spectral shape provides the best description out of the three tested here. This difference, compared to H. E. S. S. I, is due to the lower minimum energy of the H. E. S. S. II spectrum.

The 1σ confidence interval of the best-fitting curved power law is shown in Fig. 5.11, together with approximate spectral points which were calculated after the forward folding. The fit results from H. E. S. S. I and MAGIC II are shown for comparison (without error estimates). The H. E. S. S. II spectrum is located below the other two, which may partly be due to the preliminary lookup tables used here. In addition to that, it has to be pointed out that the confidence interval of the spectrum only includes statistical errors. Notably the H. E. S. S. II spectrum presented here not only provides a lower energy threshold than the one of H. E. S. S. I, but also extends to beyond 30 TeV.

Table 5.2 contains some key parameters of the Crab Nebula spectrum as measured with different instruments. Since the threshold energy of the H. E. S. S. I spectrum is considerably larger than the ones of the other three and, furthermore, the assumed spectral shape is different, a comparison of the spectral index is not deemed necessary. Out of the other three spectra, the one of H. E. S. S. II exhibits the lowest spectral index, but is still consistent with MAGIC I and MAGIC II within the given errors. The lower index is compensated by a larger curvature, which might be partly due to the fact that the spectrum is defined up to higher energies. The table also contains the integrated photon flux above 1 TeV for each measurement, which is a handy value to compare the results of all four instruments. The flux measured with H. E. S. S. II is the lowest of all four. Given that preliminary lookup tables were used to derive the spectrum, this behaviour is expected to a certain level. Nevertheless, the measured value is within the $\approx 30\%$ systematic uncertainty that is usually assumed on flux measurements with IACTs (H.E.S.S. Collaboration et al. 2014).

Up to now, no IACT has been able to detect any variability of the Crab Nebula flux.

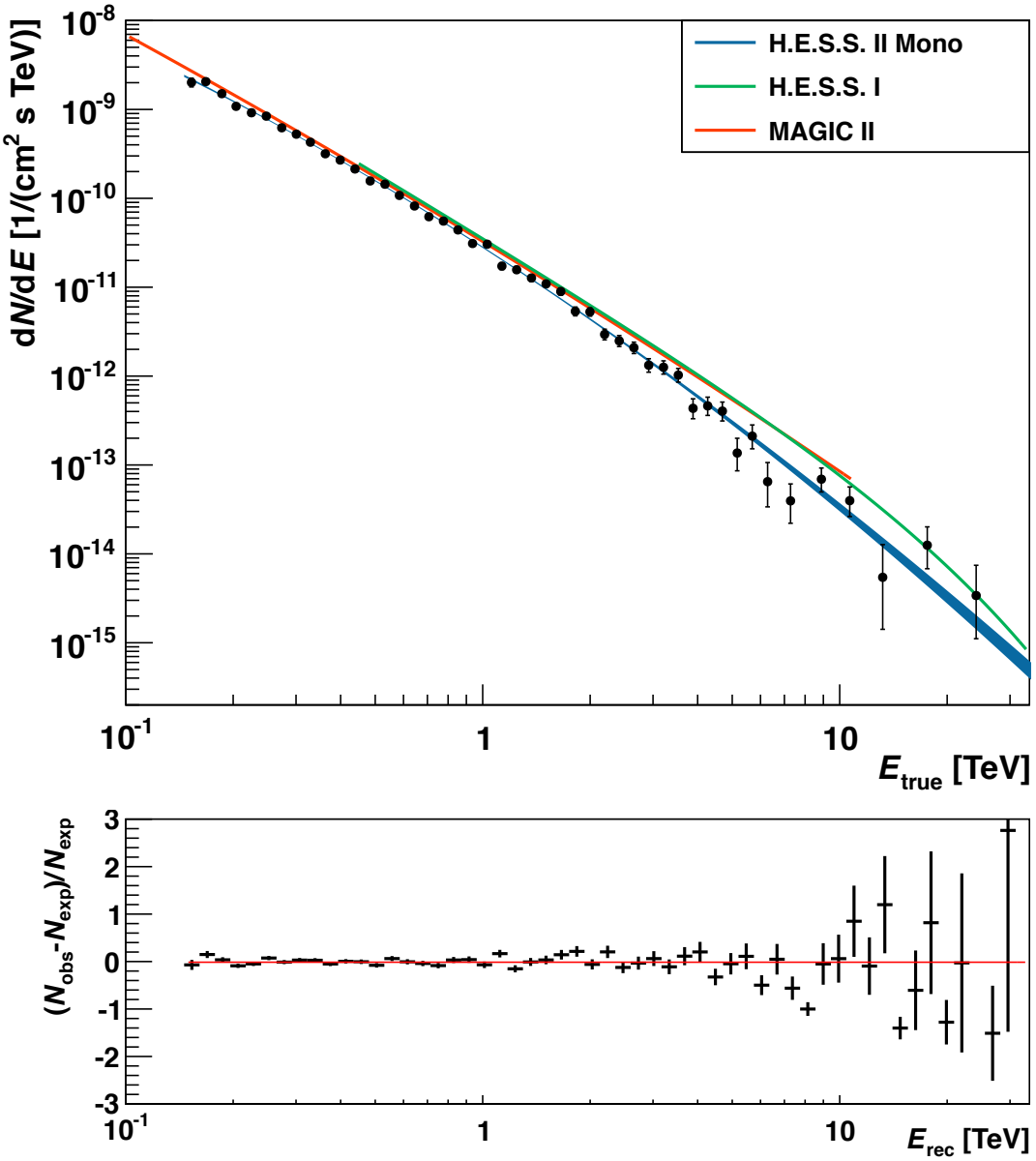

Fig. 5.11: Spectrum of the Crab Nebula as measured with the single-telescope model analysis presented in this work (*Standard* cut configuration). The blue line represents the confidence interval of the best-fit curved power law, and the black points correspond to approximate data points calculated after the forward-folding method. The best-fit results obtained with H. E. S. S. I (Aharonian et al. 2006a) and MAGIC II (Aleksić et al. 2012) are shown for comparison. The fit residuals are drawn in the lower panel of the figure.

The Fermi satellite detected a strong outburst of the source at energies above 100 MeV on 18th October 2013 (Buson et al. 2013), but none of the runs of the H. E. S. S. II data set analysed here was taken during that time. Since no measurable variation is expected, an evaluation of the flux on a run-by run basis is ideal to test how susceptible both the applied run selection and analysis are to systematic disturbances. Fig. 5.12 (*left panel*) shows the integrated photon flux above 1 TeV for each run as a function of the Modified

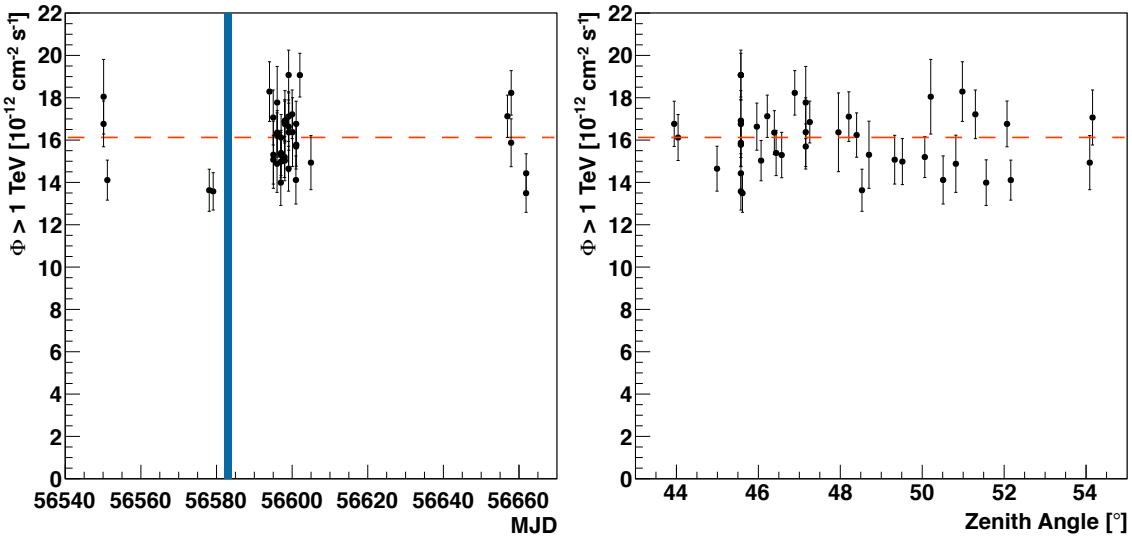

Fig. 5.12: Integrated photon flux of the Crab Nebula above 1 TeV for each run (using *Standard* cuts), separately as a function of the Modified Julian Day (*left*) and the mean pointing zenith angle (*right*). The errors are solely statistical. The blue line in the *left panel* denotes the period of enhanced soft γ-ray excess as reported by (Buson et al. 2013). The dashed red line marks the average flux in both panels.

Julian Day (MJD). As expected, the values scatter statistically around the mean. The same is true for the *right panel* of Fig. 5.12, which contains the run-wise flux with respect to the mean pointing zenith angle. There is no dependency apparent, testifying that the zenith angle does not introduce any bias on the measured flux.

5.2 Analysis of the Galactic Centre Region

The second analysis is performed on the region around the Galactic Centre (GC), with a focus on its central point source.

5.2.1 The Galactic Centre in γ-rays

The central part of our Galaxy, the Milky Way, hosts a variety of different sources that are energetic enough to produce γ-rays. Measuring the photons of this energy domain provides insight in the violent phenomena that take place in that region.

In 1974, a bright and compact radio source was discovered in the GC region by Balick & Brown, which was named Sgr A* some years later (Brown 1982). Using very long baseline radio interferometry, the size of Sgr A* has recently been constrained to be below one astronomical unit (Doeleman 2008). Schödel et al. (2002) observed a star closely orbiting Sgr A* with a period of 15.2 years and a peri-centre distance of only 17 light hours. The derived point mass of roughly 4×10^6 solar masses in combination with its small size provides strong evidence that Sgr A* is a supermassive black hole which corresponds to the nucleus of the Galaxy. Being at a distance of around 8.33 kpc (Gillessen et al. 2009), it is by far the nearest of these objects and is thus of particular interest for both theoretical and experimental astrophysics.

γ-rays from the direction of the GC were first detected with the satellite-based EGRET instrument (Mayer-Hasselwander et al. 1998) at energies above 30 MeV. However, deeper investigations by Pohl (2005) showed that the source is not positionally coincident with Sgr A*. A first hint for the emission of TeV γ-rays from the GC was seen in 2004 with the Whipple telescope (Kosack et al. 2004), followed by a significant detection of VHE γ-rays below 1 TeV by CANGAROO−II (Tsuchiya et al. 2004). Later that year, H. E. S. S. I confirmed that detection (Aharonian et al. 2004a), but reported a much harder spectrum of the source. Follow-up results by MAGIC I are in very good agreement with the H. E. S. S. measurement (Albert et al. 2006), indicating systematic problems of the CANGAROO spectrum. In the following, the VHE γ-ray source will also be referred as HESS J1745−290.

Owing to the poor angular resolution of IACTs compared to most telescopes observing at lower energies, the counterpart of the VHE γ-ray emission of HESS J1745−290 remains undetermined so far. The situation improved when the H. E. S. S. collaboration presented results that were obtained using observations with a higher pointing precision, reducing the systematic uncertainty on the measured position of HESS J1745−290 (Acero et al. 2010). With this study, the authors showed that the supernova remnant Sgr A East is not positionally consistent with the VHE γ-ray source. Two known objects remain as possible counterparts of HESS J1745−290. The first is the X-ray PWN G359.95−0.04 (Wang et al. 2006), whose potential IC emission could account for the measured γ-ray flux (Hinton & Aharonian 2007). Alternatively, Sgr A* might be able to produce γ-rays through various mechanisms (see, e.g., Aharonian & Neronov 2005; Atoyan & Dermer 2004). Of course it should also be considered that the emission of HESS J1745−290 could correspond to a superposition of both G359.95−0.04 and Sgr A*. Although there are lots of various interpretations of the signal, Aharonian et al. (2006b) ruled out the possibility that it mainly originates from the annihilation of dark matter. Motivated by flares of Sgr A* as seen in, e.g., X-rays with *Chandra* and XMM−Newton (Aschenbach

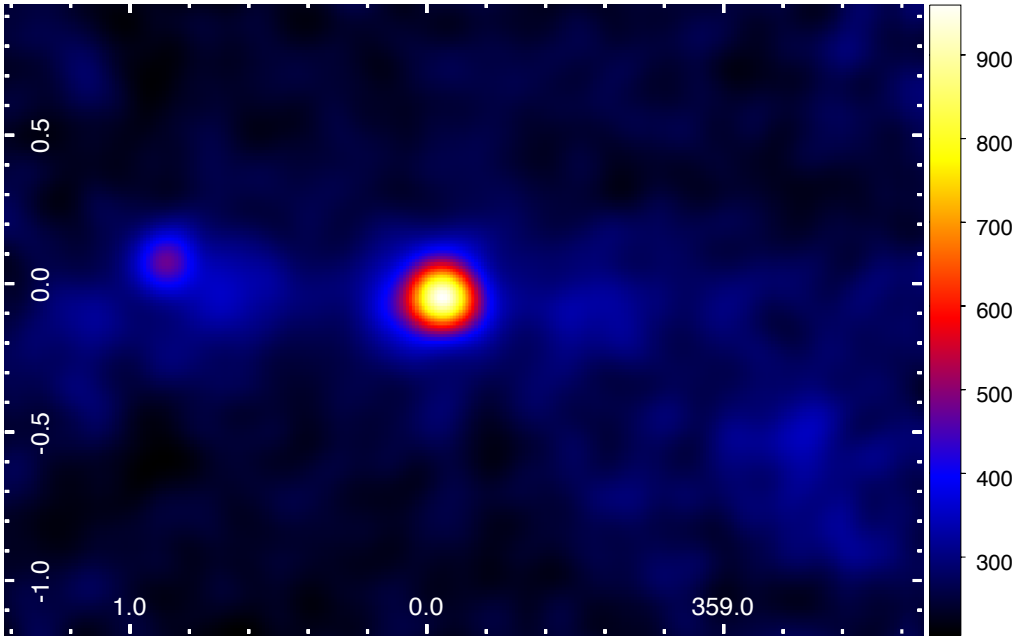

Fig. 5.13: Distribution of γ-like events from the GC region, measured with H. E. S. S. I as published in Aharonian et al. (2006d). The map is displayed in Galactic coordinates, where the longitude corresponds to the horizontal axis, and the latitude to the vertical one. The source in the centre corresponds to HESS J1745−290, and the fainter one on the left to the PWN G0.9+0.1. The diffuse emission whose detection was first published in the reference is situated along the Galactic plane.

et al. 2004), Aharonian et al. (2009) performed a thorough search for variability of the VHE γ-ray flux of HESS J1745−290, which led to a negative result.

Aharonian et al. (2006d) first reported the detection of diffuse VHE γ-ray emission from the GC region, measured with H. E. S. S. I. The resulting count map is shown in Fig. 5.13. The emission is spatially correlated with a molecular cloud complex, compellingly indicating that it mostly originates from interactions of cosmic rays with that complex.

Since the launch of the spaceborne Fermi-LAT telescope in 2008 (see, e.g., Atwood et al. 2009), the sensitivity of measuring cosmic γ-rays in the MeV−GeV range has greatly improved. One example is the detection of large bubbles of emission whose origin appears to be the GC (Su et al. 2010). Another attention-getting result was reported by Weniger (2012), who reported an indication of a line-like feature at an energy of $\approx 130\,\mathrm{GeV}$ in the energy spectra of regions close to the GC. This led to an avalanche of follow-up publications, lots of them trying to explain the signal with dark-matter annihilation processes. The feature was also investigated by the Fermi-LAT collaboration (Ackermann et al. 2013). Although several systematic uncertainties were pointed out in that reference that lead to a decrease of significance, checking the hint will be an important project for H. E. S. S. II. It is, however, beyond the scope of this thesis.

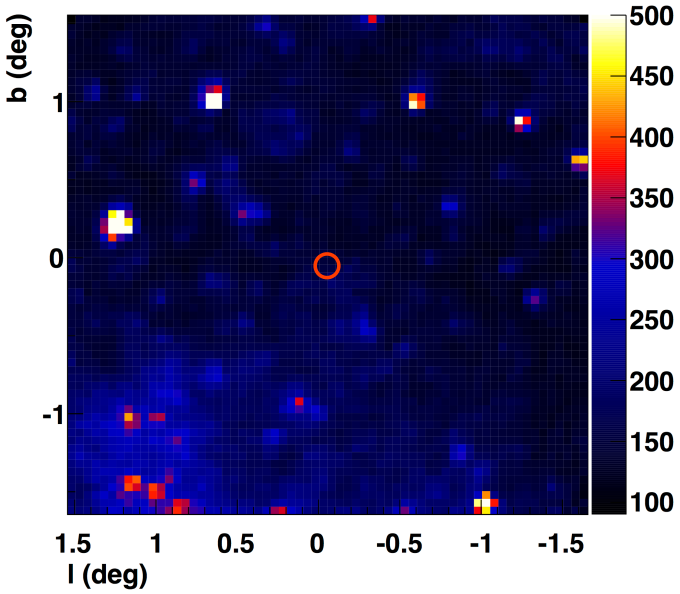

Fig. 5.14: NSB rate (in units of MHz) in the sky region around the GC, estimated using the pedestal width of the pixels of the H. E. S. S. II telescope. The red circle denotes the position of Sgr A*.

5.2.2 Data Set

From the location of the H. E. S. S. telescopes, the region around the GC is generally visible each year from February to November and can be observed at zenith angles below 45° between March and October. Data-taking of the region with the H. E. S. S. II telescope started during its commissioning phase and, due to various physics goals, it is continuously being observed. As for the Crab Nebula analysis, all runs taken during the commissioning phase are discarded from the following analysis.

The calibration of the data is conducted as described in Section 5.1.2. Good-quality runs are also selected correspondingly, with the exception of the mean trigger rate criterion. Where a minimum value of 1200 Hz was chosen for the Crab Nebula, it is set to 1500 Hz for the GC analysis. With most runs ranging between 1800 Hz and 2000 Hz, the threshold also corresponds to around 80% of the mean in this case. Only wobble runs with an offset between 0.5° and 1.0° are used for the analysis. To set a stronger focus on low-energy events, only runs with zenith angles below 45° are analysed.

The data set consists of 77 runs with a total live time of 33.5 hours (after dead-time correction), taken between 8th April and 3rd October 2013. Pointing corrections as described in Gillesen (2004) were applied to all of them.

5.2.3 Results

Compared to the Crab Nebula, the analysis of the GC is far more challenging for several reasons. One of them is that the NSB level in that region varies significantly across the FoV of the camera. This can be seen in Fig. 5.14, which shows the NSB rate in the sky region around the GC, estimated using the pedestal width of the pixels of the H. E. S. S. II telescope (calculated as described for H. E. S. S. I in Aharonian et al. (2004b)). Apart

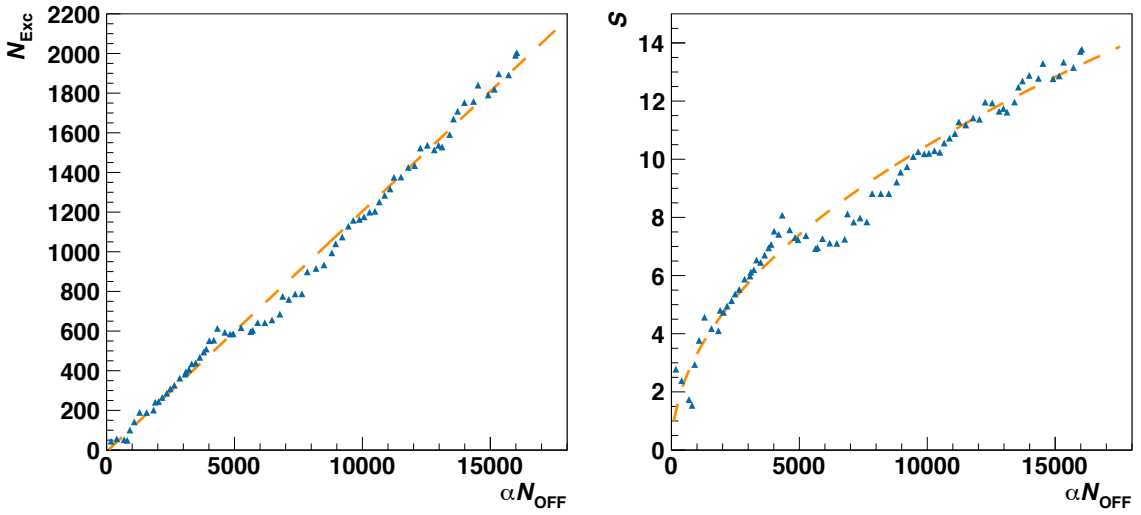

Fig. 5.15: Number of excess events (*left*) and significance (*right*) with respect to the number of rescaled OFF events for the analysis of HESS J1745−290.

from locally enhanced NSB which is due to single stars (bright spots in Fig. 5.14), the rate varies between around 100 MHz and 300 MHz. This strong inhomogeneity is expected to cause systematic uncertainties that are not easy to correct for, such as a FoV-dependent rate of NSB-triggered events. Therefore, the GC region is going to be analysed solely with *Standard* cuts which are less prone to such uncertainties compared to *Loose* cuts.

For the first part of the GC analysis, the focus is set on the central point source HESS J1745−290. Its spectral properties were extensively studied with H. E. S. S. I in the energy range from 160 GeV to 70 TeV (Aharonian et al. 2004a, 2006b, 2009). To prevent distortion of the analysis results, OFF regions were defined in the two latter references such as to not overlap with other known γ-ray emitters, including the diffuse emission regions situated along the Galactic plane (Aharonian et al. 2006d). This implies that the measured spectra include both the emission from the central point source and the diffuse component. The approach was justified with the arguments that, firstly, the spectral shape of the Galactic diffuse emission is similar to that of HESS J1745−290, and, secondly, that its expected contribution to the overall flux is lower than the systematic uncertainty of the measurement. In contrast, the diffuse emission regions are not excluded from the OFF regions for the following H. E. S. S. II analysis of HESS J1745−290. This is because the relative contribution of the diffuse emission is expected to be larger for this analysis due to the larger solid angle of the target region as defined by the $\vartheta^2_{\mathrm{max}}$ cut. It is expected that allowing the respective regions to be used as OFF regions helps to lower this contribution of the diffuse component to the intrinsic signal of HESS J1745−290.

For the following analysis, the target region is centred on the position of Sgr A* (Yusef-Zadeh et al. 1999). For defining OFF regions, a circle with radius 0.4° around the target centre is excluded (i.e. as for the Crab Nebula analysis presented in Section 5.1.3). Additional exclusion regions cover the VHE γ-ray sources G0.9+0.1 (Aharonian et al. 2005) and HESS J1745−303 (Aharonian et al. 2006c). The background subtraction is performed using the *reflected-region* method (Berge et al. 2007).

The development of the number of excess events with respect to the number of rescaled OFF events is shown in the *left panel* of Fig 5.15. Apart from a local flattening at

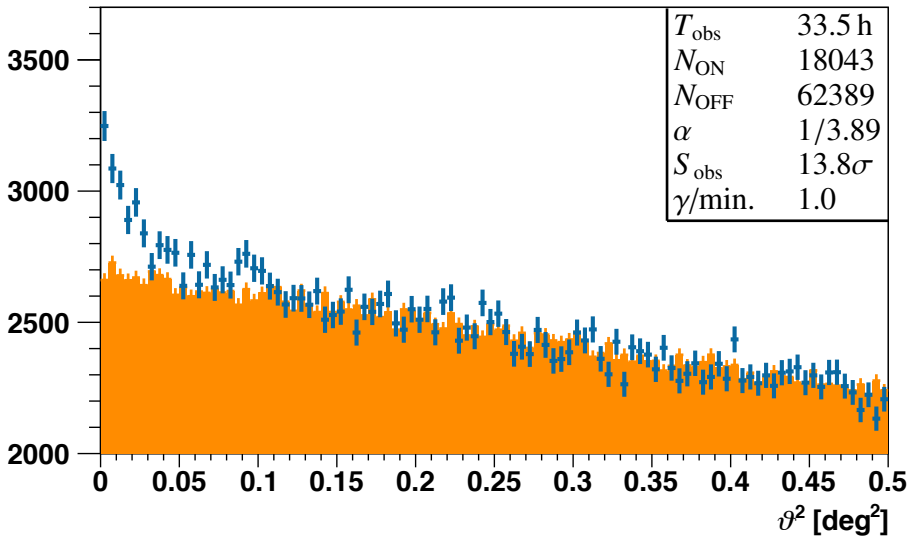

Fig. 5.16: ϑ^2 distribution of γ-like events from the direction of Sgr A*. The histogram of the ON region is drawn in blue, and the one of the OFF regions (scaled with α) in orange. The analysis statistics are shown on the upper right.

$\alpha N_{\mathrm{OFF}} \approx 5000$, the excess rises linearly. The significance (drawn in the *right panel*) develops correspondingly, scattering statistically around the fitted square root function over most of the range.

Fig. 5.16 displays the ϑ^2 histogram of γ-like events from the direction of Sgr A*. The ON distribution clearly peaks at $0\,\mathrm{deg}^2$ and is well compatible with the distribution of OFF events at $\vartheta^2 \gtrsim 0.1\,\mathrm{deg}^2$. This indicates that the diffuse emission is properly subtracted for the excess calculation within the measurable range and is not expected to shift or warp the spectrum of HESS J1745−290 (assuming that there is no strong local variability of the spectral shape of the diffuse emission).

The fit statistics of the analysis are also shown in Fig. 5.16. Compared to the *Standard*-cut analysis of the Crab Nebula (see Section 5.1.3), the average number of reflected regions per run is lower due to the exclusion regions. The excess rate is roughly 30% higher than the one obtained with H. E. S. S. I (Aharonian et al. 2009, 4185 excess events in 92.9 hours, yielding around $0.75\,\gamma$/min.). Although the effective area of H. E. S. S. II for the *Standard* cuts is lower than the one of H. E. S. S. I above 150 GeV (see Fig. 4.12), the lower energy threshold overcompensates this difference.

In both Aharonian et al. (2004a) and Aharonian et al. (2006b), the spectrum of HESS J1745−290 could be well characterised by a power law. Due to an enhanced data set, a significant deviation from this shape was found by Aharonian et al. (2009). According to the authors, the data can be both described by an exponential cutoff power law (see Eq. 5.6) and a smoothed broken power law (see Eq. (4) in the reference), where the former exhibits a slightly better fit quality ($\chi^2/\mathrm{NDF} = 23/26$ as compared to 20/19 for the smoothed broken power law). The deviation from a standard power law starts to occur at roughly 10 TeV.

The spectrum of HESS J1745−290 as measured with H. E. S. S. II from approximately 60 GeV to 10 TeV is shown in Fig. 5.17. The data are well described by a standard power law, which is apparent from both the fit residuals and the fit statistics. As for the spectrum

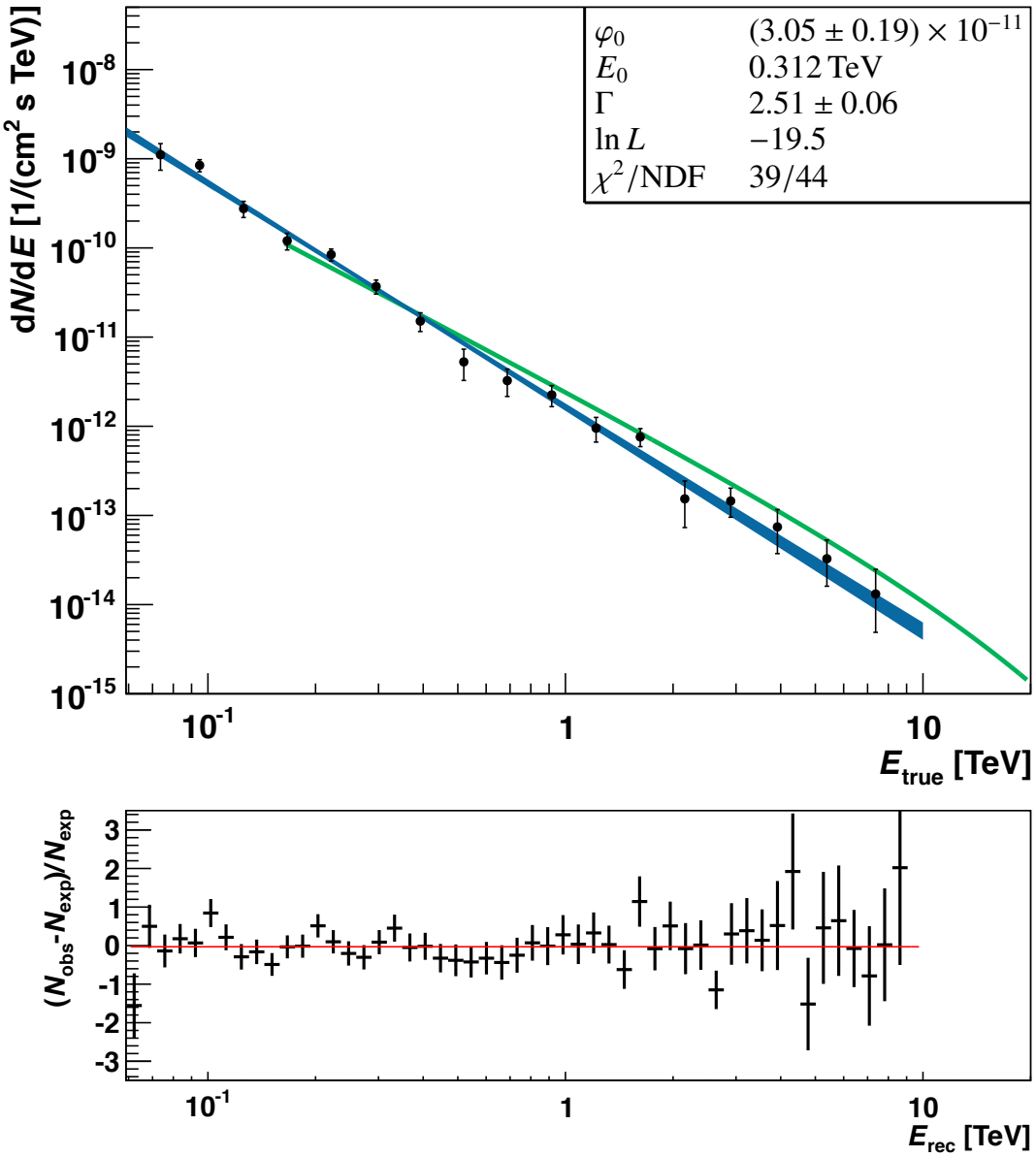

Fig. 5.17: Spectrum of the GC point source HESS J1745−290, obtained by assuming a relative optical efficiency of 100% (1σ confidence region in blue, forward-folded spectrum points in black). The residuals are given in the lower part. The results of the power-law fit are shown in the upper right (see Eq. 5.5 for the definition of the function parameters). The flux normalisation φ_0 is given in units of $1/(\mathrm{cm}^2\,\mathrm{s}\,\mathrm{TeV})$. The best-fitting exponential cutoff power law as measured with H. E. S. S. I (Aharonian et al. 2009) is shown in green.

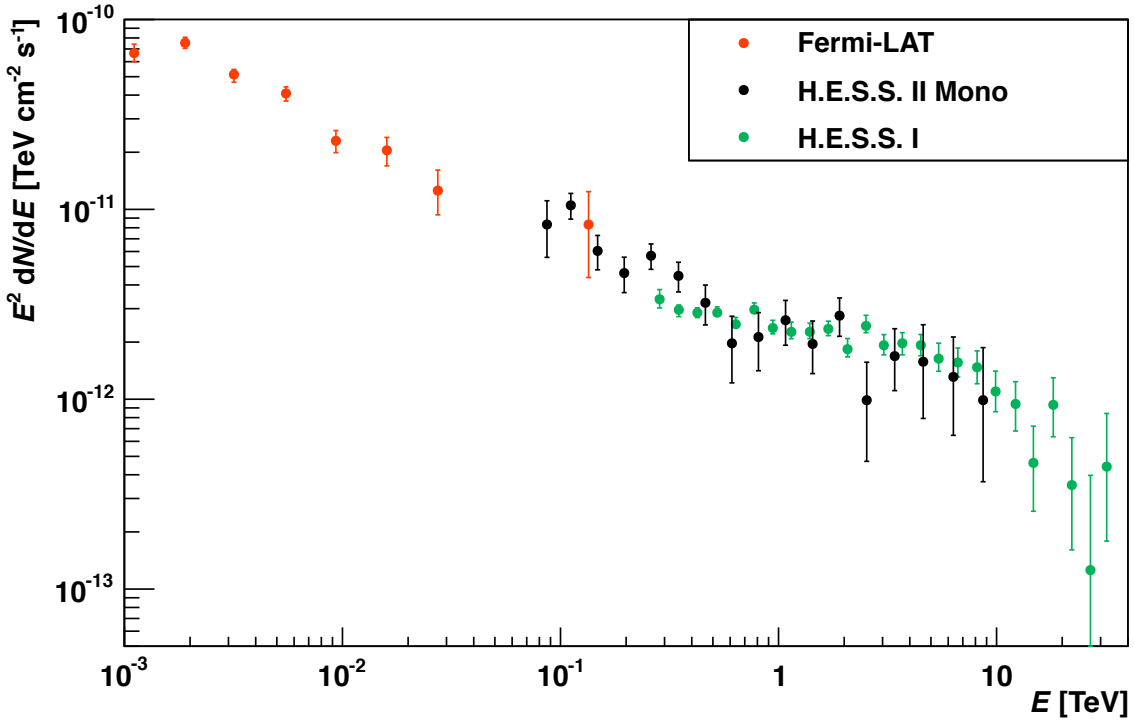

Fig. 5.18: Spectral energy distribution of the GC γ-ray source. The spectral points of Fermi-LAT are taken from Chernyakova et al. (2011), and the ones of H. E. S. S. I from Aharonian et al. (2009). Each of the points of the H. E. S. S. II spectrum was shifted by a factor of 1.00/0.85 in energy to correct for the bias that was introduced by using the preliminary lookup tables. As this is just a first-order correction, the figure has to be considered preliminary.

of the Crab Nebula (Fig. 5.11), preliminary lookup tables were used to derive the results, assuming a relative optical efficiency of 100%. The figure also includes the best-fitting exponential cutoff power law from Aharonian et al. (2009). The H. E. S. S. II spectrum appears to be distinctly steeper (for H. E. S. S. I, $\Gamma = 2.10 \pm 0.04_{\mathrm{stat}} \pm 0.10_{\mathrm{sys}}$), which might be due to either an intrinsic difference at low energies or a yet unresolved systematic effect that affects the H. E. S. S. analysis.

With its lower threshold, H. E. S. S. II now enables large event statistics at energies around 100 GeV, corresponding to the domain where the background-free Fermi-LAT runs out of statistics. This is illustrated in Fig. 5.18, which contains the spectral energy distribution of the GC γ-ray source, measured with Fermi-LAT (Chernyakova et al. 2011), H. E. S. S. II (this work), and H. E. S. S. I (Aharonian et al. 2009). To correct to first order for the bias that was introduced by using the preliminary lookup tables, each of the H. E. S. S. II spectrum points was shifted by a factor of 1.00/0.85 in energy (where 85% is the approximate real relative optical efficiency). After this correction, the H. E. S. S. I and H. E. S. S. II spectra are in good agreement at energies above 500 GeV. The (purely statistical) errors are larger for H. E. S. S. II, which is partly because of the $\approx$ 65% lower live time and partly because of the poorer γ-hadron separation of the single-telescope reconstruction. As mentioned before, the photon index of the H. E. S. S. II spectrum is larger, leading to a worse agreement at lower energies. The new spectrum extends to much lower energies, well overlapping and matching with the Fermi-LAT spectrum.

After the investigation of HESS J1745−290, the focus of the following part is to test the imaging capabilities of the analysis for the GC sky region, using the *ring background* method from Berge et al. (2007). For this second analysis, additional regions with known γ-ray emission are excluded from both the OFF regions and the run-wise acceptance calculation to improve the normalisation of the maps (see *lower left* panel of Fig. 5.19). In addition to HESS J1745−290, which is excluded with a radius of 0.45°, and HESS J1745−303 (0.4°), the whole area with Galactic latitude between −0.4° and +0.4° is defined as an OFF region. This includes the PWN G0.9+0.1, which was also excluded for the spectral analysis.

The resulting excess map is shown in the *top* panel of Fig. 5.19. A circular-shaped region on the right part of the map is masked because it is of particular interest for the cross-check of the spectral feature claimed by Weniger (2012) using Fermi-LAT data. Its investigation is beyond the scope of this thesis. As expected from the ϑ^2 distribution of the previous analysis (Fig. 5.16), there is a strong excess at the position of Sgr A*. Apart from this point source, the map appears to contain diffuse emission. Contours of the H. E. S. S. I emission from Aharonian et al. (2006d) are drawn, denoting the areas in which the relative excess exceeds ≈ 10% of its maximum. In comparison, the emission seen by H. E. S. S. II appears to be stronger and more extended. This is expected to a certain level when comparing it with the contours of the emission above 10 GeV as seen by Fermi-LAT[1] (also corresponding to ≈ 10% of the maximum). However, the obvious systematic uncertainties in the map suggest caution should be used with the interpretation. Several parts of the map, particularly the lower left, feature distinctly negative excess values, indicating a correlation with the enhanced NSB in this region (see Fig. 5.14). The feature is even more apparent in the significance map (shown on the *lower left*). The significance distribution of the OFF regions (*lower right* panel) is too broad. In addition to the systematic uncertainties, this might also indicate that the current set of exclusion regions is not yet sufficient to account for the extended diffuse emission. Using even larger exclusion regions is, however, difficult with the small FoV of the H. E. S. S. II telescope. A possible solution to this problem is to implement a likelihood analysis approach in the software framework, similar to the one that was first introduced for the EGRET instrument (Mattox et al. 1996).

[1] The contours were created using data that are publicly available at:
`http://fermi.gsfc.nasa.gov/ssc/data/access/lat/`

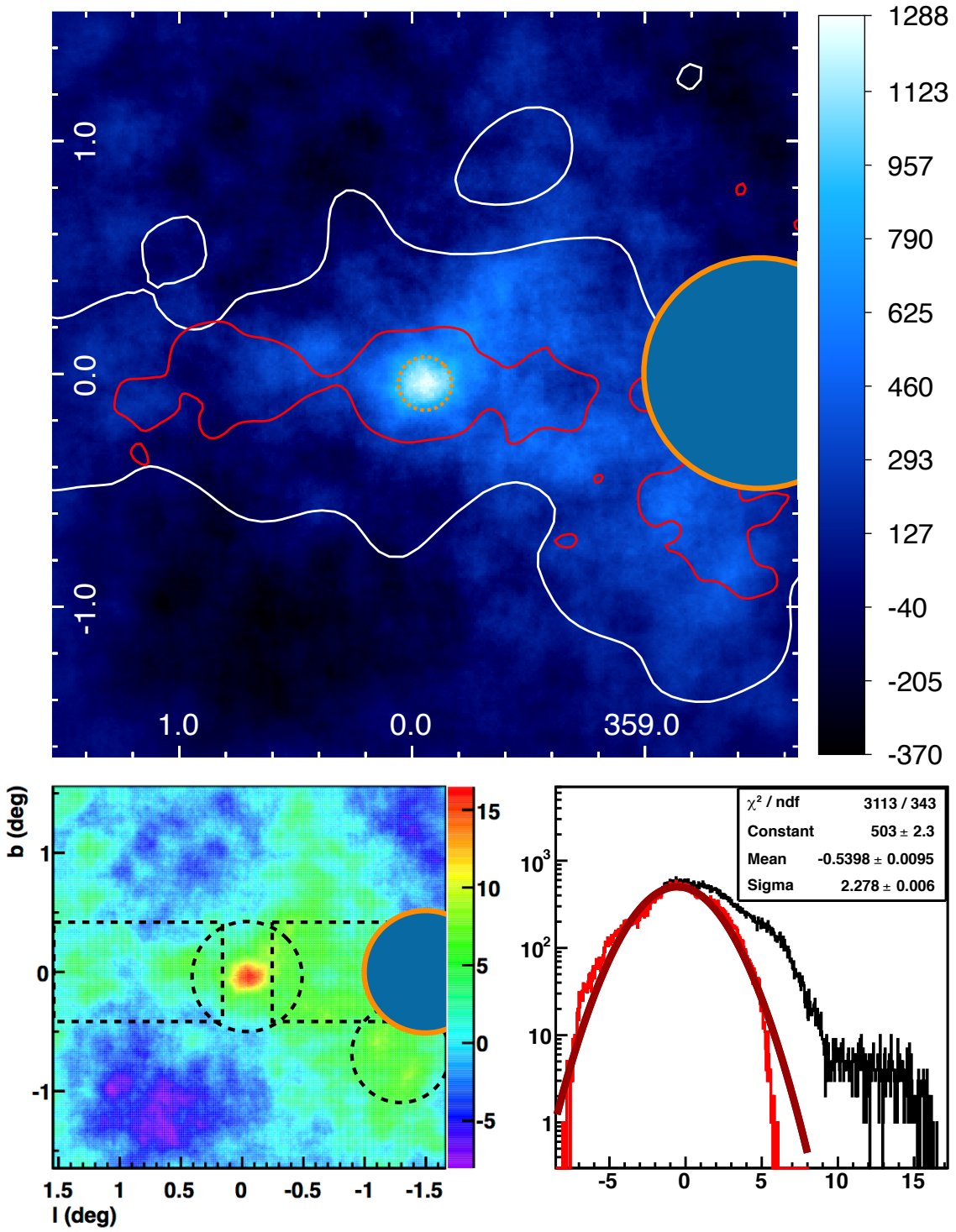

Fig. 5.19: *Top:* excess map of the GC region. The red contours correspond to the excess measured with H. E. S. S. I (Aharonian et al. 2006d), whereas the white contours indicate the emission above 10 GeV as seen by Fermi-LAT. The position of Sgr A* is shown with a dashed orange circle. *Lower left:* significance map obtained using the *ring background* method (Berge et al. 2007). The exclusion regions used for the analysis are encompassed by dashed black lines. *Lower right:* significance distribution, separately for the OFF regions (red) and the whole map (black). In both maps, a circular region is masked because it is of particular interest for the cross-check of the spectral feature claimed by Weniger (2012) using Fermi-LAT data.

6 Conclusion and Outlook

In the presented work, the most advanced photon reconstruction method currently available in ground-based γ-ray astronomy was successfully adapted to the H. E. S. S. II telescope. It was afterwards applied to observations of the Crab Nebula and the GC region. The analysis results of both regions emphasise the capabilities of the new telescope to measure γ-rays in an energy range that is still poorly explored.

The presented method performs much better compared to similar previous work in terms of signal-to-background ratio and γ-hadron separation (see Section 5.1.3). Remarkably, the obtained significance of the Crab Nebula per observation time is even larger than the one obtained with H. E. S. S. I with a Hillas analysis, indicating that the sensitivity of the method presented here is of the same order. This is in agreement with the expectations of Section 4.4.

A good agreement between simulated and real events indicates a good understanding of the detector and thus helps the obtained results to be trusted. Although the performance of the reconstruction and analysis could also be solely evaluated from the data, the MC-data comparisons that were performed enable the detector's behaviour to be studied in much greater detail. This, e.g., applies for the MC-data comparison of the energy distributions of the Crab Nebula (Fig. 5.10), which match very well for *Standard* cuts. No scaling was applied to normalise the two energy distributions, implying a good understanding of the overall instrument response. Even for *Loose* cuts, where the systematic uncertainties are expected to be larger, the agreement is still acceptable, endorsing that the measured excess at around 40 GeV is real despite the large zenith angle of more than 45°. The apparent differences for this cut configuration might be resolved in the future by improving the detector simulation. The generally good agreement between the distributions of the values that are used for the event selection assures that the selection variables are suitable to be used for the γ-hadron separation.

The analysis results of the Crab Nebula, which make use of both the *ring background* as well as the *reflected region background* method, appear reasonable. The good normalisations of the ϑ^2 distributions of the ON and OFF regions show that the PSF does not suffer from tails that are not properly taken into account. Apart from being slightly too small, the significance distribution outside the target region looks as expected. The Crab Nebula appears as a circular point source in the maps, proving that the analysis is usable for creating sky maps and even able to properly handle regions of locally enhanced NSB due to single stars.

Owing to the lower energy threshold compared to H. E. S. S. I, the H. E. S. S. II telescope is now able to measure the whole spectral domain from close to the Crab Nebula's IC peak up to several tens of TeV. As for MAGIC I and MAGIC II, the spectrum is best described by a curved power law. Notably the spectrum presented here extends to larger energies than the one obtained with the stereoscopic MAGIC II system. Since no flux variations with respect to the observation date and zenith angle were found, the systematics appear to be well understood for the chosen run selection.

The second test of the analysis was performed on the Galactic Centre region. Calculating properly normalised excess and significance maps becomes more complicated for regions with larger-scale NSB variations, such as the one around the GC. The analysis is even more difficult if large parts of the FoV are covered by diffuse emission, as appears to be the case with the GC. While the usual background subtraction methods fail in this case, a likelihood analysis approach might be able to solve this problem.

In contrast to the aforementioned difficulties that concern the calculation of the sky map, the analysis of the GC point source (HESS J1745−290) did not seem to be affected by large systematic uncertainties. The good normalisation between the ϑ^2 distributions of the ON and OFF events indicates that the diffuse emission is properly subtracted. The minimum energy of the spectrum is $\approx 60\,\mathrm{GeV}$, which is far below the energies H. E. S. S. has ever reached before. The well-matching overlap of the H. E. S. S. II spectrum with the spectrum from Fermi-LAT might indicate systematic problems of the H. E. S. S. I spectrum near the threshold, but the same could be the case for H. E. S. S. II and has to be investigated in the near future.

With its low energy threshold, the H. E. S. S. II telescope enables us to explore the sky regions that are visible from the Earth's southern hemisphere at energies around and below 100 GeV with unprecedented statistics. A very recent result that emphasises this statement is the detection of pulsed emission from the Vela pulsar using the analysis presented in this thesis. This source is very bright at energies around 1 GeV and was thus easily detected by Fermi-LAT in that range (Abdo et al. 2010). At energies $\gtrsim 20\,\mathrm{GeV}$, the event statistics are however quite low due to a steep source spectrum in combination with the small effective area of this spaceborne instrument.

Fig 6.1 (*top panel*) shows the phase distribution of events from the direction of the Vela pulsar, reconstructed with the method which was presented in this work (using the *Loose* cut configuration with an enlarged $\vartheta^2_{\mathrm{max}}$ cut). Despite an observation time of only 17 hours, pulsations are detected at a $\approx 10\sigma$ level in the phase range that corresponds to the second peak (P2) of the distribution that was measured with Fermi-LAT (Abdo et al. 2010). The ≈ 6000 excess events prove the capability of the new analysis and telescope to collect large statistics on a short time scale. The energy distribution of the excess events is displayed in the *bottom panel* of Fig. 6.1. The first measurable excess appears below 20 GeV, which most likely corresponds to even lower true energies due to the energy bias as measured in Section 4.3. These are the lowest energies that have ever been reached in ground-based γ-ray astronomy. Understanding the instrument in the low-energy domain has top priority for H. E. S. S. as it is crucial in order to make credible statements with potentially high impact on the astrophysics community.

In addition to pulsars, transient sources like GRBs probably constitute the largest science potential for H. E. S. S. II. Using the *Loose* cuts, H. E. S. S. II is expected to be more sensitive than Fermi-LAT on variability time scales of around one year and shorter at energies down to 20 GeV. For the same energies and variability time scales of around one hour, H. E. S. S. II is able to detect 1000 times fainter sources compared to Fermi-LAT.

In summary, the results presented in this thesis promise an exciting future for ground-based γ-ray astronomy, particularly regarding the energy domain around and below 100 GeV. The presented analysis will be a key tool used in the exploration of the southern sky with H. E. S. S. II in the years to come.

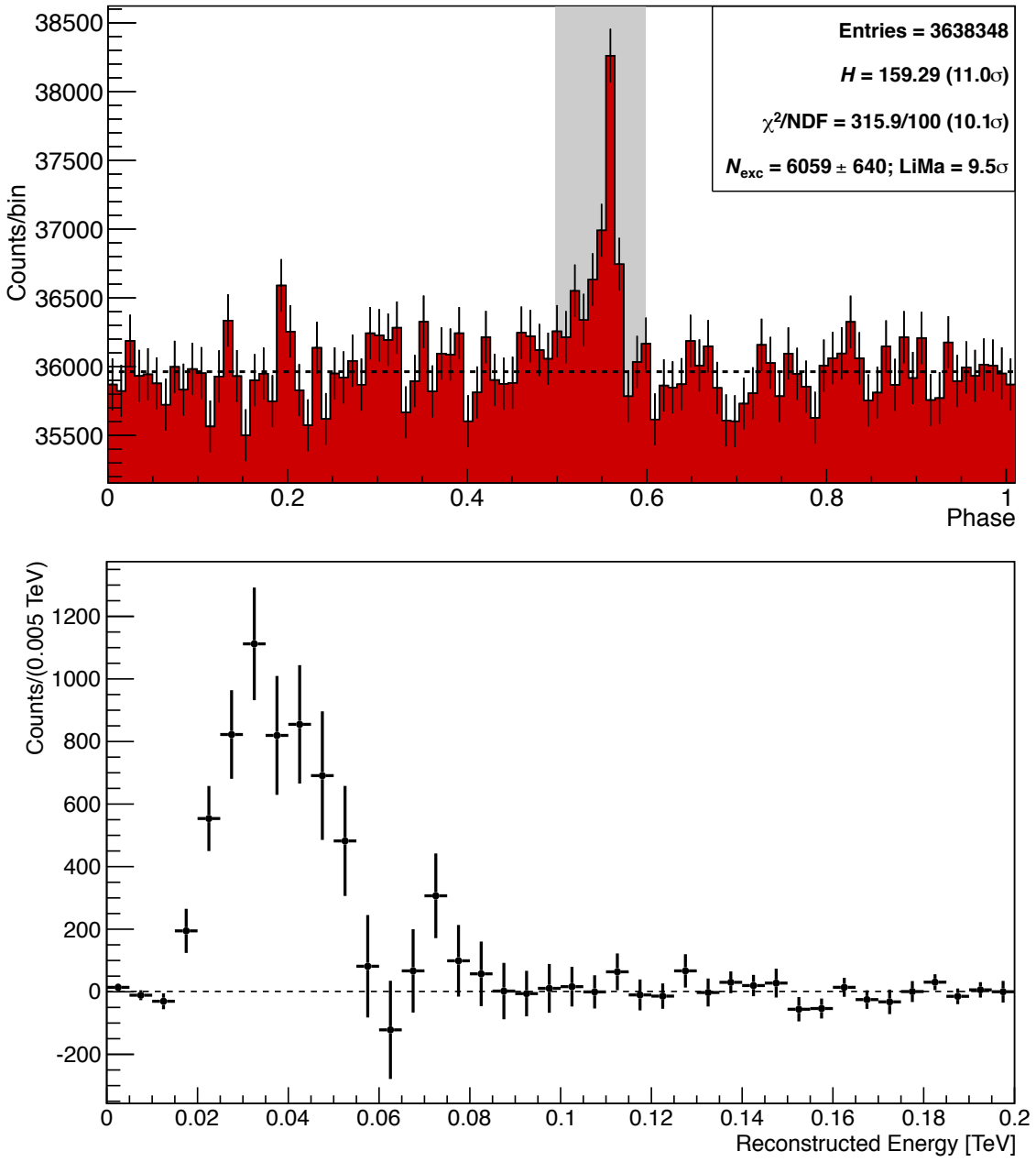

Fig. 6.1: *Top:* phase distribution of γ-like events from the direction of the Vela pulsar for *Loose* cuts (using an enlarged $\vartheta^2_{\mathrm{max}}$ cut of $0.16\,\mathrm{deg}^2$). The ON region is denoted by the grey area, whereas the rest of the phase range is defined as one single OFF region. *Bottom:* distribution of reconstructed energy of the excess shown in the *top* panel.

List of Figures

List of Tables

Bibliography

Abdo, A. A., Ackermann, M., Ajello, M., et al. 2010, ApJ, 713, 154

Abdo, A. A., Ackermann, M., Ajello, M., et al. 2011, Science, 331, 739

Acero, F., Aharonian, F., Akhperjanian, A. G., et al. 2010, MNRAS, 402, 1877

Ackermann, M., Ajello, M., Albert, A., et al. 2013, Phys. Rev. D, 88, 082002

Aharonian, F., Akhperjanian, A. G., Anton, G., et al. 2009, A&A, 503, 817

Aharonian, F., Akhperjanian, A. G., Aye, K.-M., et al. 2005, A&A, 432, L25

Aharonian, F., Akhperjanian, A. G., Aye, K.-M., et al. 2004a, A&A, 425, L13

Aharonian, F., Akhperjanian, A. G., Aye, K.-M., et al. 2004b, Astroparticle Physics, 22, 109

Aharonian, F., Akhperjanian, A. G., Bazer-Bachi, A. R., et al. 2007, ApJ, 664, L71

Aharonian, F., Akhperjanian, A. G., Bazer-Bachi, A. R., et al. 2006a, A&A, 457, 899

Aharonian, F., Akhperjanian, A. G., Bazer-Bachi, A. R., et al. 2006b, Physical Review Letters, 97, 221102

Aharonian, F., Akhperjanian, A. G., Bazer-Bachi, A. R., et al. 2006c, ApJ, 636, 777

Aharonian, F., Akhperjanian, A. G., Bazer-Bachi, A. R., et al. 2006d, Nature, 439, 695

Aharonian, F., Akhperjanian, A. G., Bazer-Bachi, A. R., et al. 2006e, A&A, 460, 365

Aharonian, F. & Neronov, A. 2005, ApJ, 619, 306

Aharonian, F. A., Akhperjanian, A. G., Barrio, J. A., et al. 2000a, A&A, 361, 1073

Aharonian, F. A., Akhperjanian, A. G., Barrio, J. A., et al. 2000b, ApJ, 539, 317

Aharonian, F. A. & Bogovalov, S. V. 2003, New Astronomy, 8, 85

Albert, J., Aliu, E., Anderhub, H., et al. 2006, ApJ, 638, L101

Albert, J., Aliu, E., Anderhub, H., et al. 2008a, ApJ, 674, 1037

Albert, J., Aliu, E., Anderhub, H., et al. 2008b, ApJ, 674, 1037

Aleksić, J., Alvarez, E. A., Antonelli, L. A., et al. 2012, Astroparticle Physics, 35, 435

Aleksić, J., Ansoldi, S., Antonelli, L. A., et al. 2014, A&A, 565, L12

Aliu, E., Anderhub, H., Antonelli, L. A., et al. 2009, Astroparticle Physics, 30, 293

Aliu, E., Archambault, S., Aune, T., et al. 2014, ApJ, 781, L11

Aliu, E., Arlen, T., Aune, T., et al. 2011, Science, 334, 69

Aschenbach, B., Grosso, N., Porquet, D., & Predehl, P. 2004, A&A, 417, 71

Atoyan, A. & Dermer, C. D. 2004, ApJ, 617, L123

Atwood, W. B., Abdo, A. A., Ackermann, M., et al. 2009, ApJ, 697, 1071

Balick, B. & Brown, R. L. 1974, ApJ, 194, 265

Balzer, A. 2014, Dissertation, Universität Potsdam, Potsdam, Germany

Balzer, A., Füßling, M., Gajdus, M., et al. 2014, Astroparticle Physics, 54, 67

Barnacka, A. 2013, Dissertation, Polish Academy of Sciences & Universite Paris-Sud 11, Warsaw, Poland; Paris, France, http://arxiv.org/abs/1307.4050

Berge, D., Funk, S., & Hinton, J. 2007, A&A, 466, 1219

Blair, W. P., Long, K. S., Vancura, O., et al. 1992, ApJ, 399, 611

Blumenthal, G. R. & Gould, R. J. 1970, Reviews of Modern Physics, 42, 237

Bolmont, J., Corona, P., Gauron, P., et al. 2013, ArXiv e-prints

Breisky. 2012, http://www.nytimes.com/2012/08/07/science/space/when-victor-hess-discovered-cosmic-rays-in-a-hydrogen-balloon.html?_r=0

Brown, R. L. 1982, ApJ, 262, 110

Buson, S., Buehler, R., & Hays, E. 2013, The Astronomer's Telegram, 5485, 1

Celik, O. 2008, International Cosmic Ray Conference, 2, 847

Chalme-Calvet, R., de Naurois, M., Tavernet, J.-P., & for the H. E. S. S. Collaboration. 2014, ArXiv e-prints

Cherenkov, P. A. 1934, Doklady Akademii Nauk SSSR, 2, 451

Chernyakova, M., Malyshev, D., Aharonian, F. A., Crocker, R. M., & Jones, D. I. 2011, ApJ, 726, 60

Cocke, W. J., Disney, M. J., & Taylor, D. J. 1969, Nature, 221, 525

Collins, II, G. W., Claspy, W. P., & Martin, J. C. 1999, PASP, 111, 871

Commichau, S. C., Biland, A., Contreras, J. L., et al. 2008, Nuclear Instruments and Methods in Physics Research A, 595, 572

de Naurois, M. 2000, Dissertation, Université Pierre et Marie Curie - Paris VI, Paris, France, http://tel.archives-ouvertes.fr/tel-00004261

de Naurois, M. 2012, Habilitation thesis, Laboratoire Leprince-Ringuet, Ecole polytechnique, Palaiseau, France, http://tel.archives-ouvertes.fr/tel-00687872

de Naurois, M., Guy, J., Djannati-Atai, A., Tavernet, J. P., & H.E.S.S. Collaboration. 2003, International Cosmic Ray Conference, 5, 2907

de Naurois, M. & Rolland, L. 2009, Astroparticle Physics, 32, 231

Doeleman, S. 2008, Journal of Physics Conference Series, 131, 012055

Duyvendak, J. J. L. 1942, PASP, 54, 91

Fermi, E. 1949, Physical Review, 75, 1169

Fomin, V. P., Stepanian, A. A., Lamb, R. C., et al. 1994, Astroparticle Physics, 2, 137

Funk, S., Hinton, J. A., & the CTA Consortium. 2013, Astroparticle Physics, 43, 348

Gaensler, B. M. & Slane, P. O. 2006, ARA&A, 44, 17

Galbraith, W. & Jelley, J. V. 1953, Nature, 171, 349

Gillesen, S. 2004, Dissertation, Ruprecht-Karls-Universität Heidelberg, Heidelberg, Germany, `http://www.bsz-bw.de/cgi-bin/xvms.cgi?SWB11244050`

Gillessen, S., Eisenhauer, F., Trippe, S., et al. 2009, ApJ, 692, 1075

Graham, J. R., Wright, G. S., & Longmore, A. J. 1990, ApJ, 352, 172

Greisen, K. 1956, Prog. Cosmic Ray Physics, 3, 1

H.E.S.S. Collaboration, Abramowski, A., Acero, F., et al. 2012, A&A, 548, A46

H.E.S.S. Collaboration, Abramowski, A., Aharonian, F., et al. 2014, A&A, 562, L4

Hester, J. J. 2008, ARA&A, 46, 127

Hillas, A. M. 1985, in International Cosmic Ray Conference, Vol. 3, International Cosmic Ray Conference, ed. F. C. Jones, 445–448

Hinton, J. A. & Aharonian, F. A. 2007, ApJ, 657, 302

Hofverberg, P., Kankanyan, R., Panter, M., et al. 2013, ArXiv e-prints

Kennel, C. F. & Coroniti, F. V. 1984, ApJ, 283, 694

Kertzman, M. P. & Sembroski, G. H. 1994, Nuclear Instruments and Methods in Physics Research A, 343, 629

Kosack, K., Badran, H. M., Bond, I. H., et al. 2004, ApJ, 608, L97

Levenberg, K. 1944, The Quarterly of Applied Mathematics, 2, 164

Li, T.-P. & Ma, Y.-Q. 1983, ApJ, 272, 317

Lobanov, A. P., Horns, D., & Muxlow, T. W. B. 2011, A&A, 533, A10

Loparco, F. & Fermi LAT Collaboration. 2011, Nuclear Instruments and Methods in Physics Research A, 630, 136

MAGIC Collaboration. 2008, Science, 322, 1221

Marquardt, D. 1963, SIAM Journal on Applied Mathematics, 11, 431

Marsden, P. L., Gillett, F. C., Jennings, R. E., et al. 1984, ApJ, 278, L29

Mattox, J. R., Bertsch, D. L., Chiang, J., et al. 1996, ApJ, 461, 396

Mayall, N. U. & Oort, J. H. 1942, PASP, 54, 95

Mayer, M., Buehler, R., Hays, E., et al. 2013, ApJ, 775, L37

Mayer-Hasselwander, H. A., Bertsch, D. L., Dingus, B. L., et al. 1998, A&A, 335, 161

Mazin, D. 2007, Dissertation, Technische Universität München, Munich, Germany, `https://magicold.mpp.mpg.de/publications/theses/DMazin.pdf`

Ohm, S., van Eldik, C., & Egberts, K. 2009, Astroparticle Physics, 31, 383

Parsons, R. D. & Hinton, J. A. 2014, Astroparticle Physics, 56, 26

Piron, F., Djannati-Atai, A., Punch, M., et al. 2001, A&A, 374, 895

Pohl, M. 2005, ApJ, 626, 174

Ranganathan, A. 2004, The Levenberg-Marquardt Algorithm, `http://ananth.in/docs/lmtut.pdf`

Rees, M. J. & Gunn, J. E. 1974, MNRAS, 167, 1

Schödel, R., Ott, T., Genzel, R., et al. 2002, Nature, 419, 694

Seward, F. D., Tucker, W. H., & Fesen, R. A. 2006, ApJ, 652, 1277

Spitkovsky, A. 2008, ApJ, 682, L5

Su, M., Slatyer, T. R., & Finkbeiner, D. P. 2010, ApJ, 724, 1044

Tavani, M., Bulgarelli, A., Vittorini, V., et al. 2011, Science, 331, 736

Trimble, V. 1968, AJ, 73, 535

Tsuchiya, K., Enomoto, R., Ksenofontov, L. T., et al. 2004, ApJ, 606, L115

Wang, Q. D., Lu, F. J., & Gotthelf, E. V. 2006, MNRAS, 367, 937

Weekes, T. C., Cawley, M. F., Fegan, D. J., et al. 1989, ApJ, 342, 379

Weniger, C. 2012, Journal of Cosmology and Astroparticle Physics, 8, 7

Yusef-Zadeh, F., Choate, D., & Cotton, W. 1999, ApJ, 518, L33

Zhang, L., Chen, S. B., & Fang, J. 2008, ApJ, 676, 1210